# MEASUREMENTS AND MODELING OF THE FLOW OF SUPERCRITICAL CARBON DIOXIDE THROUGH ORIFICES

**by**

**John P. Edlebeck**

**A thesis submitted in partial fulfillment of the requirements for the degree of**

**Master of Science**

**(Mechanical Engineering)**

**at the**

**UNIVERSITY OF WISCONSIN-MADISON**

**2013**

This thesis has been approved by

_____

Professor Gregory F. Nellis

_____

Professor Sanford A. Klein

_____

Doctor Mark H. Anderson

Date: _____

## Abstract

This thesis describes the methods used to measure and model the flow of supercritical and two-phase Carbon Dioxide ($CO_2$) through sharp-edged orifices with small and large length-to-diameter ratios (L/D). Orifices with diameters of 1 millimeter and L/D of 3.2, 5, and 20 were investigated. Flow rates through the orifices were measured over a broad range of inlet conditions with orifice inlet pressures ranging from 5 MPa to 11 MPa and orifice inlet densities ranging from 86.5 $kg/m^3$ to 630 $kg/m^3$.

The data that were collected with orifices with small L/D were used to investigate the form losses associated with the contraction and expansion of the fluid at the orifice entrance. The data was compared to the isentropic model for the expansion of a fluid in order to determine an empirical discharge coefficient. The single-phase isentropic model was used for single-phase orifice outlet conditions, and the Homogeneous Equilibrium Model (HEM) and the Separated Flow Model (SFM) were compared for two-phase orifice outlet conditions. It was observed that for two-phase orifice outlet conditions, the SFM provides a more accurate prediction of the behavior of the data than the HEM when used with an empirical discharge coefficient. All of the data that were collected with orifices with small L/D are predicted within five percent by applying an empirical discharge coefficient of 0.82 to the single-phase isentropic model for single-phase orifice outlet conditions or the isentropic SFM with either Moody's or Fauske's correlation for the slip ratio for two-phase orifice outlet conditions.

The data that were collected with the orifice with a large L/D were used to investigate the friction, acceleration, and gravity pressure losses. A model was developed in which the

empirical form loss model is applied at the orifice entrance, and the friction, acceleration, and gravity losses are integrated along the remaining length of the orifice. The HEM assumptions were used for two-phase conditions. A number of correlations for the friction factor were compared. All of the data collected with the orifice with a large L/D are predicted within five percent with this model when Colebrook's correlation for the friction factor is used.

The data that were collected throughout this study are useful for validating various models for the flow of S-$CO_2$ through orifices. They also provide a starting point for studies of the flow of S-$CO_2$ through more complex geometries such as annular orifices and labyrinth seals. The one-dimensional models that were developed and validated with the data are also useful for first approximations of valves, pipe ruptures, and turbomachinery seals. The critical mass flow rate and critical pressure ratio were determined for each test, and the raw data from this investigation are available on the internet.

## Acknowledgements

Although I am very proud of the results of the work that I have done for this degree, there are a handful of people without whom any of this would have been possible.

I would like to thank the U.S. Department of Energy for sponsoring my research and education through the NEUP program.

I want to thank my advisors, Professor Gregory Nellis and Professor Sanford Klein for being my mentors through courses and research during my undergraduate and graduate education. They are exceptional teachers and advisors, and they have shaped my interests and the ways in which I attack engineering problems in ways that I am certain will benefit me for the rest of my life. I would also like to thank Doctor Mark Anderson for overseeing the research project. He provided me with countless opportunities for growth through his knowledge of research and connections throughout the research world. The weekly presentations, expectations, and deadlines were intimidating at first, but it is now clear to me how valuable these experiences were to my growth as an independent problem solver.

I want to thank my parents for the countless sacrifices that they have made throughout my life in order to ensure that I would have opportunities that they never had. I am truly lucky to have been born to two people who put everything else on the backburner in order to focus on me the moment that I was born. I am forever indebted to them for making accomplishments like these possible. I also want to thank my sister for always

looking out for me and for showing me the right way to do so many things. I could not have asked for a better role model.

I have had the opportunity to work with some extraordinary students during the last year and a half. I want to thank Matt Wolf for being not only a great colleague and teaching me all kinds of useful hands on skills, but also a great friend. I am grateful that we were thrown off the deep end together. I also want to thank Haomin Yuan for sharing his wealth of theoretical knowledge with me. It has been a pleasure working with and getting to know him. Finally, I want to thank John Dyreby for all of his great advice. I appreciate him always taking time out of his day to answer my questions, and his advice about engineering and life is always helpful.

I want to thank all of the SEL students for making the last year and a half such a fun experience. My office mates, Doug, Wenjie, Kathryn and Evan, have always made work an enjoyable place to be. The SEL is a special place, and I am grateful for having had the opportunity to meet and spend time with so many great friends like Doug, Wenjie, Russell, Rogelio, Diego, Mohamed, Kyle, and many others. I am sure that all of them will do great things.

## Table of Contents

## Table of Figures

## List of Tables

# Nomenclature

**Abbreviations**

| | |
|---|---|
| ANL | Argonne National Laboratory |
| CFD | Computational Fluid Dynamics |
| DAQ | Data Acquisition System |
| EES | Engineering Equation Solver |
| HEM | Homogeneous Equilibrium Model |
| L/D | Length-to-Diameter Ratio |
| PID | Proportional Integral Derivative |
| RSS | Root-Sum Square |
| S-CO2 | Supercritical Carbon Dioxide |
| SFM | Separated Flow Model |
| SSTAR | Small, sealed, transportable, autonomous reactor |

**Variables**

| | |
|---|---|
| $C_C$ | Contraction Coefficient |
| $C_D$ | Discharge Coefficient |
| $\dot{W}$ | Power |
| $\dot{m}$ | Mass Flow Rate |
| $\dot{q}$ | Heat Transfer Rate |
| $\tau_w$ | Wall Shear Stress |
| $h$ | Specific Enthalpy |
| $A$ | Cross Sectional Area |
| $D$ | Diameter |
| $G$ | Mass Flux |
| $L$ | Length |
| $Maxspan$ | Maximum Span |
| $N$ | Number of points |
| $P$ | Pressure |
| $Range$ | Signal Range |
| $Re$ | Reynolds Number |
| $S$ | Slip Ratio |
| $T$ | Temperature |
| $V$ | Volume |
| $c$ | Sound Speed |
| $dz$ | Distance between nodes |
| $f$ | Darcy Friction Factor |
| $g$ | Gravitational Acceleration |
| $per$ | Perimeter |
| $s$ | Specific Entropy |
| $t$ | Student's t Distribution Value |
| $u$ | Velocity |
| $unc$ | Uncertainty |
| $v$ | Specific Volume |

| | |
|---|---|
| $x$ | Mass Averaged Quality |
| $z$ | Axial Position |
| $\alpha$ | Void Fraction |
| $\varepsilon$ | Surface Roughness |
| $\theta$ | Orientation Angle |
| $\mu$ | Dynamic Viscosity |
| $\rho$ | Density |

**Subscripts**

| | |
|---|---|
| $v_{95}$ | 95% Confidence Interval |
| $\Omega$ | Resistance |
| $P$ | Pressure |
| $PC$ | Pseudo-critical |
| $V$ | Voltage |
| $acc$ | Accuracy |
| $cal$ | Calibrated |
| $d$ | Downstream Stagnation Location |
| $da$ | Data Acquisition |
| $e$ | Exit Location |
| $f$ | Liquid Phase |
| $g$ | Vapor Phase |
| $ins$ | Instrument |
| $iso$ | Isothermal |
| $m$ | Mixture |
| $o$ | Upstream Stagnation Location |
| $prec$ | Precision |
| $r$ | Resolution |

# 1 Introduction

The Supercritical Carbon Dioxide (S-$CO_2$) Brayton Gas Turbine Cycle has been studied as an efficient and cost-effective option for producing power for several decades. However, until recently (within the last decade or so), a number of issues have prevented its full-scale implementation. For example, the low temperatures (below 500°C) of the heat sources used for the majority of large-scale power production are more suitable for traditional steam cycles than for the S-$CO_2$ Brayton Cycle in terms of thermal efficiencies. This has led to the optimization and establishment of the Rankine Cycle over the past century which has limited the development of alternative power cycles such as the S-$CO_2$ Brayton Cycle. Also, the unique properties and behavior of the working fluid, S-$CO_2$, have caused difficulties in the design and analyses of plant components such as heat exchangers, turbomachinery, valves, and seals.

In recent years, the push to design high temperature heat sources such as the Generation IV nuclear reactors [1] and concentrating solar power receivers, in addition to significant research on the properties and behavior of S-$CO_2$ ([2], [3],[4],[5],[6]), have generated renewed interest in the S-$CO_2$ Brayton Cycle as a means for producing power. Also, as a result of imminent carbon taxes, carbon emissions regulations, and increased costs associated with power production, the S-$CO_2$ Brayton Cycle is under consideration for use in fossil fuel power production [7] and waste heat recovery applications [8].

The S-$CO_2$ Brayton Cycle offers several advantages over both Rankine Cycles and other Brayton Cycles. For example, due to the high densities of $CO_2$ near its critical point, the S-$CO_2$ Brayton Cycle reduces the work required to compress the working fluid

(effectively reducing the back work ratio, defined as the compression work as a percentage of the turbine output), resulting in thermal efficiency gains. The high density of S-$CO_2$ also reduces the size of the turbomachinery required for the cycle, possibly resulting in lower capital costs. Although very little pumping power is required to compress liquid water in a Rankine Cycle, the presence of two-phase water within the cycle has disadvantages. Complex equipment is required to ensure that cavitation does not occur within the pumps and that droplets do not form on the turbine blades. In contrast, the S-$CO_2$ Brayton Cycle operates entirely above the critical point of $CO_2$, allowing the fluid (in this case, $CO_2$) to remain in a single phase throughout the cycle thereby eliminating the need for additional equipment required to deal with a two-phase fluid within the cycle.

The S-$CO_2$ Brayton Cycle also offers several advantages over the more developed Helium Brayton Cycle. For example, the relatively high turbine inlet temperature (approximately 900°C) of the Helium Brayton Cycle causes difficulties in the selection of structural materials; such difficulties may pose fewer challenges with the S-$CO_2$ Brayton Cycle, which operates at a much lower turbine inlet temperature (between 500°C and 700°C) [9]. In addition, the reduction in the back work ratio achieved by the S-$CO_2$ Brayton Cycle is greater than that achieved by the Helium Brayton Cycle [9].

Several aspects of the S-$CO_2$ Brayton Cycle still require significant research and development, and this study addresses one such challenge. The behavior of S-$CO_2$ as it flows through restrictions such as valves, turbomachinery seals, and pipe ruptures is not well understood, but the development of models describing these phenomena is integral

to the practical implementation of the S-$CO_2$ Brayton Cycle. For example, approximations for flow rates and pressure drops associated with valves and piping are necessary in computer models used for predicting the performance of the power cycle. Additionally, models for the flow of S-$CO_2$ through pipe ruptures are required for safety analyses, as in the case of a nuclear power plant application. Models such as these are also useful for the design of plant components, such as valves and turbomachinery seals.

The real gas behavior of $CO_2$ near the critical point and the presence of both single-phase and two-phase $CO_2$ during various processes create challenges in analytical and numerical modeling of the flow of S-$CO_2$ through restrictions, such as valves, turbomachinery seals, and pipe ruptures. Although the S-$CO_2$ Brayton Cycle operates entirely above the critical point, $CO_2$ may exist as either a single-phase or a two-phase fluid when exhausted from the cycle into a low pressure environment through a restriction. For example, when a pipe ruptures in the system, $CO_2$ is exhausted through a restriction in the pipe from a single-phase state in the supercritical region to a much lower pressure (e.g., atmospheric pressure or a vacuum), which results in single-phase $CO_2$ entering the restriction and two-phase $CO_2$ exiting the restriction.

Restrictions, such as valves, turbomachinery seals, and pipe ruptures, can often be modeled as simple orifices. The objective of this study is to collect and use experimental data to develop and validate one-dimensional models for the flow of S-$CO_2$ through orifices. These data and models are useful for the analyses of various components and processes within the S-$CO_2$ Brayton Cycle.

## 2 Background and Modeling Methodology

The simple configuration of the S-$CO_2$ Brayton Cycle consists of a compressor, a turbine, an electric generator, a precooler heat exchanger, a recuperator heat exchanger, and a primary heat exchanger. The simple cycle layout and the state points on a temperature-specific entropy diagram are shown in Figure 1. The S-$CO_2$ Brayton Cycle is not competitive with traditional steam cycles for large scale power generation in terms of thermal efficiency when it is used with lower temperature heat sources such as fossil fuels and light water nuclear reactors. However, due to the development of high temperature heat sources such as Generation IV nuclear reactors and solar power receivers, there is a renewed interest in the S-$CO_2$ Brayton Cycle as a means for power generation.

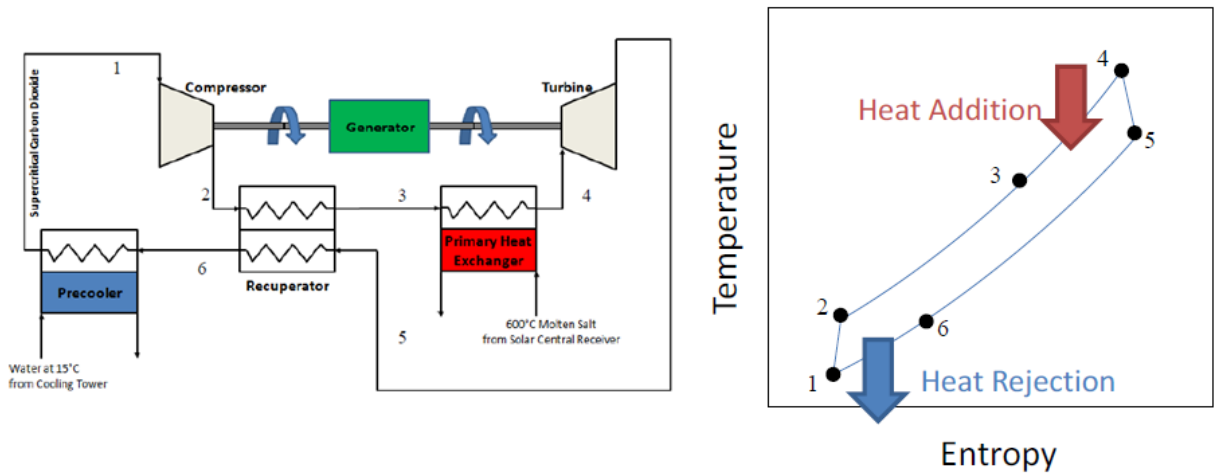


**Figure 1. Simple configuration of the S-$CO_2$ Brayton Cycle.[10].**

Dostal et al. [3, 9, 11] performed an extensive analysis of various configurations of the S-$CO_2$ Brayton Cycle, and recommended the recompression cycle configuration for heat sources above 500°C. The recompression cycle consists of main and recompressing compressors, a turbine, an electric generator, a precooler heat exchanger, high and low

temperature recuperator heat exchangers, and a primary heat exchanger. The layout is shown in Figure 2.

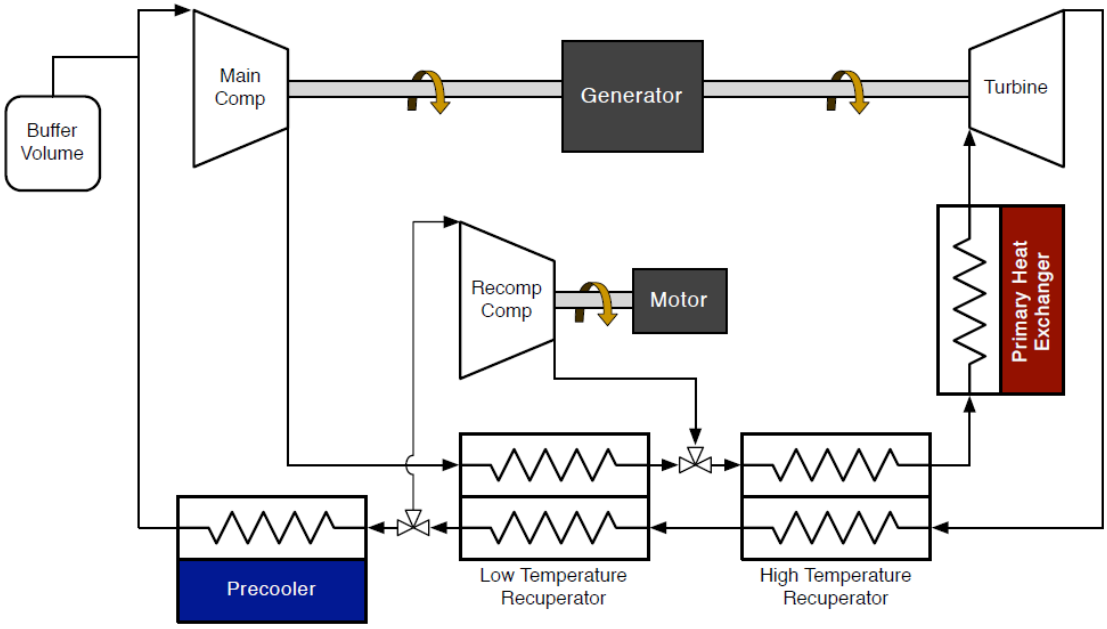


**Figure 2. S-$CO_2$ Brayton Recompression Cycle.**

## 2.1 S-$CO_2$ as a Working Fluid

The critical point of a fluid is defined by Klein and Nellis [12] as the point at which the first and second derivatives of pressure with respect to the volume at constant temperature are equal to zero, as shown in Equation (1).

$$\left.\frac{\partial P}{\partial V}\right|_T = 0 \qquad \left.\frac{\partial^2 P}{\partial V^2}\right|_T = 0 \tag{1}$$

There is no distinct separation between the phases of a fluid when either its temperature or pressure exceeds the respective critical value. Therefore, although the fluid remains in a single-phase, it may take on properties representative of either a gas or a liquid. In the

case of S-$CO_2$, unique fluid property variations occur near the critical point, and these variations can be both advantageous and disadvantageous for the design, analysis, and performance of the S-$CO_2$ Brayton Cycle. Figure 3, shows the specific heat capacity of $CO_2$ as a function of temperature for various pressures near the critical pressure. The pseudo-critical line is defined as the line that passes through the points in the supercritical region at which the specific heat capacity reaches a maximum value for a given pressure. As shown in the figure, the magnitudes of the variations in the specific heat capacity along the pseudo-critical line increase as the pressure approaches the critical pressure (7.38 MPa). The Engineering Equation Solver (EES) software package [13] was used to calculate fluid properties. EES was also used to create all of the original plots in this document.

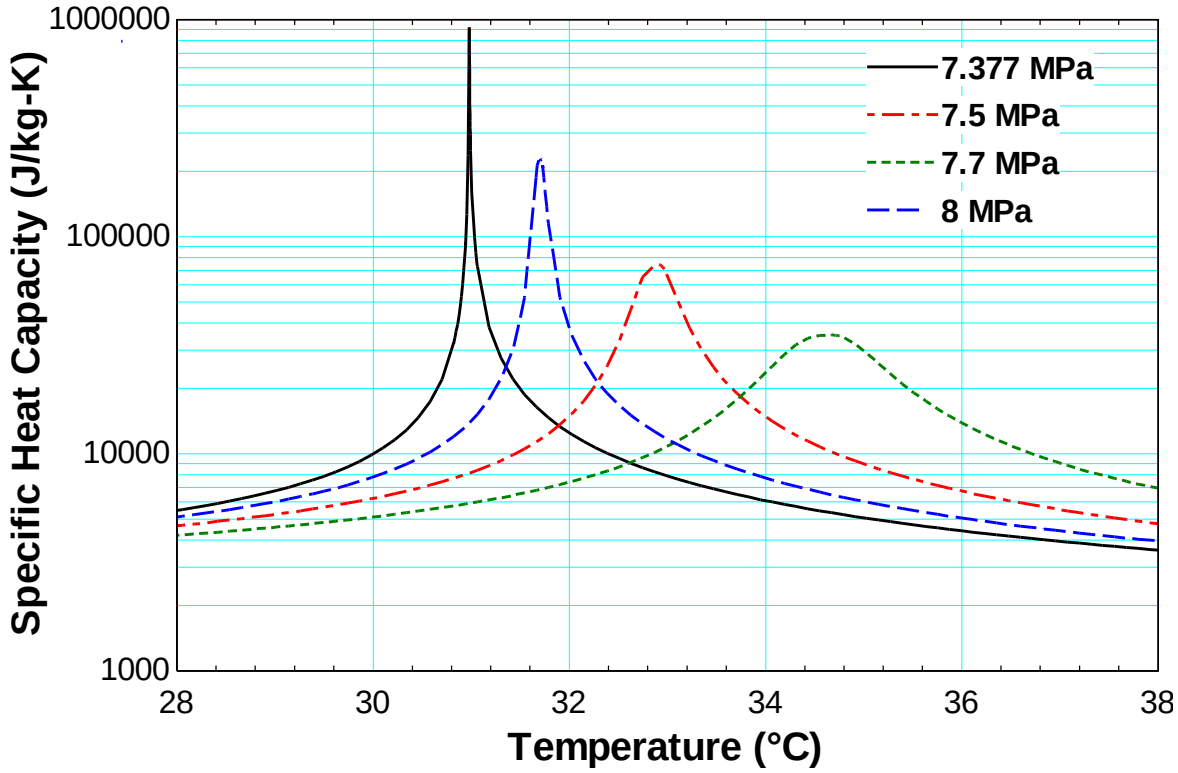

**Figure 3. Specific heat capacity of $CO_2$ as a function of temperature for various pressures in the supercritical region.**

The pseudo-critical line for S-$CO_2$ can be determined with curve fits to property data. The curve fit used throughout this study was developed by Carlson [14], and it is shown in Equation (2) where $P$ is in MPa and $T_{PC}$ is in °C. This relationship is valid for pressures between the critical pressure (7.38 MPa) and 20 MPa, and it is based on a curve fit developed by Liao and Zhao [15] for pressures between the critical pressure and 10 MPa.

$$T_{PC} = -28.4 + 10.3P - 0.3359P^2 + 4.063E{-}3P^3 \qquad (2)$$

Unique variations in other properties of $CO_2$ also occur near the critical point. Figure 4 shows the pseudo-critical line and the density of $CO_2$ as a function of temperature for various pressures in the supercritical region. Near the critical point (7.38 MPa, 30.98 °C), the density of $CO_2$ changes drastically with temperature. This is beneficial for the S-$CO_2$ Brayton Cycle in terms of the thermal efficiency because the density of the fluid in the compressor can be very large.

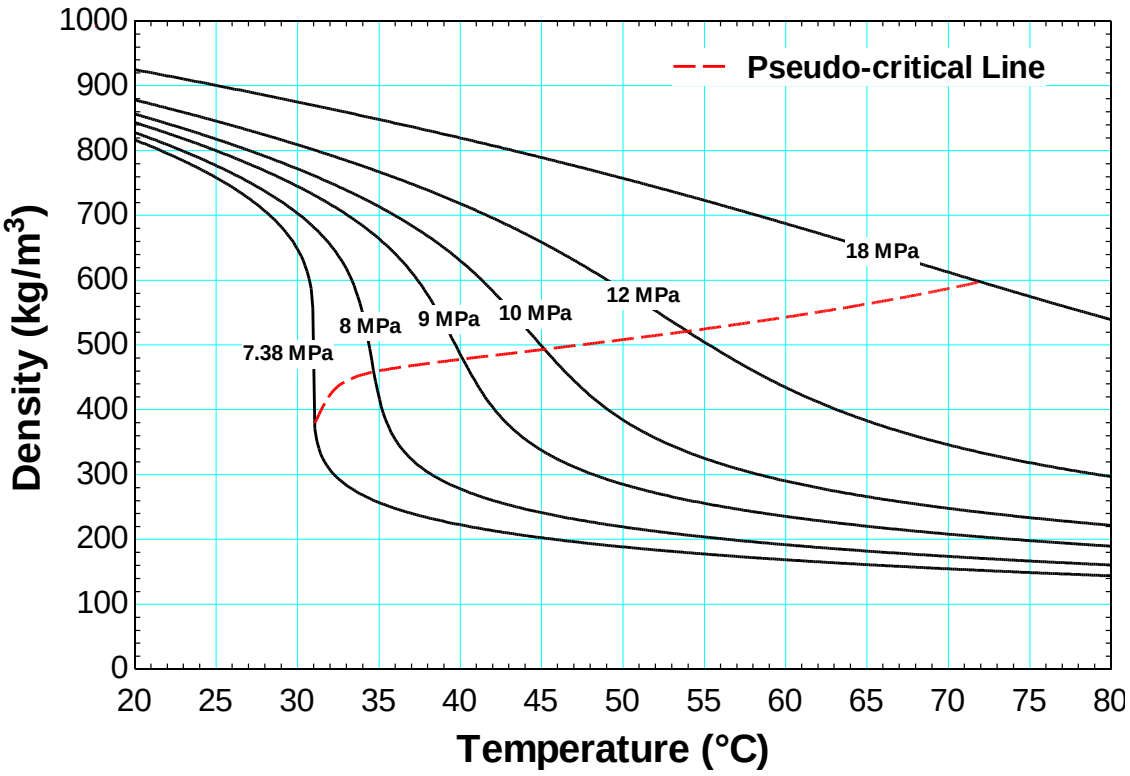


**Figure 4. Density of $CO_2$ as a function of temperature for various pressures in the supercritical region.**

The work required by a compressor or the work extracted from a turbine can be related to the fundamental property relation for specific enthalpy, specific entropic, and specific volume, as shown in Equation (3). The limiting processes of compression and expansion are isentropic (i.e., reversible and adiabatic); the work associated with an isentropic process is equivalent to the integral of the specific volume with respect to pressure. Therefore, for a given pressure ratio across a piece of turbomachinery, the work is directly proportional to the change in specific volume or the change in density of the fluid.

$$dh = T\underbrace{ds}_{0} + vdP \tag{3}$$

For gas turbine cycles, the work required to compress the working fluid can be significant in comparison to the work extracted from turbine, since the working fluid is a compressible gas that remains in single phase (i.e. the density of the fluid in the compressor and turbine are not all that different). The significance of the required compressor power is quantified by the back work ratio, which is defined as the ratio of the power required to compress the working fluid (compressor power) to the power extracted from the expansion of the fluid (turbine power), as shown in Equation (4).

$$Back\ Work\ Ratio = \frac{\dot{W}_{compressor}}{\dot{W}_{turbine}} \tag{4}$$

An effective method for increasing the thermal efficiency of a gas turbine cycle is to reduce the back work ratio. The S-$CO_2$ Brayton Cycle takes advantage of this method. By operating the compressor near the critical point of $CO_2$, the density of the fluid in the compressor can be much larger than the density of the fluid in the turbine, resulting in a reduction in the work required to compress the $CO_2$ and the back work ratio. This concept is illustrated in Figure 5, which shows the density of $CO_2$ as a function of temperature for various pressures in the supercritical region with the compressor and turbine inlet and outlet states for the simple cycle analyzed by Dostal et al. [3] labeled.

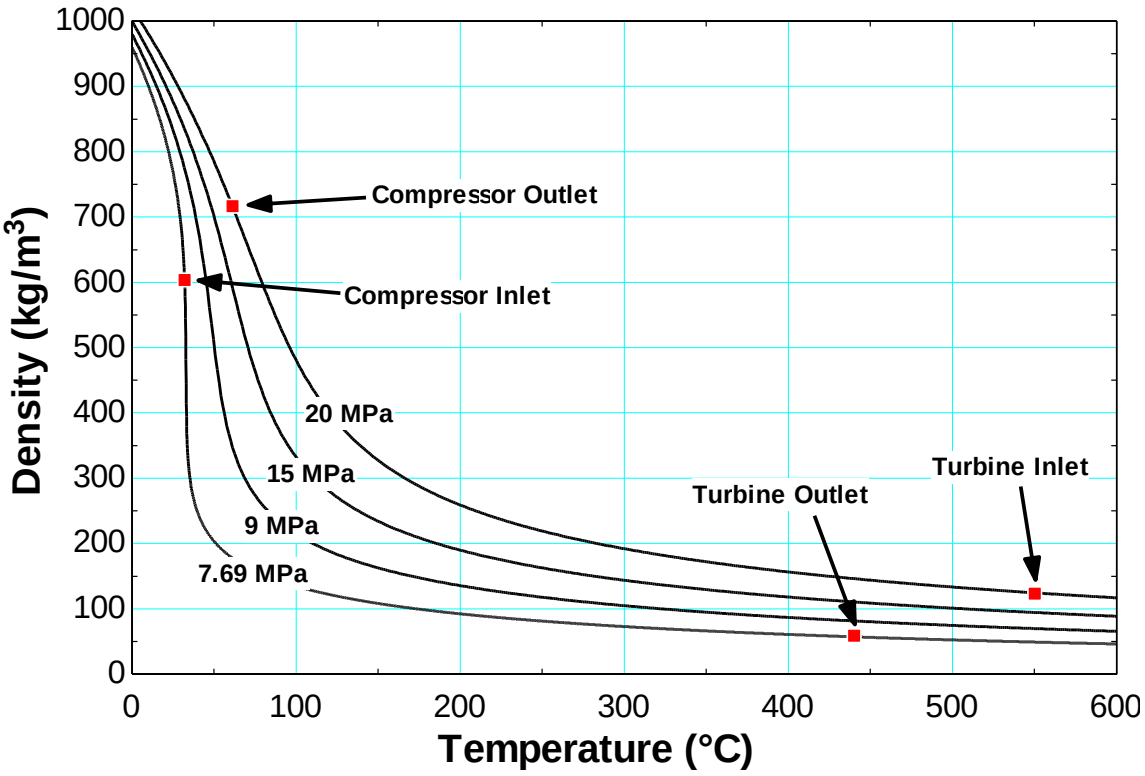


**Figure 5. Density of $CO_2$ as a function of temperature for various pressures in the supercritical region with the compressor and turbine inlet and outlet conditions for Dostal's simple S-CO2 Brayton Cycle labeled [3].**

Other more developed gas turbine cycles such as the Helium Brayton Cycle operate in the ideal gas region, where fluid properties do not vary drastically. These cycles are unable to take advantage of an increased thermal efficiency by reducing the back work ratio in the same way that the S-$CO_2$ Brayton Cycle does [9].

In contrast to gas turbine cycles, the work required to pressurize incompressible liquid water in traditional steam cycles is negligible in comparison to the output of the turbine. However, the operation of the cycle across the two-phase region requires complex equipment in order to prevent cavitation within the pumps and the formation of droplets on the turbine blades. This equipment is not required by the S-$CO_2$ Brayton Cycle since

the working fluid remains in a single-phase with properties in the supercritical region throughout the cycle.

In addition to an increase in thermal efficiency, the high density of S-$CO_2$ also allows for a reduction in the size of the turbomachinery required for the cycle. As can be observed in Figure 4, the density of S-$CO_2$ is quite high, even approaching the density of liquid water for various pressures and temperatures in the supercritical region. The high density substantially reduces the size of the turbomachinery required for the cycle, as can be seen in Figure 6, which shows a comparison of the sizes of a steam turbine, a Helium turbine, and a S-$CO_2$ turbine [11].

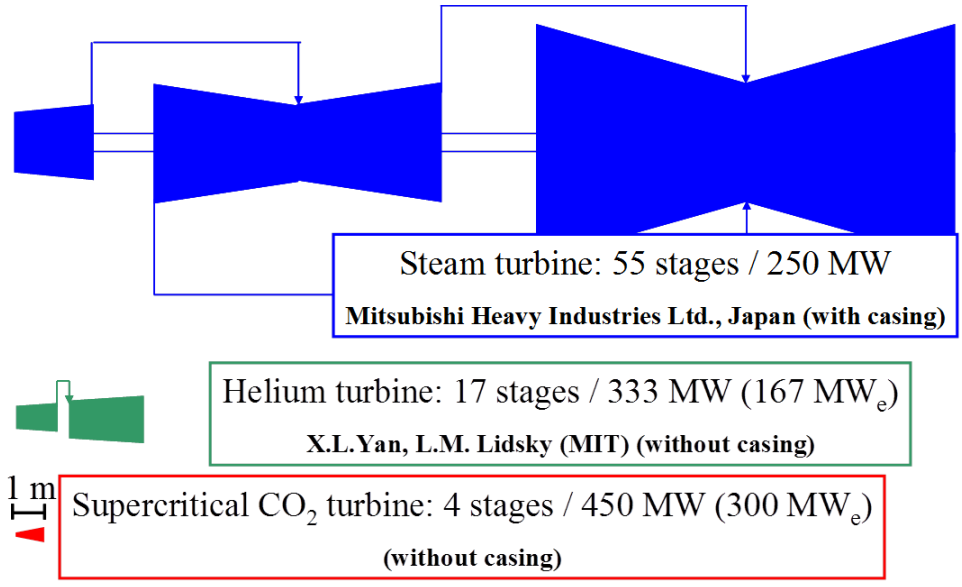


**Figure 6. Size comparison of a steam turbine, a helium turbine, and a S-CO2 turbine [11].**

Although the unique property behavior of S-$CO_2$ is advantageous within the S-$CO_2$ Brayton Cycle (i.e., in terms of efficiency and capital costs, as discussed above), this behavior presents significant challenges for those analyzing and designing components of the cycle.

Figure 7 illustrates the compressibility factor of $CO_2$ as a function of temperature for various pressures in the supercritical region. As illustrated in Figure 7, the compressibility of $CO_2$ near the critical point and along the pseudo-critical line is low. Thus, for purposes of engineering analysis, the $CO_2$ must be treated as a real gas rather than an ideal gas at these conditions.

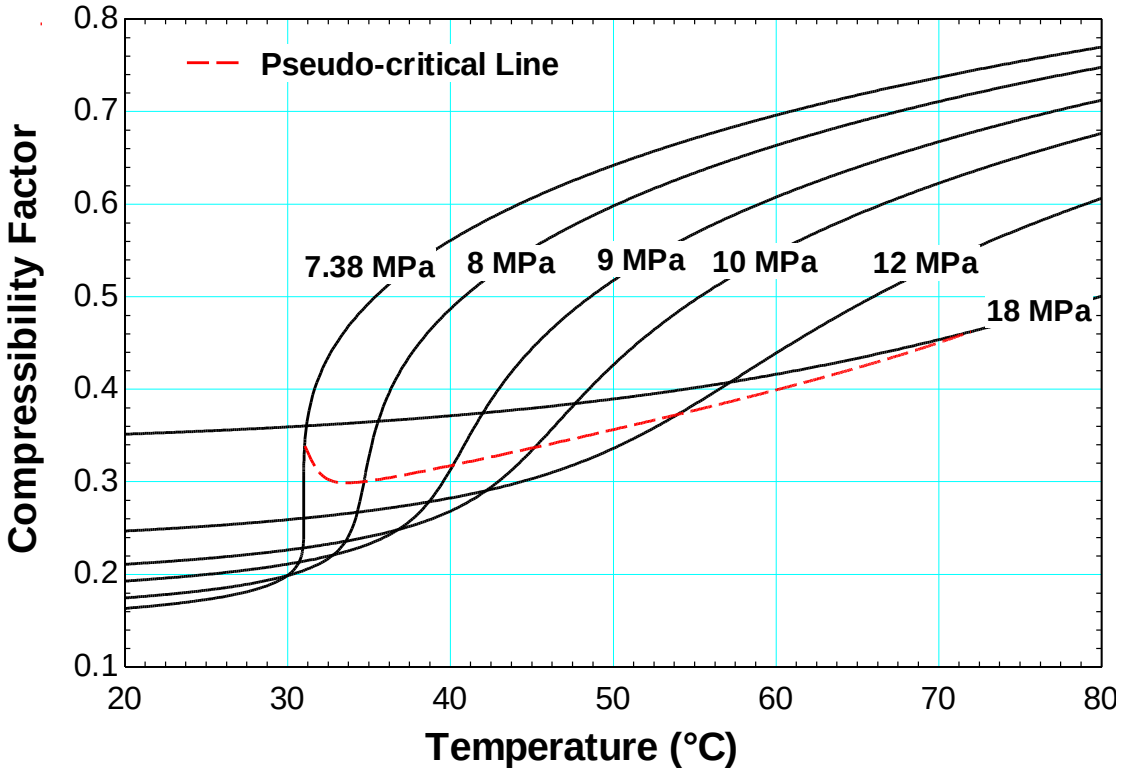


**Figure 7. Compressibility factor of $CO_2$ as a function of temperature for various pressures in the supercritical region.**

For all of the reasons discussed (i.e., unique property variations, real gas behavior, high temperatures and pressures), the behavior of S-$CO_2$ flowing through restrictions such as valves, pipe ruptures, and turbomachinery seals is not well understood. However, experimentally validated models, both one-dimensional and multi-dimensional, that

describe the physics of these processes are essential for the practical implementation of the S-$CO_2$ Brayton Cycle as a competitive means for producing power.

## 2.2 Restrictions of Interest

A variety of restrictions with different geometries and applications exist within the S-$CO_2$ Brayton Cycle. Figure 8 shows a diagram of the simple configuration of the S-$CO_2$ Brayton Cycle Plant Dynamics Code developed at Argonne National Laboratory (ANL) [16]. The cycle model utilizes a variety of valves for control, but models for the flow of S-$CO_2$ through valves restrictions have not been developed and existing models developed for other fluids have not have validated with experimental data for S-$CO_2$. Therefore, it is possible that the models used for valves in systems codes such as the one developed at ANL could introduce large errors into cycle performance approximations. Models for the flow of S-$CO_2$ through restrictions resembling valves are also necessary for the practical design of valves for use within the power cycle.

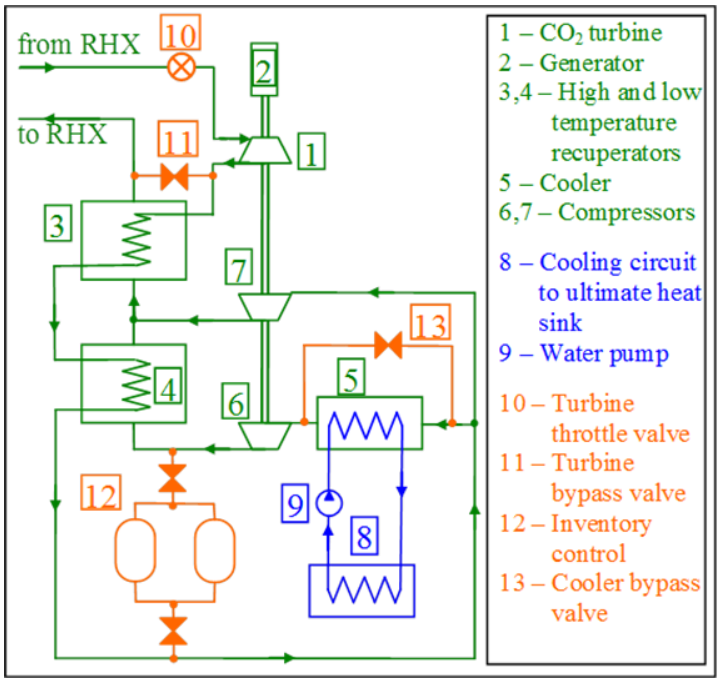


**Figure 8. Diagram of simple configuration of S-$CO_2$ Brayton Cycle Plant Dynamics Code developed at Argonne National Laboratory (ANL) [17].**

Figure 9 shows a diagram of the recompression configuration of the S-$CO_2$ Brayton Cycle Plant Dynamics Code developed at ANL for use with the SSTAR lead fast reactor. In the nuclear industry, significant analyses are performed on accident scenarios. Many of these scenarios involve a pipe rupture within the system through which coolant is expelled, resulting in a rise in the temperature of the reactor core and a risk of core meltdown. In order to accurately predict the behavior of the system when a pipe ruptures, it is essential to have models for predicting the rate at which coolant is expelled. Currently, this analysis is difficult to perform for the S-$CO_2$ Brayton Cycle due to a lack of understanding of the behavior of S-$CO_2$ flowing through pipe ruptures.

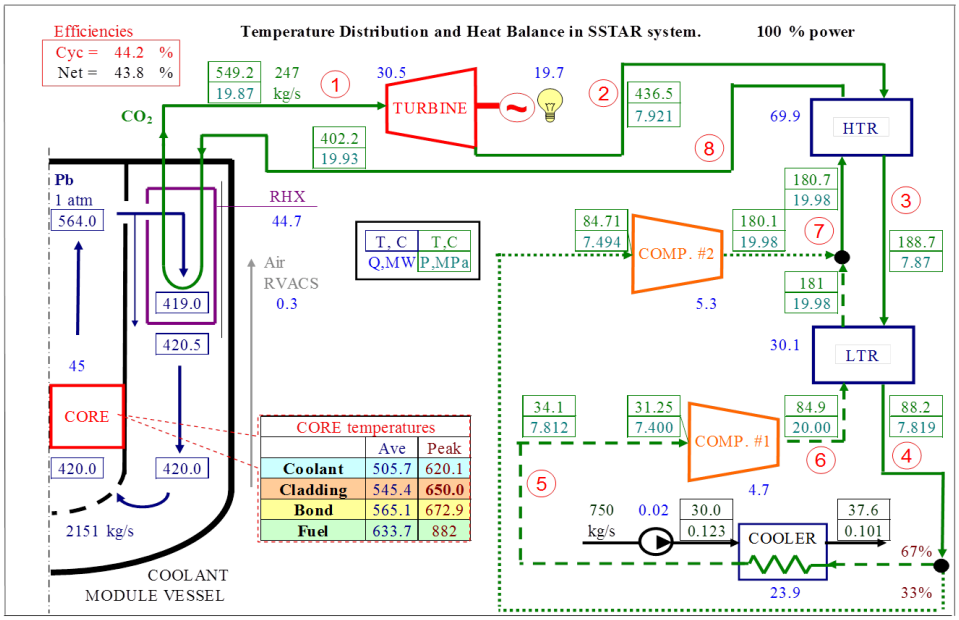


**Figure 9. Diagram of recompression configuration of S-$CO_2$ Brayton Cycle Plant Dynamics Code developed at ANL for use with the SSTAR lead fast reactor [17].**

Another application for which models for the flow of S-$CO_2$ through restrictions are essential is turbomachinery sealing. Figure 10 shows the simple configuration of the S-$CO_2$ Brayton Cycle in which the compressor, turbine, and generator share a common shaft. In order to reduce the frictional losses within the generator, it is necessary to maintain a low pressure within the generator cavity. However, it is difficult to create a seal between the turbomachinery wheels, which contain high pressure S-$CO_2$, and the generator cavity due to the rotating shaft connection. Therefore, an additional compressor is required to maintain the low pressure within the generator cavity by removing any S-$CO_2$ that leaks from the turbomachinery into the generator cavity. The resulting power required to operate the additional compressor acts to reduce the overall efficiency of the cycle, so it is essential to minimize the amount of S-$CO_2$ leakage from the turbomachinery.

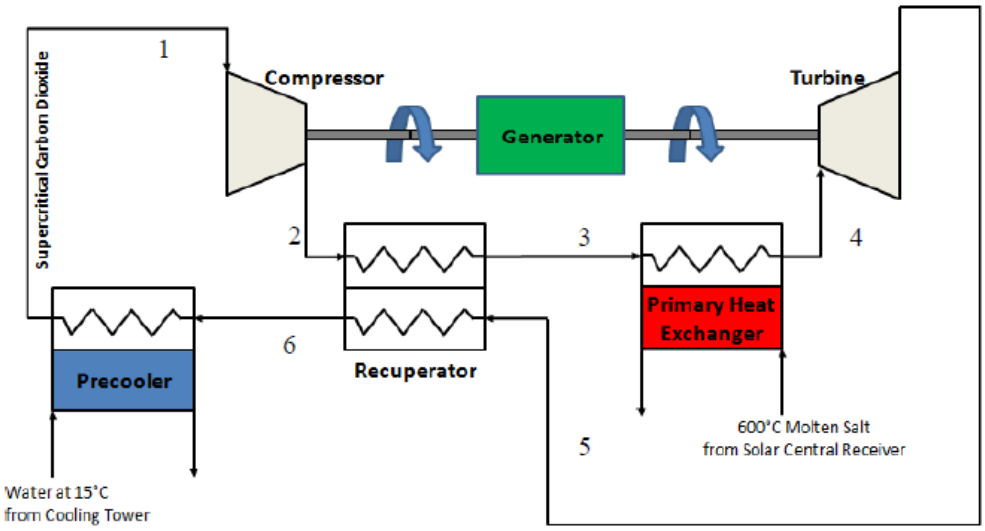


**Figure 10. Simple configuration of the S-$CO_2$ Brayton Cycle [10].**

Labyrinth seals provide one solution to the leakage problem. These seals consist of a series of teeth and cavities placed along the rotating shaft between the turbomachinery and the generator cavity with the purpose of minimizing the fluid flow rate, as shown in Figure 11. It is essential to have an understanding of the flow of S-$CO_2$ through restrictions in order to effectively design labyrinth seal geometries for specific applications.

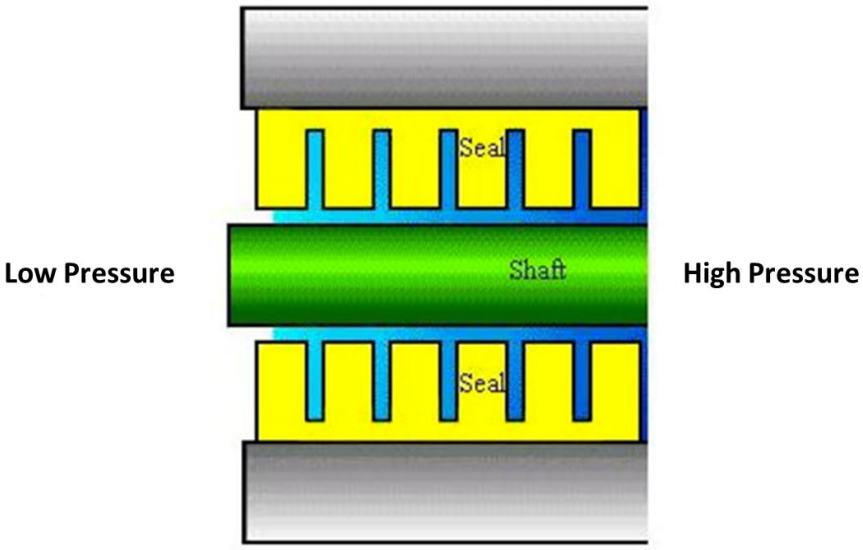


**Figure 11. Labryinth seal [18].**

Many of the restriction geometries of interest for the S-$CO_2$ Brayton Cycle can be modeled as simple orifices for a first approximation. Therefore, it is necessary to gain an understanding of simple orifice geometries prior to moving on to more complex geometries such as labyrinth seals. This study focuses on creating new one-dimensional models and validating existing one-dimensional models based on experimental data for the flow of S-$CO_2$ through sharp-edged orifices.

## 2.3 Overview of Pressure Losses in an Orifice

The total pressure drop for a fluid flowing through an orifice is the sum of the minor pressure losses and the major pressure losses, as represented by Equation (5). The minor pressure losses, also known as form losses, result from the contraction and expansion of the fluid flowing through the orifice as it encounters the sudden restriction in flow area at the orifice entrance. The major pressure losses result from friction, acceleration of the

fluid through the orifice, and gravitational force on the fluid along the length of the orifice.

$$\Delta P = \underbrace{\sum \Delta P_{form}}_{Minor\ Losses} + \underbrace{\sum \Delta P_{friction} + \sum \Delta P_{acceleration} + \sum \Delta P_{gravity}}_{Major\ Losses} \quad (5)$$

Figure 12 illustrates a fluid ($CO_2$ in this case) flowing through a sharp-edged orifice. Upon entering the orifice at point (2), the $CO_2$ contracts to a flow area that is smaller than that of the orifice since the streamlines of the $CO_2$ cannot change direction abruptly. The point at which the flow area reaches a minimum is known as the vena contracta and is represented by point (3) in Figure 12. After reaching the vena contracta, the $CO_2$ expands until it reattaches to the wall of the orifice, represented by point (4) in Figure 12. The form loss of the $CO_2$ is equivalent to the pressure loss associated with the contraction and the expansion of the $CO_2$ from the orifice entrance, point (2), to the point of reattachment to the orifice wall, point (4). At the point of reattachment the pressure drop resulting from the form loss has occurred and the friction, acceleration, and gravity pressure losses become dominant. The objective of this study is to develop and validate models for the minor and major losses associated with flow of S-$CO_2$ through sharp-edged orifices.

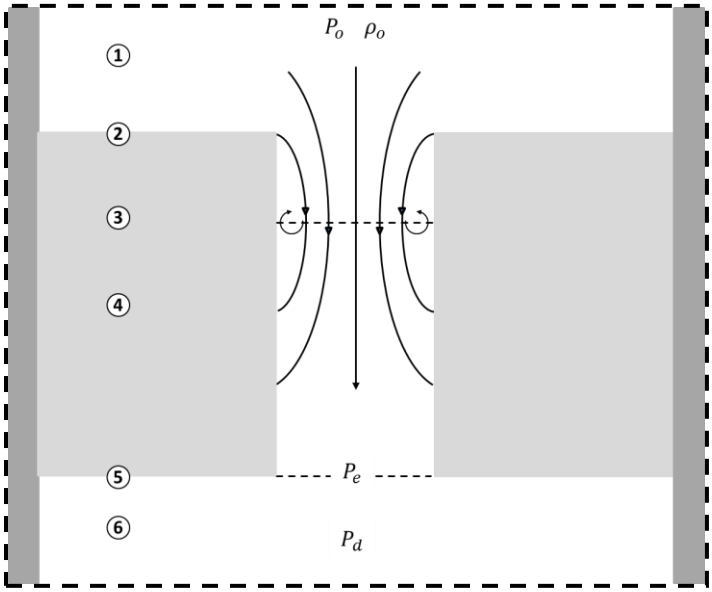


**Figure 12. Flow of fluid through a sharp-edged orifice.**

## 2.4 Critical Flow

The maximum mass flow rate that can be achieved by a fluid flowing through a converging nozzle or orifice is referred to as the critical mass flow rate. Critical flow occurs when the bulk velocity of the fluid reaches the local speed of sound, which is defined as the square root of the derivative of pressure with respect to density at constant specific entropy [19], as shown by Equation (6).

$$c^2 = \left.\frac{\partial P}{\partial \rho}\right|_s \tag{6}$$

Figure 13 shows the mass flow rate (in arbitrary units) of a fluid through an orifice as a function of pressure ratio. The pressure ratio is defined as the ratio of the downstream stagnation pressure to the upstream stagnation pressure. For constant upstream conditions, as the downstream stagnation pressure is reduced (i.e., the pressure ratio is reduced), the mass flow rate and the velocity of the fluid increase until the bulk velocity

of the fluid reaches the local speed of sound. Any decrease in the downstream stagnation pressure after the bulk velocity of the fluid reaches the local speed of sound has no effect on the mass flow rate of the fluid through the orifice. This is due to the inability of the downstream stagnation pressure information to be communicated upstream since pressure waves travel at the local speed of sound. The pressure ratio at which critical flow occurs is referred to as the critical pressure ratio [19]. The critical mass flow rate and the critical pressure ratio are important engineering quantities in the analysis of pipe ruptures, valves, and turbomachinery seals.

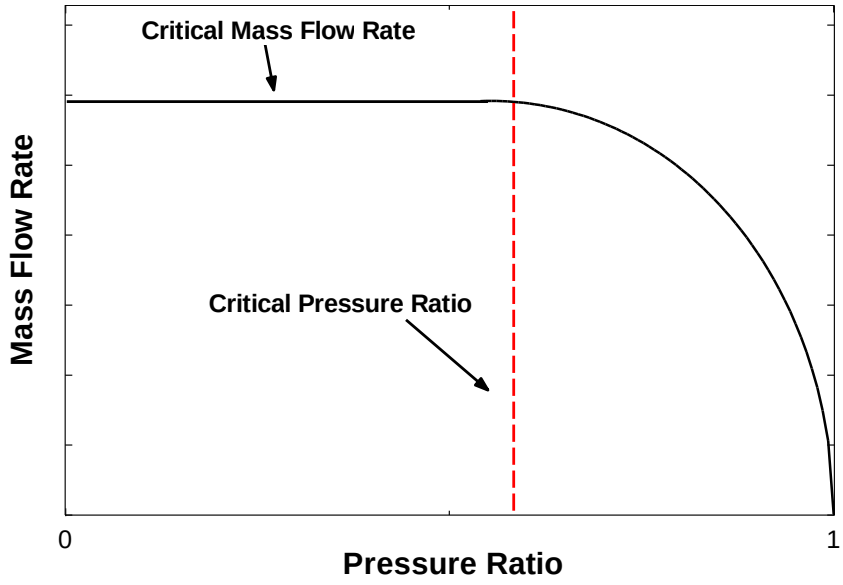


**Figure 13. Mass flow rate (arbitrary units) as a function of pressure ratio for an orifice (typical).**

## 2.5 Two-phase flow

Although the S-$CO_2$ Brayton Cycle operates entirely above the critical point of $CO_2$, there are still applications within the cycle for which both single-phase and two-phase flow of $CO_2$ through restrictions will occur. For example, when high pressure S-$CO_2$ is

exhausted through a turbomachinery seal into the generator cavity, S-$CO_2$ enters the seal restriction as a single-phase fluid, but reaches two-phase conditions at some point further downstream as it expands to lower pressures. This concept is illustrated in Figure 14, which shows results from three tests performed for this study. Figure 14a shows the orifice inlet conditions for the three tests as squares (held constant throughout the test) and the orifice outlet conditions at which mass flow rate measurements were recorded as circles on a temperature-specific entropy diagram. The resulting mass flow rate measurements as a function of the pressure ratio are shown in Figure 14b. The figure shows that for high pressure ratios only single-phase S-$CO_2$ exists within the orifice, but as the orifice outlet pressure enters the two-phase region, both single-phase and two-phase flow of $CO_2$ occurs within the orifice. This behavior must be captured in models in order to accurately predict the flow of S-$CO_2$ through orifices.

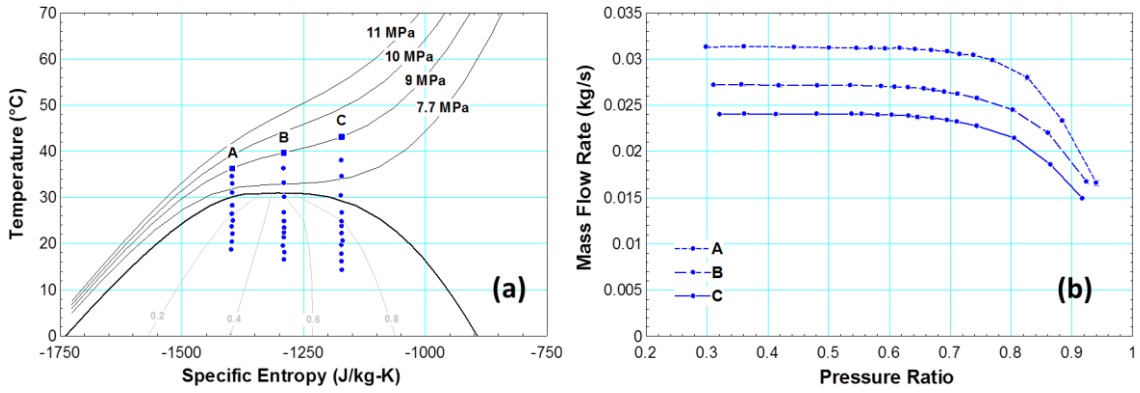


**Figure 14. Three sets of test conditions: (a) temperature-specific entropy diagram (b) the respective mass flow rate measurements as a function of pressure ratio.**

## 2.6 Form Losses

Form losses are most commonly characterized by a loss coefficient, which is analytically, numerically, or empirically determined. The loss coefficient represents the ratio of the

actual mass flow rate through a restriction to the mass flow rate calculated by an ideal model. In the case of S-$CO_2$ flowing through a sharp-edged orifice, the ideal model is some form of the isentropic model for the expansion of a fluid through a nozzle.

Figure 15 shows a converging nozzle. By assuming that the process is adiabatic and frictionless and that the nozzle is designed in a way such that the fluid streamlines follow its curvature, then the mass flow rate through the nozzle can be calculated with an isentropic model for the expansion of a fluid through a converging nozzle.

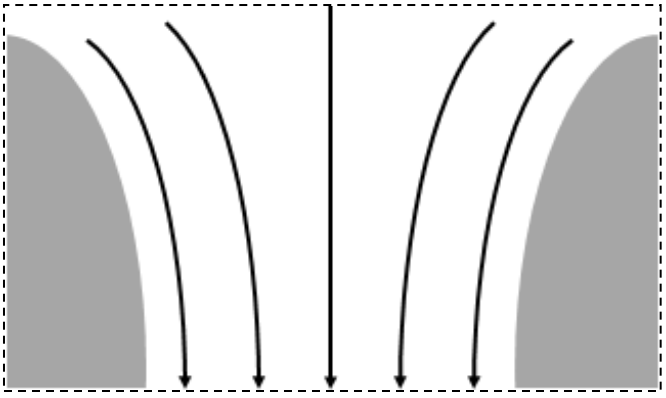

**Figure 15. Converging nozzle.**

The isentropic mass flow rate represents an upper bound on the actual mass flow rate through a sharp-edged orifice. In contrast to the case of the ideal converging nozzle, the streamlines of the fluid flowing through a sharp-edged orifice are unable to follow the sharp geometry of the restriction and the process is not adiabatic and frictionless. The result is a contraction of the fluid to the point of the vena contracta followed by an expansion of the fluid to the point of reattachment to the orifice wall, as shown in Figure 16. The resulting form loss is characterized by a loss coefficient between 0 and 1. The loss coefficient is multiplied by the isentropic mass flow rate that would occur in an ideal

converging nozzle for the same inlet and outlet conditions in order to determine the actual mass flow rate.

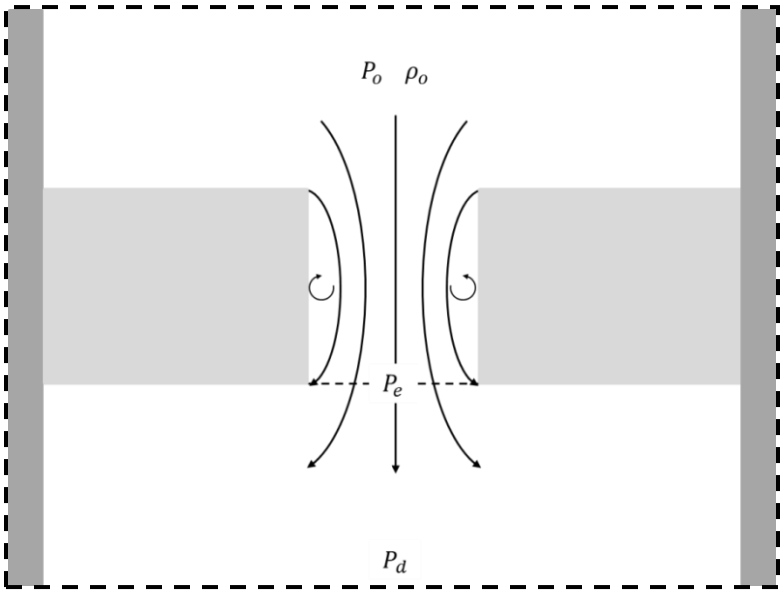


**Figure 16. Short, sharp-edged orifice.**

The contraction coefficient and the discharge coefficient are common loss coefficients used to characterize form losses for orifices. The contraction coefficient is most often determined analytically or numerically because it is difficult to measure experimentally. It is defined as the ratio of the area of the vena contracta to the area of the orifice, as shown in Equation (7). Determining the contraction coefficient is difficult, especially for a fluid with unique property variations such as S-$CO_2$.

$$C_c = \frac{A_{vena\ contracta}}{A_{orifice}} \tag{7}$$

The most common method used for characterizing form losses for orifices is to determine an empirical discharge coefficient. The discharge coefficient is defined as the ratio of the

experimentally measured mass flow rate to the calculated isentropic mass flow rate of a fluid flowing through a restriction, as shown in Equation (8).

$$C_D = \frac{\dot{m}_{measured}}{\dot{m}_{isentropic}} \tag{8}$$

An orifice with a small L/D is used to determine the measured flow rate in Equation (8) in order to isolate the form loss by ensuring that friction, acceleration, and gravity losses are very small. The following sections describe various methods for calculating the isentropic mass flow rate in Equation (8) as applied to the flow of S-$CO_2$ through sharp-edged orifices.

### 2.6.1 One-Dimensional Single-Phase Isentropic Model

The one-dimensional continuity, momentum, and energy equations for single-phase internal flow are shown in Equations (9), (10), and (11), respectively [20]. For a short, ideal, converging nozzle (i.e., adiabatic and frictionless), the friction and gravity terms of the momentum equation can be neglected and the potential energy, work, and heat transfer terms of the energy equation can be neglected. Therefore, the pressure drop within the nozzle is entirely due to the acceleration of the fluid. For a given pressure drop, the isentropic mass flow rate through the converging nozzle can be found by solving the energy equation and the continuity equation simultaneously.

$$\boldsymbol{Continuity}: \dot{m} = \rho u A = constant \tag{9}$$

$$\boldsymbol{Momentum}: \frac{dP}{dz} = -\underbrace{\underbrace{\frac{per}{A}\tau_w}_{0}}_{friction} \underbrace{-\frac{\dot{m}}{A}\frac{du}{dz}}_{acceleration} - \underbrace{\underbrace{\cancel{\rho g \cos\theta}}_{0}}_{gravity} \tag{10}$$

$$\boldsymbol{Energy}: \underbrace{\frac{d\dot{q}}{dz}}_{0} - \underbrace{\frac{d\dot{W}}{dz}}_{0} = \dot{m}\frac{d}{dz}\left(h + \frac{u^2}{2} + \underbrace{gz}_{0}\right) \tag{11}$$

### 2.6.2 Short Orifice Single-Phase Modeling Methodology

A more practical explanation for applying mass and energy balances to the isentropic flow of single-phase $CO_2$ through a converging nozzle with the purpose of determining a discharge coefficient is useful. Assuming the flow area upstream of the nozzle is significantly larger than the flow area of the nozzle itself (the nozzle area is equivalent to the area of the orifice through which the mass flow rate is experimentally measured), the upstream velocity of the $CO_2$ is negligible. Therefore, the upstream properties of the $CO_2$ are characterized as stagnation properties. In the experiment used to obtain data for this study, the stagnation pressure and stagnation density are measured and used to calculate other stagnation properties, as represented by Equation (12). Because the compressibility factor of $CO_2$ is low in the regions of interest (i.e., supercritical), real gas properties are used rather than ideal gas properties. In this study, all thermodynamic property calculations were performed using the Engineering Equation Solver (EES) software package [13].

$$P_o = Measured;\ \ \rho_o = Measured;\ h_o = f(P_o, \rho_o);\ s_o = f(P_o, \rho_o) \tag{12}$$

Because the steady state process of $CO_2$ flowing through an orifice occurs rapidly, the process is assumed to be adiabatic. The isentropic assumption can be applied by additionally assuming that there is no entropy generation due to friction effects or a shock wave. The isentropic model assumption is therefore only valid up to the point where the flow chokes and a shock wave occurs. If the process is isentropic, an entropy

balance requires that the downstream entropy be equal to the upstream entropy. The downstream pressure is measured in the experiment. Thus, the remaining downstream properties can be calculated using the downstream entropy and the downstream pressure, as represented by Equation (13).

$$s_d = s_o;\;\; P_d = Measured;\;\; \rho_d = f(s_d, P_d);\;\; h_d = f(s_d, P_d) \tag{13}$$

Using the known upstream stagnation and downstream enthalpies, the downstream velocity is calculated with an energy balance on the orifice according to Equation (14).

$$h_o = h_d + \frac{u_d^2}{2} \tag{14}$$

Finally, the isentropic mass flow rate for the given set of flow conditions (e.g., upstream stagnation pressure, upstream stagnation density, downstream pressure) is defined as the product of downstream density, downstream velocity, and nozzle (orifice) area, as represented by Equation (15). This value is substituted into Equation (8) along with the experimentally measured mass flow rate in order to determine the single-phase discharge coefficient.

$$\dot{m}_{isentropic} = \rho_d u_d A_{orifice} \tag{15}$$

### 2.6.3 One-Dimensional Isentropic Homogeneous Equilibrium Model (HEM)

It is necessary to use an isentropic model that accounts for two-phase flow when it occurs. This study focuses on applications for which the inlet conditions to the orifice are in the supercritical region and the outlet conditions are in either single-phase regions (i.e., supercritical, superheated vapor, sub-cooled liquid) or the two-phase region. The single-

phase one-dimensional isentropic model discussed in the previous section is applicable to the former cases, but a different isentropic model is required for the latter case.

The simplest method for modeling one-component two-phase flow is to assume that the velocities, temperatures, and pressures of the phases are equal. These assumptions define the Homogeneous Equilibrium Model (HEM). The isentropic HEM is identical to the single-phase isentropic model with the exception of the method for determining fluid properties. The continuity, momentum, and energy equations remain the same, and the practical method for applying these equations remains the same, but the two-phase fluid is treated as a single-phase fluid with mixture properties. Mixture properties are average properties based on the masses, areas, or volumes of the phases. For example, the two-phase mass-averaged mixture density is defined by Equation (16), and the two-phase mass-averaged mixture enthalpy is defined by Equation (17).

$$\rho_m = \frac{1}{\frac{x}{\rho_g} + \frac{1-x}{\rho_f}} \tag{16}$$

$$h_m = xh_g + (1-x)h_f \tag{17}$$

Mixture properties can also be based on the volume fractions of the phases, area fractions of the phases, or other correlations. The continuity, momentum, and energy equations for one-dimensional isentropic two-phase flow through a short, ideal, converging nozzle with HEM assumptions and mass-averaged mixture properties are shown in Equations (18), (19), and (20), respectively [20]. It is important to note that the isentropic HEM model collapses to the single-phase isentropic model for exclusively single-phase flow.

$$\boldsymbol{Continuity}: \dot{m} = \frac{1}{\left[\frac{x}{\rho_g} + \frac{1-x}{\rho_f}\right]} uA \tag{18}$$

$$\boldsymbol{Momentum}: \frac{dP}{dz} = -\underbrace{\frac{per}{A}\underbrace{\tau_w}_{0}}_{friction} - \underbrace{\frac{\dot{m}}{A}\frac{du}{dz}}_{acceleration} - \underbrace{\underbrace{\left(\frac{x}{\rho_g} + \frac{1-x}{\rho_f}\right)^{-1} g\cos\theta}_{0}}_{gravity} \tag{19}$$

$$\boldsymbol{Energy}: \frac{1}{\dot{m}}\left(\underbrace{\frac{d\dot{q}}{dz}}_{0} - \underbrace{\frac{d\dot{W}}{dz}}_{0}\right) = \frac{d}{dz}\left[xh_g + (1-x)h_f\right] + \frac{d}{dz}\left(\frac{u^2}{2}\right) + \underbrace{g\cos\theta}_{0} \tag{20}$$

### 2.6.4 One-Dimensional Isentropic Separated Flow Models

Many applications require better approximations than the one-dimensional isentropic HEM provides. For these applications, various separated flow models exist. The degrees to which these models capture the physics of the problem are dependent upon the number of equilibrium assumptions that are made. Commonly, the first equilibrium assumption to relax is the assumption of equal velocities of the phases. In this case, the pressures and temperatures of the phases are assumed to be equal, so mixture properties are used. However, the phases are assumed to flow at different velocities through separate flow areas. The continuity, momentum, and energy equations for one-dimensional isentropic two-phase flow through a short, ideal, converging nozzle assuming equal pressures and temperature of the phases and different velocities of the phases with mass-averaged mixture properties are shown in Equations (21), (22), and (23), respectively [20]. This model is referred to as a separated flow model in which the phases are considered together.

$$\boldsymbol{Continuity}:$$
$$\dot{m}_g = \rho_g A_g u_g$$
$$\dot{m}_f = \rho_f A_f u_f \tag{21}$$
$$\dot{m} = \dot{m}_g + \dot{m}_f$$

$$\boldsymbol{Momentum}: \frac{dP}{dz} = -\underbrace{\underbrace{\frac{per}{A}\cancel{\tau_w}}_{0}}_{friction} - \underbrace{\frac{\dot{m}}{A}\frac{d}{dz}\left[xu_g + (1-x)u_f\right]}_{acceleration} - \underbrace{\underbrace{\left(\frac{x}{\rho_g} + \frac{1-x}{\rho_f}\right)^{-1}\cancel{g\cos\theta}}_{0}}_{gravity} \tag{22}$$

$$\boldsymbol{Energy}: \frac{1}{\dot{m}}\left(\underbrace{\frac{d\cancel{\dot{q}}}{dz}}_{0} - \underbrace{\frac{d\cancel{\dot{W}}}{dz}}_{0}\right) = \frac{d}{dz}\left[xh_g + (1-x)h_f\right] + \frac{d}{dz}\left[x\frac{u_g^2}{2} + (1-x)\frac{u_f^2}{2}\right] + \underbrace{\cancel{g\cos\theta}}_{0} \tag{23}$$

### 2.6.5 Short Orifice Two-Phase Separated Flow Modeling Methodology

A more practical explanation for applying the mass and energy balances of the separated flow model in which the phases are considered together to the isentropic flow of $CO_2$ through a converging nozzle with the purpose of determining a discharge coefficient is useful. The upstream properties of the $CO_2$ are characterized as stagnation properties. The measured stagnation pressure and stagnation density are used to calculate other stagnation properties, as represented by Equation (24). It is important to note that for this study, the upstream properties are always in the supercritical region.

$$P_o = Measured;\ \ \rho_o = Measured;\ h_o = f(P_o, \rho_o);\ s_o = f(P_o, \rho_o) \tag{24}$$

The separated flow model in which the phases are considered together is utilized when the downstream conditions are in the two-phase region. If the process is isentropic, an entropy balance requires that the downstream entropy be equal to the upstream entropy. The downstream pressure is measured in the experiment. Thus, the downstream quality is calculated using the downstream entropy and downstream pressure, as represented by Equation (25).

$$s_d = s_o;\ \ P_d = Measured;\ \ x_d = f(s_d, P_d) \tag{25}$$

The downstream saturated liquid and saturated vapor densities and enthalpies are calculated using the downstream pressure, as shown in Equation (26).

$$\rho_{g,d} = f(P_d);\ \rho_{f,d} = f(P_d);\ \ h_{g,d} = f(P_d);\ \ h_{f,d} = f(P_d) \tag{26}$$

An energy balance on the nozzle using mass-averaged mixture properties and separate vapor and liquid velocities is shown in Equation (27).

$$h_o = \left[x_d h_{g,d} + (1 - x_d) h_{f,d}\right] + \left[x_d \frac{u_{g,d}^2}{2} + (1 - x_d) \frac{u_{f,d}^2}{2}\right] \tag{27}$$

Separate continuity equations are written for the vapor and liquid phases, as shown in Equations (28) and (29), respectively.

$$\dot{m}_g = \rho_{g,d} A_g u_{g,d} \tag{28}$$

$$\dot{m}_f = \rho_{f,d} A_f u_{f,d} \tag{29}$$

The overall isentropic mass flow rate is the sum of the vapor and liquid mass flow rates, and the total flow area is the sum of the vapor and liquid flow areas, as shown in Equations (30) and (31), respectively. The total flow area is known, and it is equivalent to the area of the orifice used for experimental measurements.

$$\dot{m}_{isentropic} = \dot{m}_g + \dot{m}_f \tag{30}$$

$$A_{orifice} = A_g + A_f \tag{31}$$

The isentropic mass flow rate for the given set of flow conditions (e.g., upstream stagnation pressure, upstream stagnation density, and downstream pressure) is defined as

the product of downstream mixture density, the sum of the vapor and liquid velocity fractions, and the nozzle (orifice) area, as represented by Equation (32).

$$\dot{m}_{isentropic} = \left(\frac{x_d}{\rho_{g,d}} + \frac{1 - x_d}{\rho_{f,d}}\right)^{-1} [x_d u_{g,d} + (1 - x_d) u_{f,d}] A_{orifice} \tag{32}$$

In order to solve this system of equations, one more piece of information is required. The slip ratio is defined as the ratio of the velocity of the vapor to the velocity of the liquid, as shown in Equation (33). Various analytical, numerical, and empirical correlations exist for the slip ratio.

$$S = \frac{u_{g,d}}{u_{f,d}} \rightarrow Correlation \tag{33}$$

With knowledge of the slip ratio, Equations (28), (29), (30), (31), (32), and (33) can be solved simultaneously. The resulting isentropic mass flow rate and the measured mass flow rate are substituted into Equation (8) in order to determine the discharge coefficient.

### 2.6.6 Slip Ratio

For single-component two-phase flow, the slip ratio is defined as the ratio of the velocity of the vapor to the velocity of the liquid. This ratio can also be written in terms of the vapor and liquid densities, the void fraction (volume fraction), and the quality, as shown in Equation (34).

$$S = \frac{u_g}{u_f} = \frac{\rho_f x (1 - \alpha)}{\rho_g (1 - x) \alpha} \tag{34}$$

Equation (34) shows that the slip ratio approaches unity as the ratio of the density of the liquid to the density of the vapor approaches unity. Therefore, the assumption of equal

velocities of the phases (one of the HEM assumptions) becomes less valid as the ratio of the densities increases.

An analytical solution for the slip ratio for critical flow of one-component two-phase mixtures in terms of the densities of the liquid and vapor phases can be determined by maximizing the mass flow rate in the governing equations of the separated flow model. The result is the expression shown in Equation (35). Moody [21] found good agreement between this model and available steam-water critical flow data.

$$S = \left(\frac{\rho_f}{\rho_g}\right)^{\frac{1}{3}} \tag{35}$$

Fauske [22, 23] developed a correlation for the slip ratio for critical flow of one-component two-phase mixtures based on experimental data with steam-water mixtures. His correlation is also based on the ratio of the densities of the liquid and vapor phases, but the exponent is different than Moody's solution, as shown in Equation (36).

$$S = \left(\frac{\rho_f}{\rho_g}\right)^{\frac{1}{2}} \tag{36}$$

The slip ratio expressions developed by Moody and Fauske for critical flows of single-component two-phase mixtures are the most well-known. However, many other correlations for both the slip ratio and the void fraction (the slip ratio can be determined if the void fraction is known) exist for various applications.

Since correlations for the slip ratio are often highly empirical, it is usually necessary to develop a correlation for the specific application of interest. If experimental data are

available, the slip ratio for which the separated flow model predicts the data can be determined and correlated in terms of the phase densities and other parameters.

## 2.7 Major Losses

### 2.7.1 Single-Phase Major Losses

For orifices with small L/D, forms losses are dominant, and an appropriate one-dimensional isentropic model with an empirical discharge coefficient provides an estimate of the mass flow rate through the orifice. However, for orifices with larger L/D, the major losses (i.e., friction, acceleration, and gravity) must be considered. The continuity, momentum, and energy equations for one-dimensional single-phase internal flow for the case in which major losses are not negligible are shown in Equations (37), (38), and (39), respectively [20]. The process is assumed to be adiabatic with no work entering or leaving the system.

$$\boldsymbol{Continuity}\text{: } \dot{m} = \rho u A = constant \tag{37}$$

$$\boldsymbol{Momentum}\text{: } \frac{dP}{dz} = -\underbrace{\frac{per}{A}\tau_w}_{friction} \underbrace{-\frac{\dot{m}}{A}\frac{du}{dz}}_{acceleration} - \underbrace{\rho g cos\theta}_{gravity} \tag{38}$$

$$\boldsymbol{Energy}\text{: } \underbrace{\frac{d\dot{q}}{dz}}_{0} - \underbrace{\frac{d\dot{W}}{dz}}_{0} = \dot{m}\frac{d}{dz}\left(h + \frac{u^2}{2} + gz\right) \tag{39}$$

The frictional pressure drop is expressed in terms of a dimensionless friction factor for which correlations exist. The two forms of the friction factor are the Fanning friction factor and the Darcy friction factor [20]. The Fanning friction factor is related to the wall shear stress by Equation (40), and the Darcy friction factor is four times greater than the

Fanning friction factor, as shown in Equation (41). For this study, the Darcy friction factor is used and is referred to as $f$.

$$f_{Fanning} = \frac{2\tau_w}{\rho u^2} \tag{40}$$

$$f_{Darcy} = 4f_{Fanning} = \frac{8\tau_w}{\rho u^2} \tag{41}$$

An expression for the single-phase frictional pressure drop in terms of the Darcy friction factor is developed by substituting Equation (41) into the friction term of Equation (38) for a circular channel of a specific length with constant fluid properties, as shown in Equation (42).

$$\Delta P_{friction} = -f\frac{L}{D}\frac{\rho u^2}{2} \tag{42}$$

A variety of friction factor correlations exist for laminar and turbulent flow. Due to the large Reynolds numbers associated with the flow of S-$CO_2$ through orifices, only correlations for turbulent flow are of interest. The implicit Colebrook equation [24] provides a general correlation for the Darcy friction factor for turbulent flow, and it includes the effects of the Reynolds number and the relative surface roughness, as shown in Equation (43).

$$\frac{1}{\sqrt{f}} = -2\log_{10}\left(\frac{\varepsilon}{3.7D} + \frac{2.51}{Re_D\sqrt{f}}\right) \tag{43}$$

Other correlations for single-phase turbulent flow exist, some of which include the effects of surface roughness and some of which do not, such as the Blasius solution [25], shown in Equation (44).

$$f = \frac{0.316}{(Re_D)^{0.25}} \tag{44}$$

Kruizenga et al. [4] found that both the Blasius and Colebrook correlations predicted experimental pressure drop data for the flow of S-$CO_2$ within heat exchangers accurately for pressure drops below 5 kPa. However, for pressure drops above 5 kPa, they observed an under prediction of the experimental pressure drop data when the Blasius correlation was used and an over prediction of the experimental pressure drop data when the Colebrook correlation was used.

Popov [26] developed a correlation for the friction factor for S-$CO_2$ based on his experimental data. The friction factor is in the form of a multiplier to a correlation for the isothermal friction factor developed by Filonenko [26], as shown in Equation (45).

$$f_{iso} = \frac{1}{(1.82 \log_{10} Re_b - 1.64)^2} \tag{45}$$

Popov's multiplier is shown in Equation (46), where $\rho_{b-w}^{ave}$ is the average density within a temperature range from $T_w$ to $T_b$.

$$\frac{f}{f_{iso}} = \left(\frac{\rho_{b-w}^{ave}}{\rho_b}\right)^{0.74} \tag{46}$$

An expression for the acceleration pressure drop for single-phase flow through a circular duct of specific length is developed by rearranging the acceleration term of Equation (38), as shown in Equation (47). This expression is a momentum balance, and it assumes that the acceleration pressure drop is only due to changes in the density of the fluid.

$$\Delta P_{acceleration} = -\left(\frac{\dot{m}}{A}\right)^2 \left(\frac{1}{\rho_{out}} - \frac{1}{\rho_{in}}\right) \tag{47}$$

Finally, an expression for the gravitational pressure drop for single-phase flow through a circular duct of specific length is shown in Equation (48), where $\theta$ is defined as the angle between the centerline of the duct and the direction of the gravitational force acting on the fluid.

$$\Delta P_{gravity} = L\rho g cos\theta \quad (48)$$

### 2.7.2 Long Orifice Modeling Methodology

The methodology used for modeling the flow of S-$CO_2$ through longer orifices for which the minor and major losses must be considered is illustrated in Figure 17. The form losses that occur at the entrance to the orifice are modeled by applying an empirical discharge coefficient to an appropriate isentropic model, using one of the methods described in previous sections. The form losses are represented by the section of the orifice that is labeled A in Figure 17. The models for the major losses are applied along the remaining length of the orifice, labeled as section B in Figure 17.

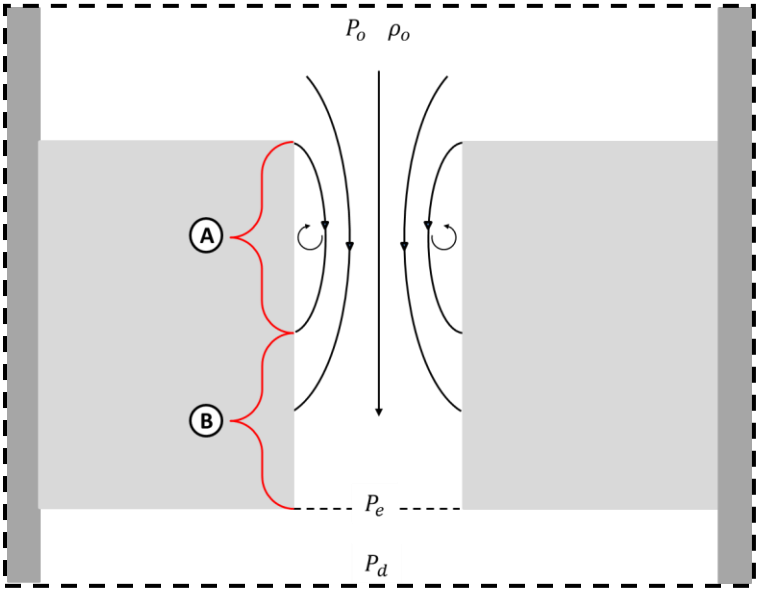


**Figure 17. Methodology for modeling the flow of S-$CO_2$ through orifices with large L/D.**
**A: Apply isentropic model with empirical discharge coefficient.**
**B: Apply models for major losses.**

Due to the property variations of $CO_2$ near the critical point, it is necessary to discretize the orifice into smaller length cells in which the properties do not vary significantly. The major losses are then integrated numerically along the length of the orifice. Figure 18 illustrates the discretization of an orifice into cells for numerical integration of the major losses.

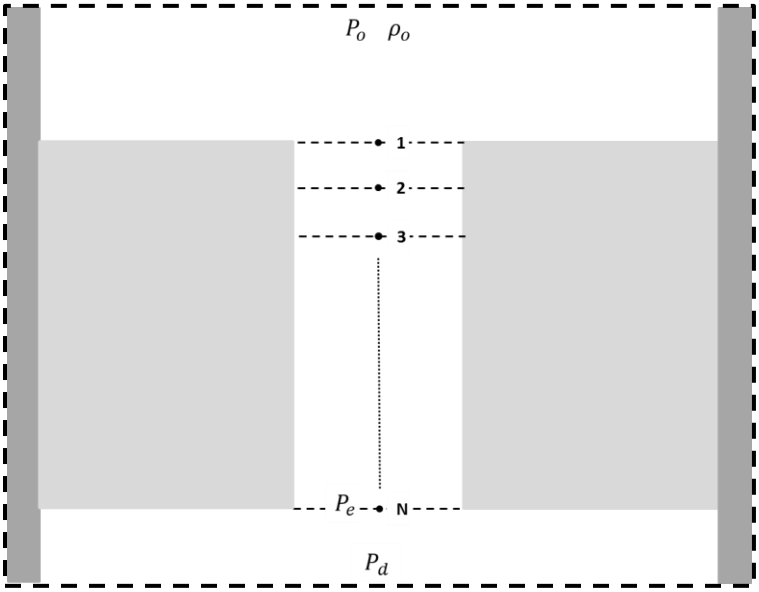


**Figure 18. Discretization of orifice with large L/D into smaller length sections.**

The length of each cell (the distance between each node) $dz$ is determined using Equation (49). It is important to note that the length over which the major losses are integrated does not include the length of the orifice used to determine the empirical discharge coefficient. The isentropic model with an empirical discharge coefficient accounts for all of the losses associated with the length of the orifice used for determining the discharge coefficient. Therefore, this length is subtracted from the total length of the longer orifice. The form loss is modeled as occurring between the upstream stagnation point and node 1.

$$dz = \frac{L}{N-1} \tag{49}$$

In the case of longer orifices, the measured downstream pressure is equal to the pressure of the last node of the numerical model. Therefore, both the mass flow rate through the orifice and the pressure at node 1 are unknown. The isentropic model with an empirical

discharge coefficient does not provide sufficient information to solve for the conditions at node 1 and initially, the mass flow rate through the orifice is guessed. The form loss at the orifice entrance is modeled by applying the measured upstream stagnation conditions, an empirical discharge coefficient, and the guess for the mass flow rate to an isentropic model in order to determine the properties and the velocity of the fluid at node 1, as shown in Equation (50).

$$P_1, s_1, h_1, \rho_1, \mu_1, u_1 = f(P_o, \rho_o, C_D, \dot{m}) \tag{50}$$

The mass flux of the fluid is a useful quantity for this analysis, and it is defined by Equation (51).

$$G = \frac{\dot{m}}{A_{orifice}} \tag{51}$$

The Reynolds number of the fluid within each cell is defined by Equation (52). The average of the viscosity of the fluid at the inlet and outlet of each cell is used.

$$Re_i = \frac{GD}{\frac{\mu_i + \mu_{i+1}}{2}} \quad for\ i = 1, N-1 \tag{52}$$

The Reynolds number of the fluid and the relative roughness of the duct surface are applied to a correlation in order to determine the Darcy friction factor within each cell, as shown in Equation (53).

$$f_i = f(Re_i, \varepsilon) \quad for\ i = 1, N-1 \tag{53}$$

The frictional pressure drop within each cell is calculated with Equation (54), in which the average of the density of the fluid at the inlet and outlet of each cell is used.

$$\Delta P_{friction_i} = f_i \frac{dz}{D} \frac{G^2}{2\left(\frac{\rho_i + \rho_{i+1}}{2}\right)} \quad for\ i = 1, N-1 \tag{54}$$

The acceleration pressure drop within each cell is calculated with Equation (55).

$$\Delta P_{acceleration_i} = G^2 \left(\frac{1}{\rho_{i+1}} - \frac{1}{\rho_i}\right) \quad for\ i = 1, N-1 \tag{55}$$

The gravitational pressure drop within each cell is shown in Equation (56), in which the average density of the fluid is used. In the experiment, the orifice is oriented in the direction of gravity (i.e., vertically).

$$\Delta P_{gravity_i} = \left(\frac{\rho_i + \rho_{i+1}}{2}\right) g dz \quad for\ i = 1, N-1 \tag{56}$$

The total pressure drop within each cell is defined as the sum of the friction, acceleration, and gravity pressure drops. This value is subtracted from the pressure at the entrance of each cell in order to obtain the pressure at the exit of each cell, as shown in Equation (57).

$$P_{i+1} = P_i - \Delta P_{friction_i} - \Delta P_{acceleration_i} - \Delta P_{gravity_i} \quad for\ i = 1, N-1 \tag{57}$$

The continuity equation is applied at the exit of each cell, as shown in Equation (58).

$$G = \rho_{i+1} u_{i+1} \quad for\ i = 1, N-1 \tag{58}$$

An energy balance is applied between the upstream stagnation point and the exit of each cell as shown in Equation (59).

$$h_{i+1} = h_o - \frac{u_{i+1}^2}{2} \quad for\ i = 1, N-1 \tag{59}$$

Finally, the density and the viscosity of the fluid at the outlet of each cell are related to the pressure and the specific enthalpy of the fluid at the outlet of each cell by property relations, as shown in Equation (60).

$$\rho_{i+1} = f(P_{i+1}, h_{i+1});\ \ \mu_{i+1} = f(P_{i+1}, h_{i+1}) \quad for\ i = 1, N-1 \tag{60}$$

Equations (52) through (60) provide ten equations and ten unknown variables for each cell, which allows for the properties and velocities at each node to be calculated. However, these values are based on the initial guess for the mass flow rate through the orifice. The final step is to iterate until the pressure of the last node is equal to the measured downstream pressure, as shown in Equation (61). This provides a calculation of the mass flow rate through an orifice of known length and diameter for a given upstream stagnation pressure, upstream density, and downstream pressure.

$$P_N = P_d \tag{61}$$

### 2.7.3 Two-Phase Major Losses

The HEM and the separated flow models can be used for modeling major losses when two-phase flow occurs within the orifice. Models for major losses with HEM assumptions are applied in the same way as single-phase models for major losses. However, mixture properties (in this case mass averaged) are used.

There are a number of approaches for determining the friction factor for two-phase flow based on the HEM assumptions. If the quality of the mixture is near 0 or 1, the fluid may be treated as either saturated liquid or saturated vapor, and the friction factor is determined with a single-phase correlation. A more common approach is to use mixture properties and a correlation for the mixture viscosity to determine the Reynolds number

of the mixture. The Reynolds number of the mixture is then used to determine the friction factor with a single-phase correlation. This is the approach used in this study. An extensive number of correlations for mixture viscosities have been developed, many of them empirical. McAdams et al. [27] proposed the expression for the mass averaged viscosity shown in Equation (62), which is used in this study.

$$\mu_m = \left( \frac{x}{\mu_g} + \frac{1-x}{\mu_f} \right)^{-1} \tag{62}$$

Models for the major losses with separated flow assumptions can also be derived. For example, the phases can be assumed to be in thermodynamic equilibrium with different velocities. However, these models were not utilized for this research, so they will not be discussed in detail.

## 2.8 Previous Work with Orifices

The flow of various fluids through orifices under ideal gas conditions has been studied extensively, and a variety of one-dimensional analytical models exist for predicting form losses [28-31]. In general, these one-dimensional analytical models are used to determine the contraction coefficient, which was previously discussed and is represented by Equation (7). The contraction coefficient can be applied to an isentropic flow model in order to determine the actual mass flow rate of fluid through the orifice.

The flow of a single-component, two-phase mixture through an orifice has also been studied extensively. For example, Fauske [22, 23, 32] and Moody [21] developed one-dimensional models for predicting the critical flow rate of single-component, two-phase mixtures through orifices with various length-to-diameter ratios (L/D) under various

orifice inlet conditions in the two-phase region based on analyzing steam-water mixtures. However, these models are highly empirical, and the accuracy of the models comes into question when they are applied to conditions other than the experimental conditions used for their derivation.

Relatively few studies have made attempts to measure the critical flow rates of supercritical fluids through orifices. For example, Mignot et al. [33, 34] measured the critical flow rates of S-$CO_2$ through orifices with L/D ranging from 3.7 to 168 for various inlet conditions that included up to three times the critical pressure and two times the critical temperature. However, the measurements were made under transient conditions. They found that when two-phase conditions existed for orifices with L/D greater than 14.7, the measured mass flow rates could be predicted accurately with the HEM model with friction using the Colebrook correlation for the friction factor. However, they did not attempt to develop a model for the form losses.

Liu et al. [35] made measurements that were similar to those made by Mignot et al. using a steady state experiment. Additionally, Chen et al. [36] measured the critical flow rate of water through short orifices under various inlet conditions in the supercritical region, and he attempted to correlate his data with a modified HEM, which is shown in the form of an expression for the mass flux in Equation (63), where $C$ is an empirically determined local resistance factor. The researchers found that the modified HEM predicted experimental mass flow rate measurements accurately for sharp edged orifices with a value of 0.6 for $C$, and for rounded edged orifices with a value of 0.2 for $C$.

$$G = \left[ \frac{2\left(h_o - x h_g - (1-x) h_f\right)}{\frac{C}{\rho_o^2} + \left(\frac{1-x}{\rho_f} + \frac{x}{\rho_g}\right)^2} \right]^{\frac{1}{2}} \tag{63}$$

Zwolinksi et al. [37] developed a scaling method for water and carbon dioxide at supercritical pressures, which may be useful for comparing models developed using supercritical water data with S-$CO_2$ data.

Limited data related to the flow of supercritical fluids through orifices for pressure ratios above the critical pressure ratio are available. However, it is necessary to have an understanding of the flow for these conditions when analyzing pipe bursts, valves, and turbomachinery seals. For example, power cycles such as the S-$CO_2$ Brayton cycle contain many valves across which the pressure drops are not large to enough to induce critical flow. The experiment described herein is capable of measuring flow rates of S-$CO_2$ through orifices for pressure ratios both above and below the critical pressure ratio.

# 3 Data Collection

## 3.1 Test Facility

Figure 19 shows a schematic of the test facility that was used to measure the flow rate of S-$CO_2$ through sharp-edged orifice geometries at different conditions. Various orifice geometries were tested under a range of inlet conditions in the supercritical region.

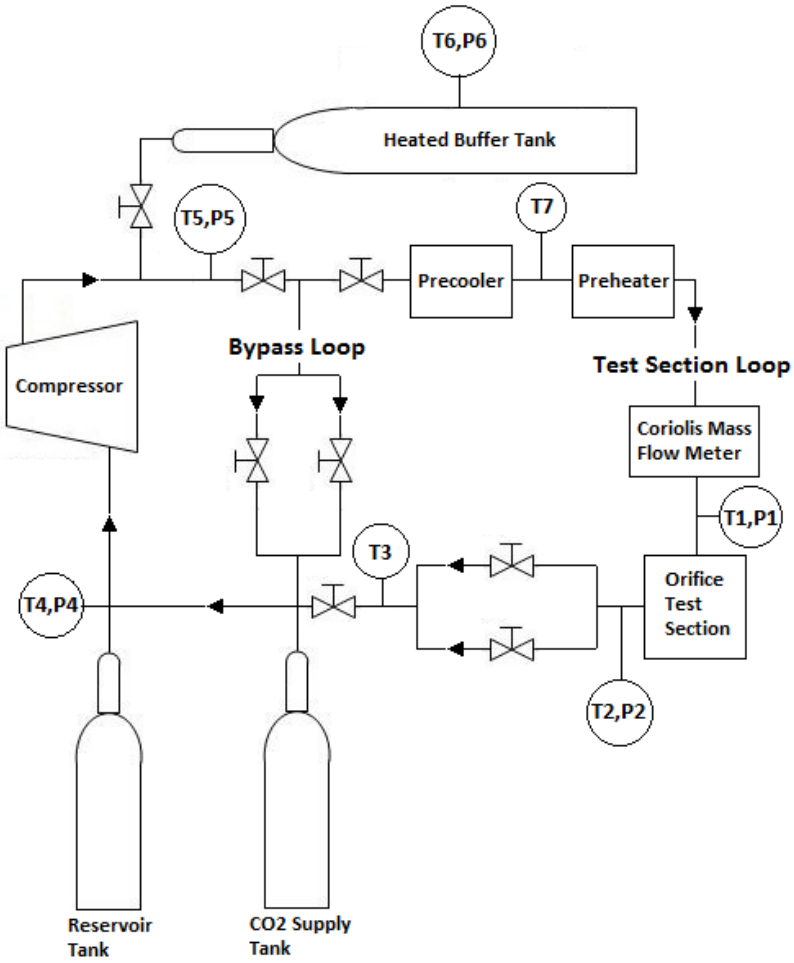


**Figure 19. Test facility.**

A single-stage, linear actuated compressor manufactured by Hydropac (Model No.: C02.4-40-2050LX/SSCO2) [38] is used to energize the facility, which consists of a

bypass loop and a test section loop. The Hydropac compressor has a maximum discharge pressure of 16.55 MPa (2400 psia) and a minimum suction pressure of 1.38 MPa (200 psia), which allow the facility to achieve a range of orifice inlet pressures that are both above and below the critical pressure. A photograph and a schematic of the Hydropac compressor are shown in Figure 20.

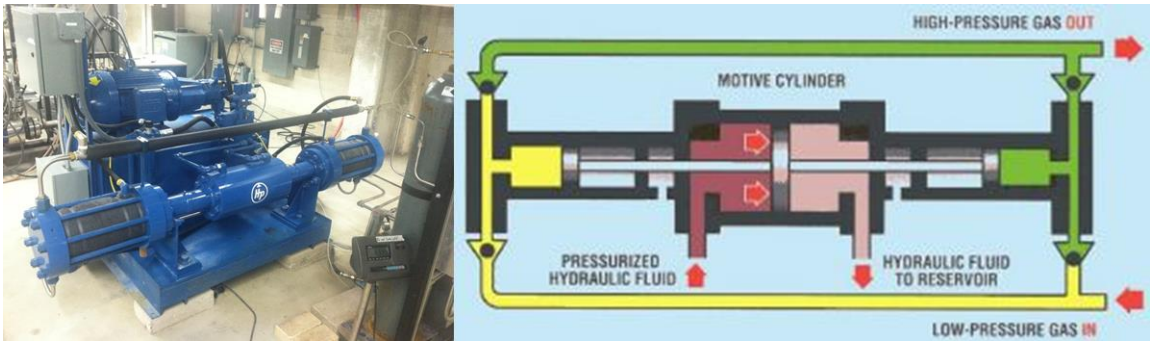


**Figure 20. Hydropac compressor used to energize test facility [38].**

The test section loop contains the test section with the orifice being investigated. Two valves (one fine and one coarse) located in the bypass loop are adjusted to control the amount of fluid allowed to bypass the test section loop. Pressure fluctuations at the test section inlet (due to the cycling of the compressor) are reduced to 20.7 kPa by a 0.123 $m^3$ heated buffer tank and a restriction valve located at the entrance to the test section loop. On the low pressure side of the loop, a reservoir tank is used to maintain a constant compressor inlet pressure, and two valves (one fine and one coarse) located at the outlet of the test section are used to control the test section outlet pressure. Simultaneous control of the valves in the bypass and test section loops allows independent control of the inlet and outlet pressures to the test section.

Fluid temperature is controlled at various locations within the experiment using a number of methods. The buffer tank requires heating in order to maintain a discharge pressure above the critical pressure because the saturation pressure of $CO_2$ at ambient temperature is 5.7 MPa. The buffer tank is wrapped with 4 HTS Amptek Duo-Tape® heater tapes [39], each capable of providing 1.25 kW. The temperature of the tank is controlled using these heaters with a Proportional Integral Derivative (PID) controller implemented in Labview™. Feedback for the PID controller is provided by three thermocouples welded to the surface of the buffer tank. During normal operation, the fluid in the buffer tank is maintained at a temperature that is between 70°C and 100°C in order to reduce the mass of $CO_2$ required in the system to reach high pressures (7.7 MPa-16.55MPa) in the supercritical region. The buffer tank before and after it was insulated is shown in Figure 21a and Figure 21b, respectively.

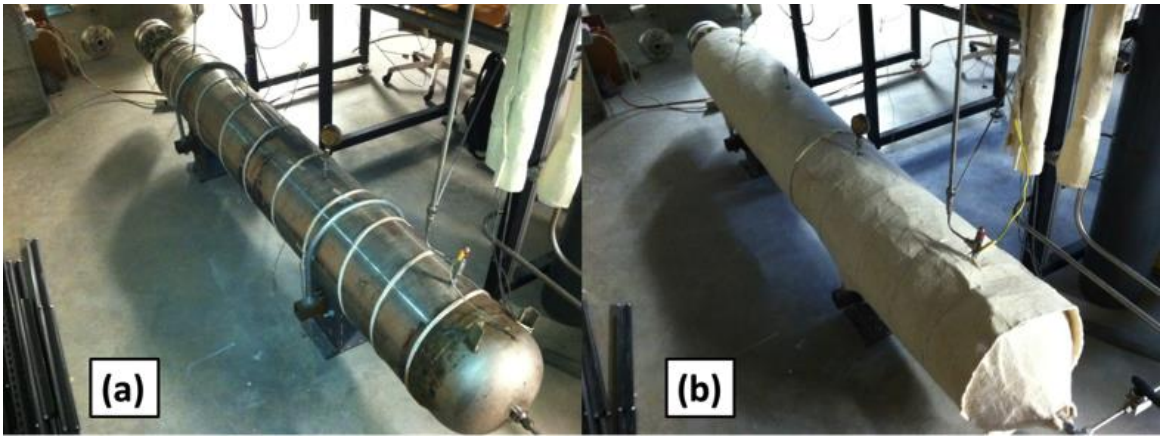


**Figure 21. Buffer tank (a) before and (b) after it was wrapped with insulation.**

To allow a test section inlet temperature that is lower than the buffer tank temperature, the fluid temperature is reduced using a precooler heat exchanger upon entering the test section loop. The precooler is a shell and tube heat exchanger with the $CO_2$ passing

through a helically wound pipe inside of a canister through which water flows. The duty of the precooler is controlled by varying the flow rate of water through the canister. The precooler heat exchanger is shown in Figure 22.


**Figure 22. Precooler heat exchanger.**

After exiting the precooler, the fluid is heated to the desired test section inlet temperature with a preheater consisting of three heated pipes in parallel. Each pipe is wrapped in HTS Amptek Duo-Tape® heater tape with a heating capacity of 1.25 kW. The inlet temperature of the test section is controlled with a PID controller implemented in Labview™. Temperature fluctuations observed at the test section inlet (based on a thermocouple immersed in the fluid) were smaller when feedback for the PID controller was provided by three thermocouples welded to the surfaces of the three heated pipes

than when it was provided by the thermocouple immersed in the fluid at the test section inlet. Therefore, this control scheme was used for all tests. During a typical run, the test section inlet temperature can be controlled to within 0.1°C.

**Figure 23. Preheater consisting of three heated pipes in parallel.**

The locations of temperature, pressure, density, and mass flow rate measurements are shown in Figure 19. The majority of these measurements are used for control feedback or to verify that the experiment is operating correctly. The test section inlet pressure, test section inlet density, test section mass flow rate, and test section outlet pressure are the primary measurements used to characterize the flow conditions and resulting flow rate through the orifices. Although the test section inlet temperature is measured with a thermocouple, the test section inlet pressure and test section inlet density are used to

define the test section inlet temperature for modeling purposes since these measurements have smaller uncertainties. Test section inlet and outlet stagnation pressures are measured with Siemens Sitrans P pressure transducers [40]. Both test section inlet pressure and test section outlet pressure correspond to stagnation pressures as they are measured in locations where the fluid velocity is negligible. The test section mass flow rate and inlet density are measured with an Endress Hauser Cubemass DCI Coriolis mass flow meter [41]. The uncertainties associated with these measurements are analyzed in the following sections.

Figure 24a illustrates a three-dimensional model of the test section, including the flow inlet and outlet ports. Figure 24b illustrates a three-dimensional model of the upper flange of the test section (upside down with respect to the model of Figure 24a), within which the orifices were secured during testing. Figure 24c illustrates a sectioned image of the upper flange and components used to secure the orifices. The orifices were placed inside of a drill bushing that is press fit into the upper flange. To secure the orifices within the press fit drill bushing, a relatively smaller drill bushing and a circular clamping plate was fastened to the upper flange with three socket head bolts. A pressure vessel attached to the lower flange was used to achieve steady downstream stagnation pressures.

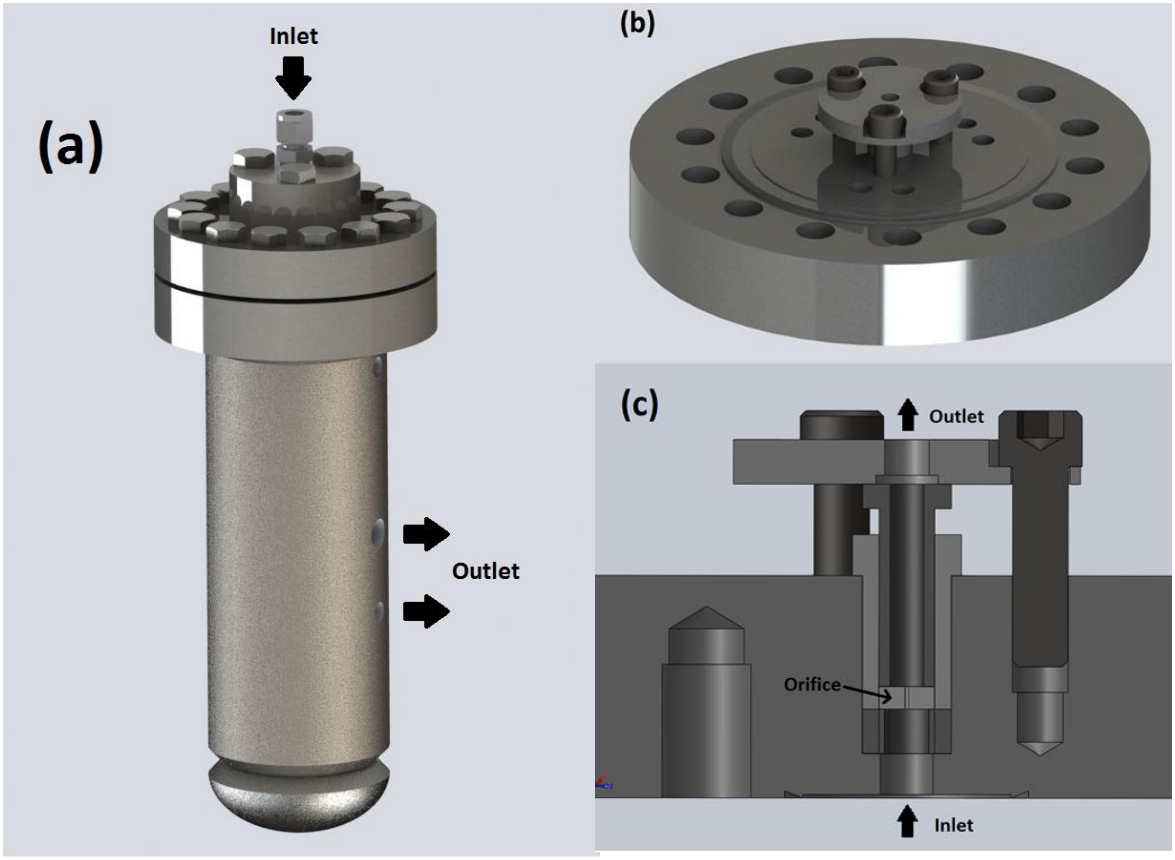


**Figure 24. Images of the (a) full test section, (b) upper flange of test section, and (c) section of upper flange in which orifices are secured. Orifices used for testing had diameters of 1 mm and lengths of 3.2 mm, 5 mm, and 20 mm. See Table 4 for precise measurements of the orifice dimensions.**

Figure 25a shows the schematic of the test facility, and Figure 25b shows the conditions at each point within the test facility for a typical experiment on a temperature-specific entropy diagram. The inlet conditions to the test section are held constant throughout a test at the desired orifice inlet condition in the supercritical region, represented by point 1 in Figure 25. There is a reduction in the pressure and temperature as the $CO_2$ flows through the orifice within the test section from the inlet (point 1) to the outlet (point 2) of the test section. The pressure at point 2 is controlled with the valves at the outlet of the test section. Another reduction in the pressure and temperature occurs from point 2 to

point 3 across the valves used to control the test section outlet pressure. Between point 3 and point 4, the $CO_2$ from the test section loop and the $CO_2$ from the bypass loop mix causing the $CO_2$ entering the compressor at point 4 to be in liquid phase under many conditions, as shown in Figure 25b. The compressor is designed to take in single-phase (either liquid or gas) or two-phase $CO_2$. From point 4 to point 5, the $CO_2$ is compressed and mixed with high temperature $CO_2$ from the buffer tank (point 6), which results in an increase in both the pressure and temperature of the $CO_2$. The pressure and temperature of the $CO_2$ is reduced as it passes through the restriction valve at the entrance to the test section loop, and the temperature is further reduced in the precooler, resulting in point 7 shown in Figure 25b. Finally, the temperature is increased to the desired test section inlet temperature (point 1) in the preheater. Figure 26 shows a photograph of the test facility with the components labeled.

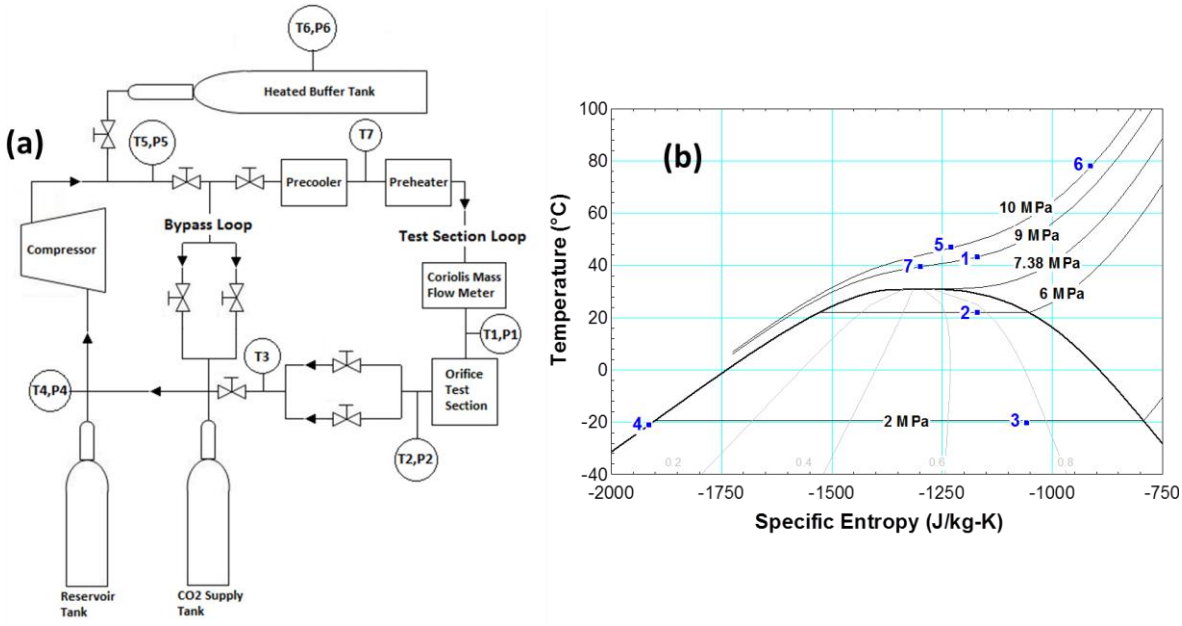


**Figure 25. (a) Schematic of the test facility and (b) conditions at each point within the test loop during a typical experiment on a temperature-specific entropy diagram.**

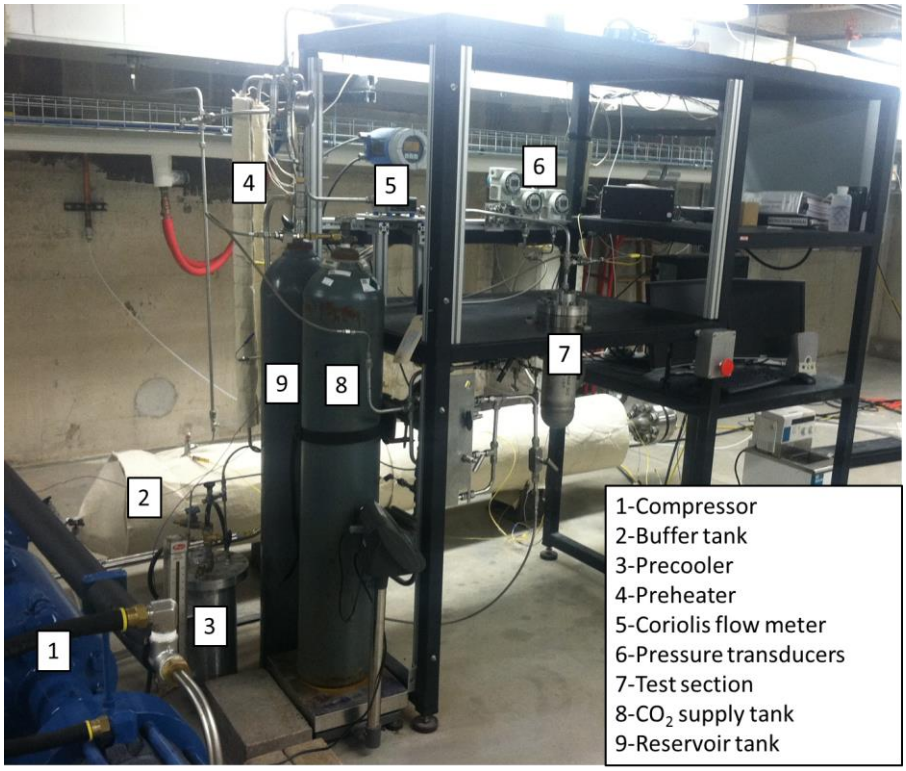


**Figure 26. Test facility with components labeled.**

## 3.2 Instrumentation and Measurement Uncertainties

Measurements of the test section mass flow rate, test section inlet density, test section inlet pressure, and test section outlet pressure were used to create and validate models for the flow of S-$CO_2$ through orifices based on experimental data. Therefore, it is important to quantify the uncertainties in these measurements. Two types of uncertainties (accuracy and precision) were considered.

### 3.2.1 Accuracy Uncertainties

Accuracy uncertainties are based on shifts in measurements from their true values; this type of uncertainty can be analyzed in the design stage, before physical measurements are available. Therefore, accuracy uncertainties are based on estimates for the uncertainties associated with the equipment used for collecting measurements. The accuracy uncertainties considered for this experiment are based on the instrument uncertainties reported by the manufacturers, the uncertainty associated with converting the instrument outputs from currents to voltages, and the uncertainty associated with the resolution of the data acquisition system.

Table 1 summarizes the instruments used for measuring the test section mass flow rate, test section inlet density, test section inlet pressure, and test section outlet pressure. Each instrument has a maximum measured instrument error reported by the manufacturer in various forms. The maximum measured error for the pressure transducers is provided as a percentage of the instrument reading that varies linearly between zero and the maximum span of the instrument. The maximum measured error for the Coriolis flow

meter for density measurements is 1 kg/m$^3$. Finally, the maximum measured error for the Coriolis flow meter for mass flow rate measurements is 0.1% of the instrument reading.

The resolution uncertainty is based on the resolution of the equipment used for data acquisition. The smallest voltage that the data acquisition system is capable of reading is based on the voltage input range and the number of bits of the system. The resolution uncertainty is defined by Equation (64). A National Instruments (NI) 9205 Data Acquisition (DAQ) system was used for data collection. The NI 9205 is a 16 bit system with an input voltage range of 20 V (+/- 10V).

$$unc_r = \underbrace{\frac{Range_{V_{da}}}{2^{N_{da}}}}_{\substack{smallest\ voltage \\ that\ system\ can \\ read}} * \frac{Maxspan_{ins}}{Range_{V_{ins}}} \tag{64}$$

**Table 1. Instruments used for measurements.**

| Measurement | Instrument | $MaxSpan_{ins}$ | Maximum measured error (from manufacturer) | Output Range |
|---|---|---|---|---|
| Inlet pressure | Siemens Sitrans P | 17.2 MPa (2500 psia) | $\leq 0.1\%$ Linear from 0 to $MaxSpan_{ins}$ | 4-20mA |
| Outlet pressure | Siemens Sitrans P | 0-17.2 MPa (2500 psia) | $\leq 0.1\%$ Linear from 0 to $MaxSpan_{ins}$ | 4-20mA |
| Inlet density | Endress Hauser Cubemass DCI | 1000 kg/m$^3$ | 1.0 kg/m$^3$ | 4-20mA |
| Mass flow rate | Endress Hauser Cubemass DCI | 0.10 kg/s | 0.1% of reading | 4-20mA |

All three of the instruments used for measurements have a current output range of 4-20mA. In order to convert the outputs to voltages for data acquisition, the current outputs of each instrument were passed through 250Ω resistors, and the voltage across the

resistors was measured with the data acquisition system. Therefore, the output range of each instrument was converted from 4-20mA to 1-5V. The resistances of the resistors were measured with a Hewlett-Packard 34401A Multimeter [42]. The uncertainty of the resistance measurements based on the error of the multimeter reported by Hewlett-Packard is the sum of 0.01 percent of the resistance reading and 0.004 percent of the span of the multimeter for the setting used (1kΩ). Table 2 shows the measured resistances and measurement uncertainties associated with the resistors that were used to convert instrument outputs from currents to voltages. The resulting voltage output ranges for each instrument are also shown.

**Table 2. Measured resistances and uncertainties associated with the resistors that were used to convert instrument outputs from currents to voltages and the resulting voltage output ranges.**

| Measurement | Instrument | Resistance of Resistor | Uncertainty in Resistance | $Range_{V_{ins}}$ |
|---|---|---|---|---|
| Inlet Pressure | Siemens Sitrans P | 249.55Ω | 0.065Ω | 0.9982V-4.991V |
| Outlet Pressure | Siemens Sitrans P | 249.08Ω | 0.065Ω | 0.9963V-4.981V |
| Inlet Density | Endress Hauser Cubemass DCI | 250.15Ω | 0.065Ω | 1.0006V-5.003V |
| Mass Flow Rate | Endress Hauser Cubemass DCI | 249.25Ω | 0.065Ω | 0.9970V-4.985V |

The uncertainties in the resistance measurements can be translated into uncertainties in pressure, mass flow rate, and density measurements. Calculations were performed for the maximum instrument outputs (20mA) where the uncertainties are the largest, as shown in Equation (65).

$$unc_{\Omega} = (0.065\Omega)(0.02A)\frac{MaxSpan_{ins}}{Range_{V_{ins}}} \tag{65}$$

The instrument uncertainties associated with the test section inlet pressure, test section outlet pressure, and the mass flow rate vary with the readings of the instruments. However, it is useful to look at the total accuracy uncertainty for each instrument for the worst case scenario in which the instrument reading is a maximum. The instrument, resistance, and resolution uncertainties are combined using the root sum-square (RSS) method to give the total accuracy uncertainty, as shown in Equation (66).

$$unc_{acc} = \sqrt{unc_{ins}^2 + unc_{\Omega}^2 + unc_r^2} \tag{66}$$

Table 3 shows the instrument, resistance, resolution, and total accuracy uncertainty for each measurement for this scenario. The results show that the accuracy uncertainty is almost entirely due to the instrument uncertainty for every measurement.

**Table 3. Instrument, resolution, and total design stage uncertainties for each measurement.**

| Measurement | $unc_{ins}$ | $unc_{\Omega}$ | $unc_r$ | $unc_{acc}$ |
|---|---|---|---|---|
| Inlet pressure | 17.24 kPa (2.50 psia) | 5.61 kPa (0.814 psia) | 1.30 kPa (0.19 psia) | 18.18 kPa (2.63 psia) |
| Outlet Pressure | 17.24 kPa (2.50 psia) | 5.62 kPa (0.816 psia) | 1.30 kPa (0.19 psia) | 18.18 kPa (2.63 psia) |
| Inlet density | 1.0 kg/m$^3$ | 0.325 kg/m$^3$ | 0.076 kg/m$^3$ | 1.05 kg/m$^3$ |
| Mass flow rate | 1.0e-4 kg/s | 3.3e-5 kg/s | 7.6e-6 kg/s | 1.06e-4 kg/s |

The previous analysis is useful for determining the maximum accuracy uncertainty during the design stage in order to choose the appropriate instruments. However, once an instrument is chosen and purchased, there are a number of methods for decreasing its

accuracy uncertainty. One such method involves calibrating the instrument using another instrument with a very small (preferably negligible) accuracy uncertainty. The pressure transducers used for measuring the upstream and downstream stagnation pressures were calibrated using a dead weight tester, which allows for a pressure, known to a high degree of accuracy, to be applied to the pressure transducers. The pressure is applied by stacking plates on top of a spindle that is suspended in incompressible oil; the oil column transmits the pressure to the pressure transducer, as shown in Figure 27a. The measured masses of the cylindrical plates and the diameter of the spindle upon which they stacked are provided by the manufacturer of the dead weight tester. Therefore, the pressure applied to the pressure transducers when they are installed in the dead weight tester can be calculated to a high degree of accuracy.

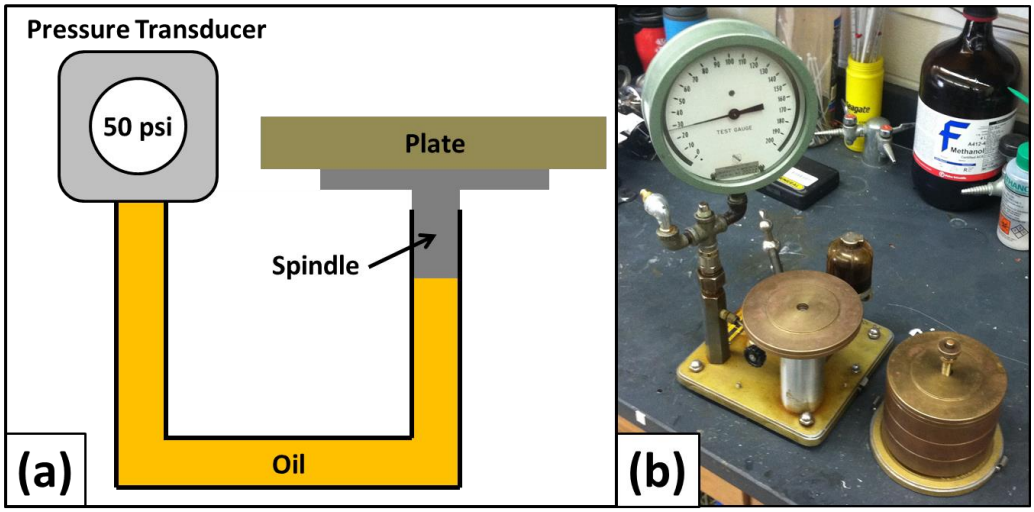


**Figure 27. Dead weight tester used for calibrating pressure transducers.**

Pressures ranging from 60 psia to 1861 psia were applied to the pressure transducers with the dead weight tester. For each applied pressure, the pressures measured by the pressure

transducers were recorded as an average of 1000 samples collected at a rate of 1000 Hz. Figure 28 shows the calibration curve for the upstream pressure transducer and the data used to construct the calibration curve. The actual pressure is defined as the pressure applied by the dead weight tester and the measured pressure is defined as the pressure measured by the upstream pressure transducer. A line was fit to the data points using EES [13], which provides the actual pressure as a function of the pressure measured by the upstream pressure transducer over the entire calibration range.

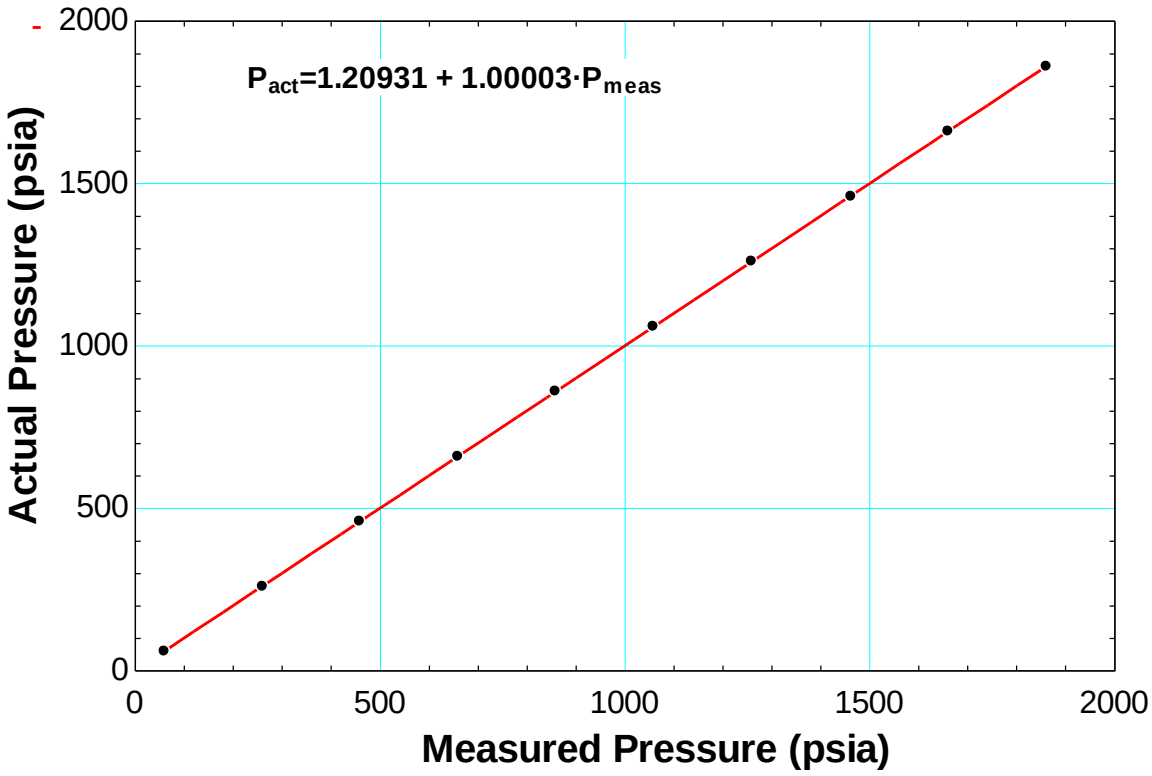


**Figure 28. Calibration curve for upstream pressure transducer.**

The accuracy uncertainty that remains after the calibration process is based on the deviation of the measured data points from the calibration curve. The standard deviation

based on this definition is shown in Equation (67), where $P_{actual,i}$ is the pressure calculated with the calibration curve for a given measured pressure, $P_{measured,i}$.

$$s_{acc_{cal}} = \frac{\sqrt{\sum_{i=1}^{N}\left(P_{actual,i} - P_{measured,i}\right)^2}}{\sqrt{N}} \tag{67}$$

Assuming that the errors are normally distributed, the uncertainty for a finite sample size is defined based on a given confidence interval as the product of the standard deviation of the sample and the appropriate value (based on the degrees of freedom) from the Student's t-distribution, as shown in Equation (68) for a 95% confidence interval.

$$unc_{acc_{cal}} = s_{acc} t_{v_{95}} \tag{68}$$

The uncertainty associated with the accuracy of a pressure measurement based on calibration is 2.28 psia for the upstream pressure transducer and 3.59 psia for the downstream pressure transducer. It is interesting to note that the uncertainty associated with the downstream pressure transducer based on calibration is greater than the maximum error specified by the manufacturer. This could be due to drift of the transducer over time. The uncertainty associated with the accuracy of a pressure measurement based on calibration is combined with the uncertainty associated with the precision of the pressure measurement in order to determine the overall uncertainty, as discussed in the following section.

It is not standard practice for users to calibrate Coriolis flow meters prior to using them for measurements. Therefore, the accuracy uncertainty of mass flow rate and density measurements are based on the instrument, resistance, and resolution uncertainties.

### 3.2.2 Precision Uncertainties

Precision uncertainties are based on the statistics of a sample of measurements, and can therefore be determined only after measurements are available. In this study, steady state for the experiment was defined as a period of 60 seconds during which the downstream pressure fluctuated by no more than 20.7 kPa (3 psi) and the upstream temperature, based on the thermocouple immersed in the fluid at the test section, fluctuated by no more than 0.1°C. Although the experiment had reached steady state at this point in time, fluctuations associated with the operation of the experiment and changes in the ambient environment remained. Therefore, once steady state was reached, data points were collected for 30 seconds in order to analyze these remaining fluctuations. During the 30 seconds of data collection, measurements of the test section mass flow rate, test section inlet density, test section inlet pressure, and test section outlet pressure were sampled by the NI DAQ at a rate of 1000 Hz. One data point was recorded each second, and the value of the recorded data point was the average of the 1000 measurements sampled within that second. Therefore, for one steady state condition, 30 data points were recorded for the test section mass flow rate, test section inlet density, test section inlet pressure, and test section outlet pressure. Although there were statistical uncertainties associated with the scatter of the 1000 points that were averaged each second, these uncertainties were much smaller than the statistical uncertainties associated with the

steady state fluctuations of the experiment. Therefore, the precision uncertainty was defined as the statistical uncertainty observed in the 30 data points collected over 30 seconds of steady state operation. The statistical uncertainty associated with a finite sized sample is dependent on the standard deviation of the sample, which is defined by Equation (69) for a sample of pressure measurements, where $\bar{P}$ is the average of the sample. The same method applies to mass flow rate and density measurements.

$$s_{prec} = \frac{\sqrt{\sum_{i=1}^{N}(\bar{P} - P_i)^2}}{\sqrt{N}} \tag{69}$$

Assuming that the errors of the sample are normally distributed, the uncertainty associated with the precision of a measurement is defined for a given confidence interval as the product of the standard deviation of the sample and the appropriate value (based on the degrees of freedom) from Student's t-distribution, as shown in Equation (70) for a 95% confidence interval.

$$unc_{prec} = s_{prec} t_{\upsilon_{95}} \tag{70}$$

### 3.2.3 Combining Precision and Accuracy Uncertainties

There are a variety of methods for combining the precision and accuracy uncertainties in order to determine the overall uncertainty of a measurement. For the test section inlet and outlet pressure measurements, an overall uncertainty is defined by combining the accuracy uncertainty (based on calibration) and the precision uncertainty (based on steady state fluctuations) using the RSS method, as shown in Equation (71). In order to

combine the two uncertainties, it is necessary that they are calculated for the same confidence interval, in this case 95%.

$$unc_{overall,P} = \sqrt{unc_{acc,cal}^2 + unc_{prec}^2} \tag{71}$$

Combining the precision and accuracy uncertainties for the measurements of the mass flow rate and the density is accomplished using a slightly different technique because the Coriolis flow meter was not calibrated. The range of mass flow rates measured with the experiment varied from approximately 0.01 kg/s to 0.04 kg/s. The accuracy uncertainties based on the instrument, resistance, and resolution uncertainties associated with these flow rates are $1.3 \times 10^{-5}$ kg/s and $4.1 \times 10^{-5}$ kg/s, respectively. The precision uncertainties associated with mass flow rate measurements for all tests conducted varied from approximately $1.0 \times 10^{-4}$ kg/s to $4.0 \times 10^{-4}$ kg/s, depending on the test conditions. Therefore, the accuracy uncertainty associated with mass flow rate measurements was neglected since it was an order of magnitude less than the precision uncertainties observed. The overall uncertainty associated with mass flow rate measurements was assumed to be completely due to precision uncertainties from steady state fluctuations within the experiment.

The accuracy uncertainty associated with density measurements is on the same order of magnitude as the precision uncertainties that were observed during testing. Therefore, it is necessary to consider both uncertainties in the overall uncertainty. Although the accuracy uncertainty for density measurements based on the instrument, resistance, and resolution uncertainties is not necessarily associated with a 95% confidence interval, it

was still combined with the precision uncertainty using the RSS method in order to estimate an overall uncertainty associated with density measurements, as shown in Equation (72).

$$unc_{overall,\rho} = \sqrt{unc_{acc}^2 + unc_{prec}^2} \tag{72}$$

### 3.3 Orifice Geometries

Orifices with diameters of 1 mm were used for all experiments reported in this paper. Two orifices with small L/D were tested in order to gain an understanding of form losses, and one orifice with a large L/D was tested in order to gain an understanding of major losses. Accurate measurements of the diameters, lengths, inlet and outlet curvatures, and roughness were necessary in order to connect the data to a specific physical geometry. Precise knowledge of the geometry is essential for the creation and validation of one-dimensional and multi-dimensional models.

Images of each orifice were captured using a microscope with a resolution of 0.90 microns. The ImageJ software package developed by the National Institutes of Health [43] was used to manually fit circles to the images in order to determine the diameters of the orifices. Images were captured with the light source directed from beneath the orifice and at the top of the orifice as shown in Figure 29a and Figure 29b, respectively. Positioning the light source beneath the orifices resulted in better lighting near the edges of the orifice, so this method was used for diameter measurements. The length of each orifice was measured with a micrometer with a resolution of 1.3 microns. Table 4

summarizes the measurements of the lengths and diameters of the three orifices used for testing.

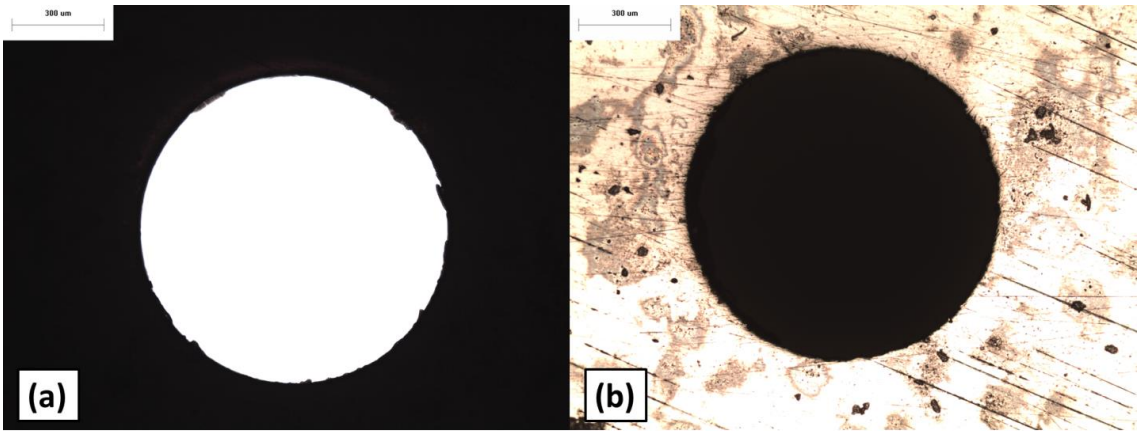


**Figure 29. Images of Orifice B taken with a microscope with (a) bottom lighting and (b) top lighting.**

**Table 4. Measurements of diameters and lengths of the orifices used for testing.**

| Orifice Label | Diameter (mm) | Length (mm) | Length to Diameter Ratio (L/D) |
|---|---|---|---|
| A | 1.014 | 3.233 | 3.188 |
| B | 1.006 | 5.011 | 4.981 |
| C | 1.009 | 20.015 | 19.847 |

In order to accurately represent the geometries of the orifices, especially as required for a detailed computational fluid dynamics (CFD) model, the sharpness of the inlet and outlet edges of Orifice B and Orifice C were measured. To quantify sharpness, a Zygo NewView$^{TM}$ white light interferometric microscope [44] was used. The curvatures of the inlet and outlet edges of Orifice A could not be measured with the interferometric microscope due to uncertainties caused by light scatter from the rough surface (this was not discovered until after flow data were collected using Orifice A). The inlet and outlet edges of Orifice B and Orifice C were therefore polished prior to data collection,

allowing the interferometric microscope to measure the curvatures of the inlet and outlet edges after testing. Figure 30 shows three-dimensional models of the surface of Orifice B captured by the white light interferometric microscope for two different magnification settings.


**Figure 30. Three dimensional models of the surface of Orifice B from the Zygo NewView™ white light interferometric microscope for two different magnification settings.**

Figure 31a illustrates a diagram of an orifice with the inlet edge of the orifice circled, highlighting one portion of Orifice B for which sharpness was quantified. Data points representing the curvature of the inlet edge of Orifice B (highlighted in Figure 31a) at a single circumferential location are shown in Figure 31b (note that the axes are scaled differently). The figure shows that the inlet edge of Orifice B is very sharp. Mass flow rate and discharge coefficient results for Orifices A and B were very close for the inlet conditions tested. Therefore, although the curvatures of the inlet and outlet edges of Orifice A were not measured, the geometry of Orifice A is thought to be similar to that of Orifice B. Curvature data for two circumferential locations for both the inlet and outlet edges of Orifice B and Orifice C are provided with the experimental data as an electronic supplement to this document.

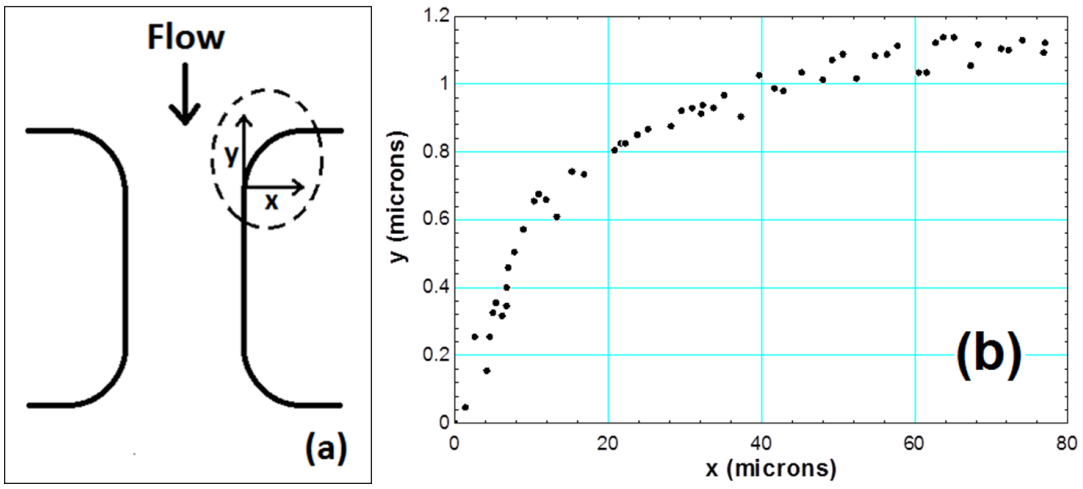


**Figure 31. Diagram of (a) region of interest for curvature measurements and (b) measured data for the curvature of the inlet edge of Orifice B at a single circumferential location.**

The surface roughness of Orifice C was also measured since it is required to accurately predict the frictional pressure losses in CFD simulations and one-dimensional models utilizing correlations for the friction factor which account for the surface roughness. The Zygo NewView$^{TM}$ white light interferometric microscope [44] was used to make this measurement. After data was collected, Orifice C was modified in order to provide optical access to the channel surface, as shown in Figure 32. The measured surface roughness was 3.005 microns.

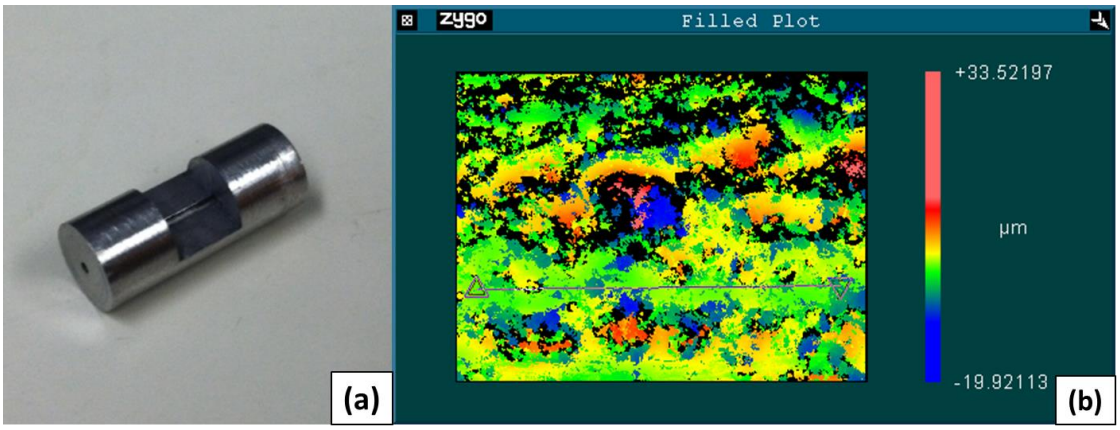


**Figure 32. (a) Orifice C after modifications were made for surface roughness measurements and (b) a contour plot of the surface of the channel of Orifice C obtained from the white light interferometric microscope.**

## 3.4 Test Conditions

The objective of this study is to collect data over a wide range of test section inlet conditions that span the supercritical region. Figure 33 shows the density of $CO_2$ as a function of temperature for various pressures in the supercritical region. The square points represent the test section inlet conditions at which data were collected for each orifice. Figure 34 shows the test section inlet conditions plotted on a temperature-specific entropy diagram. The pseudo-critical line is also shown in both figures. Data collected at these orifice inlet conditions provide insight into single-phase and two-phase flow of $CO_2$ over a wide range of densities, pressures, and temperatures near the critical point and the pseudo-critical line.

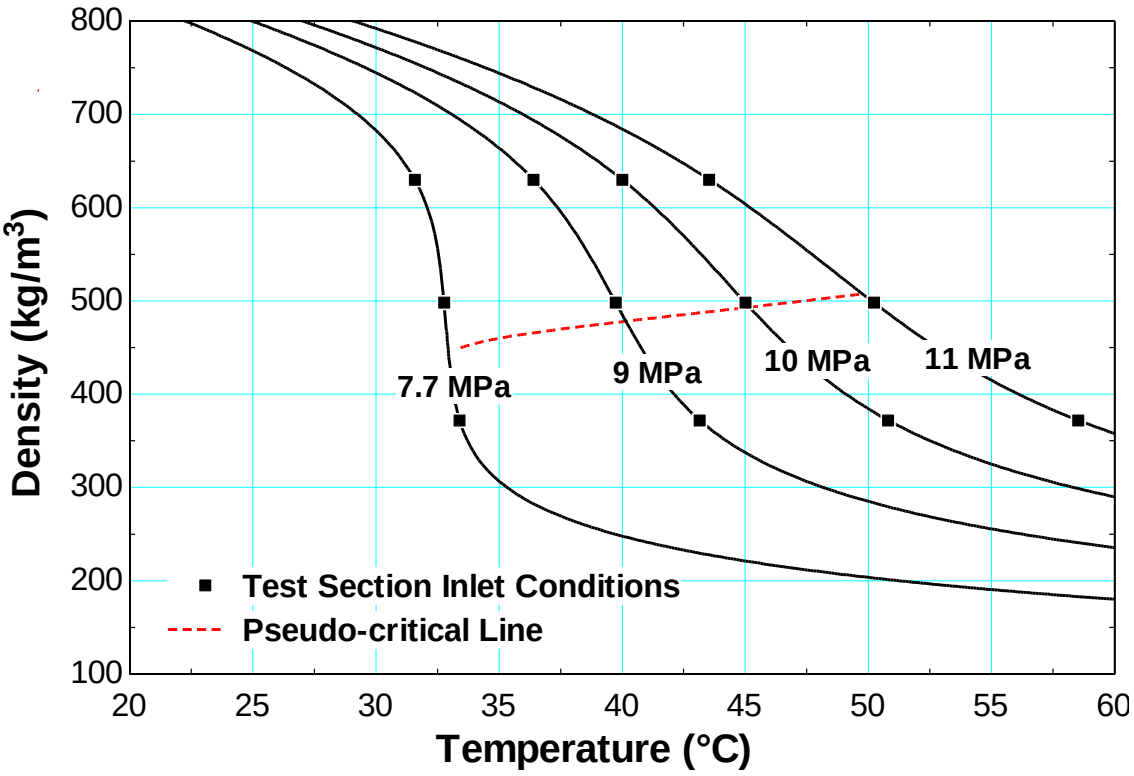


**Figure 33. Density of $CO_2$ as a function of temperature for various values of pressure. The test section inlet conditions at which data were collected are shown as square points.**

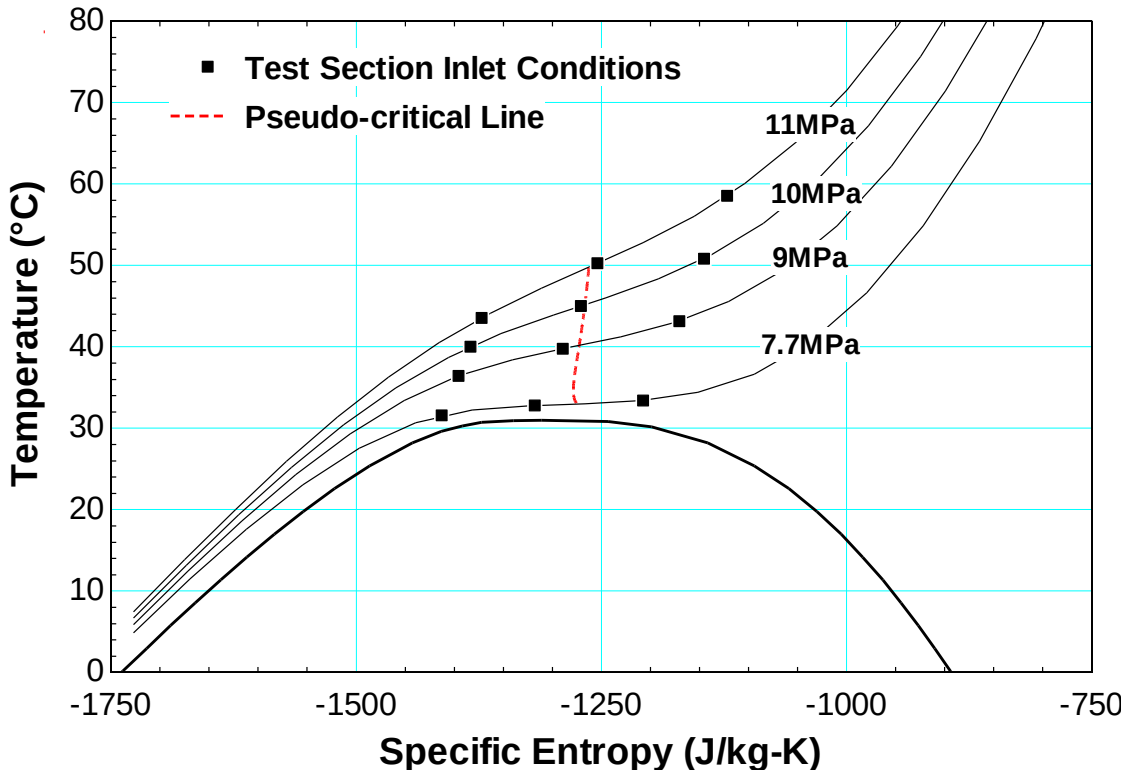


**Figure 34. Temperature-specific entropy plot for $CO_2$ with the test section inlet conditions shown as squares.**

### 3.5 Data Collection Procedure

Figure 35 shows the measured mass flow rate for a typical data set collected for the flow of S-$CO_2$ through a specific orifice at a given inlet condition. In Figure 35, the measured mass flow rate is shown as a function of the pressure ratio; pressure ratio is defined as the ratio of the test section outlet pressure to the test section inlet pressure. For each data set, the test section inlet condition was held constant and data were collected as the test section outlet pressure was incrementally increased from an initial value that corresponded to a pressure ratio of approximately 0.3. At each outlet pressure, the experiment was allowed to reach steady state and data were collected for 30 seconds. Steady state was defined as a period of 60 seconds during which the downstream

pressure fluctuated by no more than 20.7 kPa (3 psi) and the upstream temperature, based on the thermocouple immersed in the fluid at the test section inlet, fluctuated by no more than 0.1°C. In Figure 35, each data point represents the average measured mass flow rate for data collected over the 30 seconds at a rate of 1000 Hz while the experiment was at steady state. Note in Figure 35 that more data are collected in the region where the flow becomes critical in order to capture the critical pressure ratio and critical mass flow rate accurately. The method used for determining this critical point will be discussed in the following section.

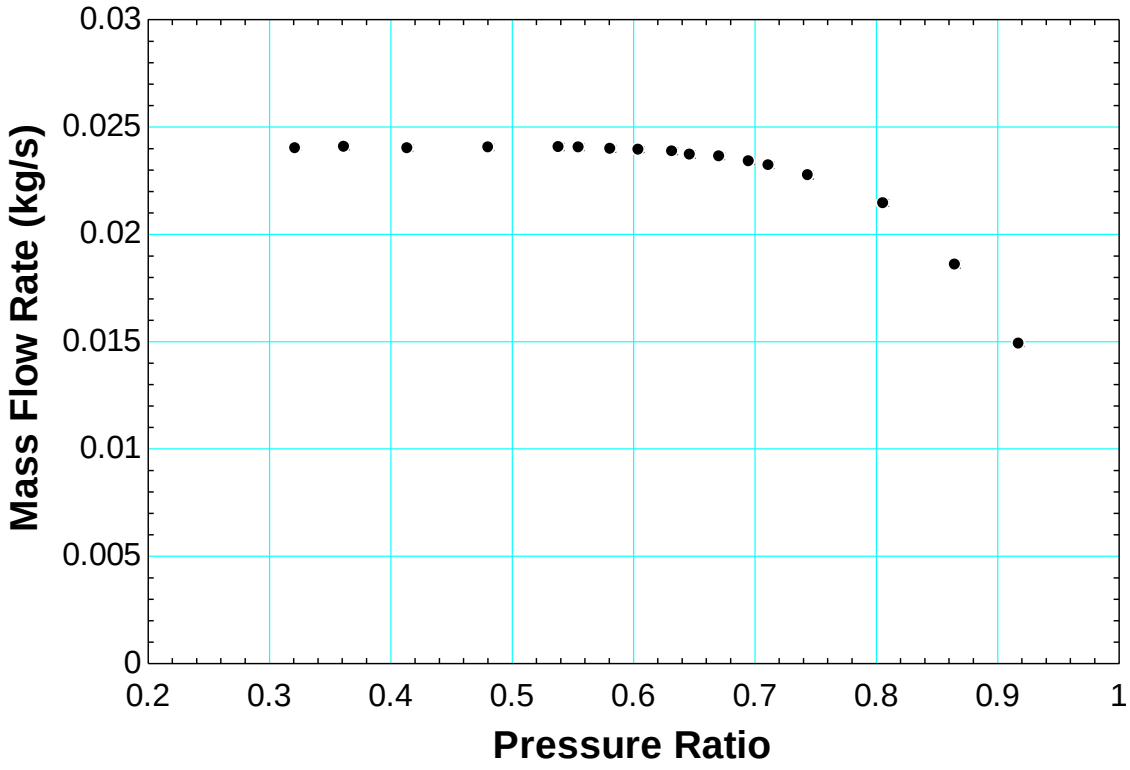


**Figure 35. Measured mass flow rate of $CO_2$ through Orifice B as a function of pressure ratio for an upstream stagnation pressure of 9 MPa and an upstream stagnation density of 372 kg/m$^3$.**

# 4 Results

## 4.1 Critical Pressure Ratio and Critical Mass Flow Rate

As described in previous sections, analysis of pipe bursts, valves, and turbomachinery seals require an understanding of the critical pressure ratio and the critical mass flow rate for a given orifice geometry and set of inlet conditions. Therefore, a method for precisely determining the critical pressure ratio and the critical mass flow rate was developed and applied to each set of data. Initially, a sixth order polynomial curve is generated to represent the measured mass flow rate as a function of the measured pressure ratio as shown in Figure 36. The critical pressure ratio is defined as the point at which the mass flow rate no longer changes with pressure ratio; therefore, for analysis of the experimental data, the critical pressure ratio is estimated as the point at which the derivative of the polynomial curve fit with respect to the pressure ratio first reaches zero. The tolerance associated with the point at which the curve fit is said to have reached zero is based on the fluctuations and offset from true zero of the curve fit observed at low pressure ratios when the flow is known to be critical. Figure 37 shows the derivative of the polynomial curve fit of Figure 36 (the sign is flipped in order to provide a better illustration of the concept) with respect to the pressure ratio as a function of the pressure ratio. An accurate estimate of the pressure ratio at the onset of critical flow was determined using this data analysis technique. Finally, the critical mass flow rate was calculated for each data set by substituting the value for the corresponding critical pressure ratio into the polynomial curve fit. Three tests were performed with Orifice A for orifice inlet conditions in the ideal gas region in order to verify that the

instrumentation for the experiment was functioning properly. The critical pressure ratio for an ideal gas with the properties of $CO_2$ flowing through an orifice is between 0.56 and 0.57. The value of the critical pressure ratio for all three of the tests performed in the ideal gas region was 0.5604 (determined using the method that was just discussed).

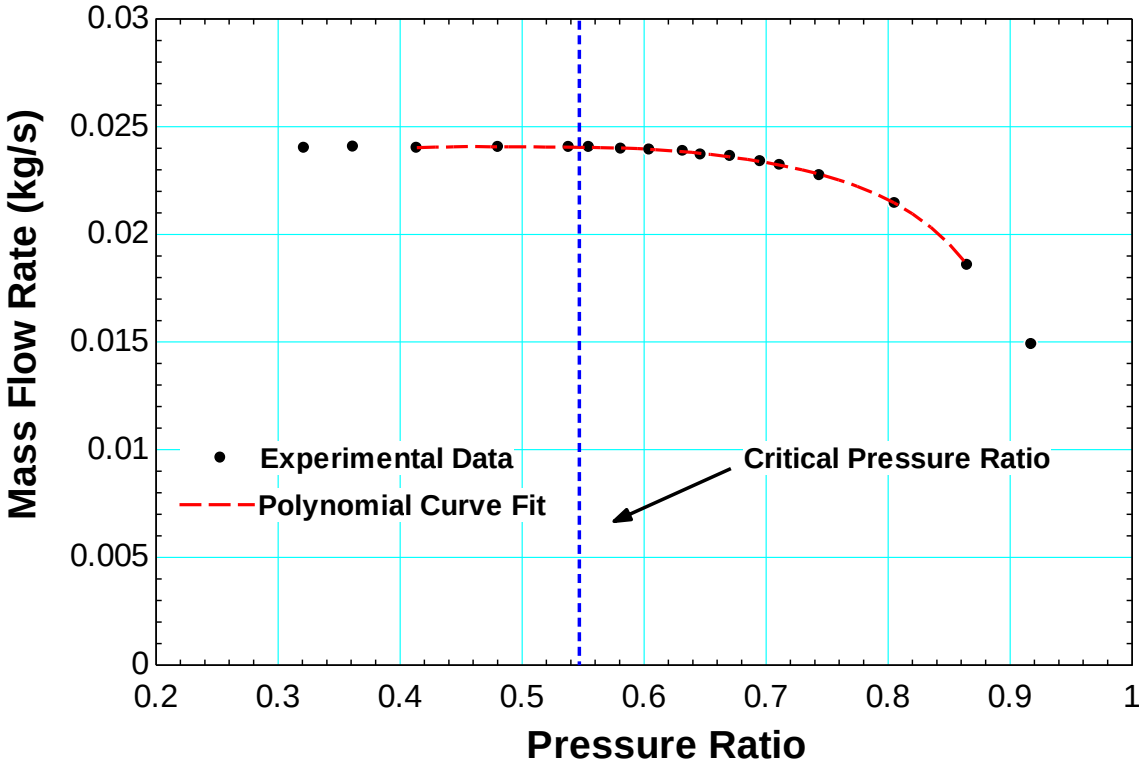


**Figure 36. Measured mass flow rate of $CO_2$ through Orifice B as a function of pressure ratio with a polynomial curve fit to the data for an upstream stagnation pressure of 9 MPa and an downstream stagnation density of 372 kg/m$^3$.**

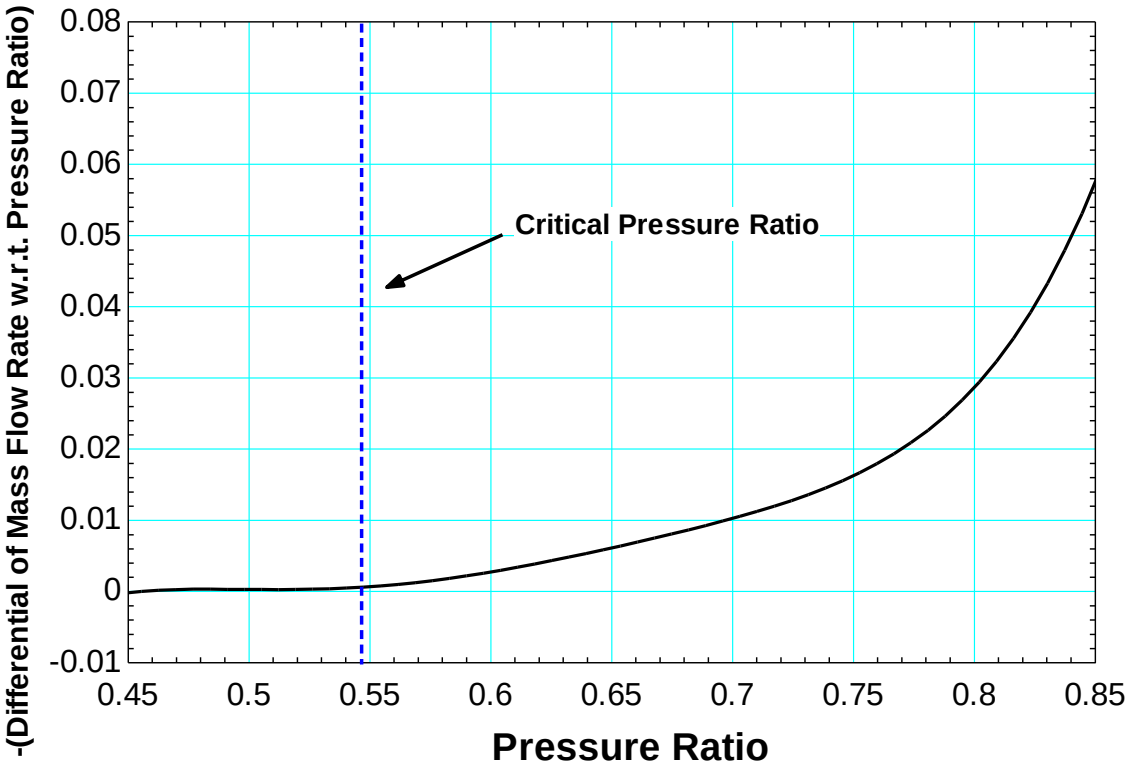


**Figure 37. Derivative of the polynomial curve fit shown in Figure 36 with respect to pressure ratio as a function of pressure ratio for the flow of $CO_2$ through Orifice B with an upstream stagnation pressure of 9 MPa and an upstream stagnation density of 372 kg/m$^3$.**

## 4.2 Repeatability Experiments

During the early stages of testing, it was observed that the data being collected were not repeatable. The cause of the issue was determined to be inconsistent leakage around the outer edges of the orifice through the metal-to-metal interfaces between the orifice and the drill bushings on either side of it. A variety of sealing methods were tested, including soft and hard Buna-N O-rings and high temperature RTV sealant. The sealing interfaces are shown in Figure 38.

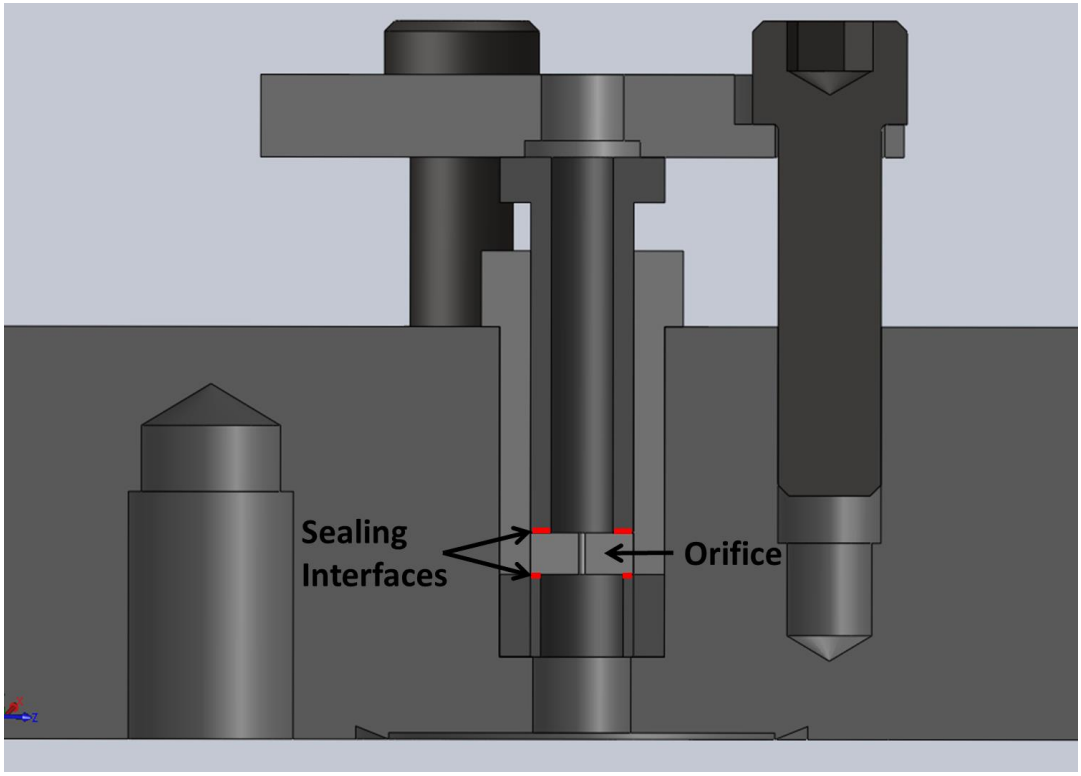


**Figure 38. Schematic of the orifice clamping assembly with the sealing interfaces labeled.**

Repeatability tests were performed with Orifice A for an upstream stagnation pressure of 10 MPa and an upstream stagnation density of 372 kg/m$^3$. Figure 39a shows the measured mass flow rate as a function of pressure ratio for the various sealing methods. The repeatability of the data is more visible in Figure 39b, which shows the discharge coefficient as a function of pressure ratio for the various sealing methods. The discharge coefficient is defined as the ratio of the measured mass flow rate to the isentropic mass flow rate, calculated with the single-phase isentropic model for single-phase outlet conditions and with the isentropic HEM for two-phase outlet conditions. The results show that all three sealing methods are sufficient to provide repeatable data. The high temperature RTV sealant was chosen for its ease of application and resistance to high temperature degradation for extended periods of time.

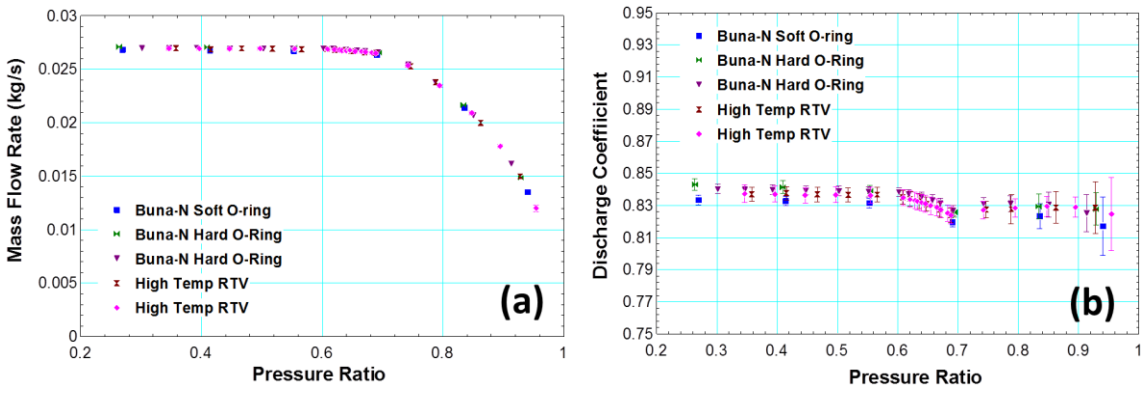


**Figure 39. Measured mass flow rate as a function of pressure ratio for various sealing techniques (a) and the resulting discharge coefficient as a function of pressure ratio (b). All tests were performed with Orifice A for an upstream stagnation pressure of 10 MPa and an upstream stagnation density of 372 kg/m$^3$.**

## 4.3 Form Loss Results

Data were collected with Orifice A and Orifice B for 12 inlet conditions in order to develop and validate models for form losses. For simplicity, the data sets that were collected with the 12 inlet conditions will be referred to by the single letter labels shown in Table 5. The geometries of Orifice A and Orifice B are summarized in Table 4.

**Table 5. Labels for inlet conditions, defined by stagnation pressure and stagnation density, for which data were collected.**

| Label | Upstream Stagnation Pressure (MPa) | Upstream Stagnation Density ($kg/m^3$) |
|---|---|---|
| A | 7.7 | 372 |
| B | 7.7 | 498 |
| C | 7.7 | 630 |
| D | 9 | 372 |
| E | 9 | 498 |
| F | 9 | 630 |
| G | 10 | 372 |
| H | 10 | 498 |
| I | 10 | 630 |
| J | 11 | 372 |
| K | 11 | 498 |
| L | 11 | 630 |

The data collected with Orifice A and Orifice B were very similar. This was expected, since form losses are dominant for orifices with small L/D. Therefore, the figures used for explanations of form loss results are primarily based on data collected with Orifice B. However, ultimately, the models that were developed and validated for form losses were based on data from Orifice A and Orifice B.

Figure 40 shows the inlet conditions and approximate orifice outlet conditions for data sets A, B, and C collected with Orifice B on a temperature-specific entropy diagram. The inlet conditions (squares) are defined by the measured upstream stagnation pressure and the measured upstream stagnation density. The approximate orifice outlet conditions (circles) are defined by the measured downstream stagnation pressure and the upstream specific entropy. Therefore, the outlet conditions shown in the figure are approximate, since the isentropic assumption was applied. The approximate orifice outlet conditions for each test represent the downstream conditions at which data were collected for

subcritical flow. For pressure ratios lower than the critical pressure ratio (determined using the method discussed in the previous section), the orifice outlet conditions are constant and independent of the measured downstream stagnation pressure. Although data were collected for downstream stagnation pressures corresponding to pressure ratios below the critical pressure ratio, these conditions are not shown on the temperature-specific entropy diagram since they do not describe the conditions at the orifice outlet. Therefore, the outlet condition with the lowest pressure and temperature for each data set in Figure 40 approximately corresponds to the critical pressure ratio for the respective data set.

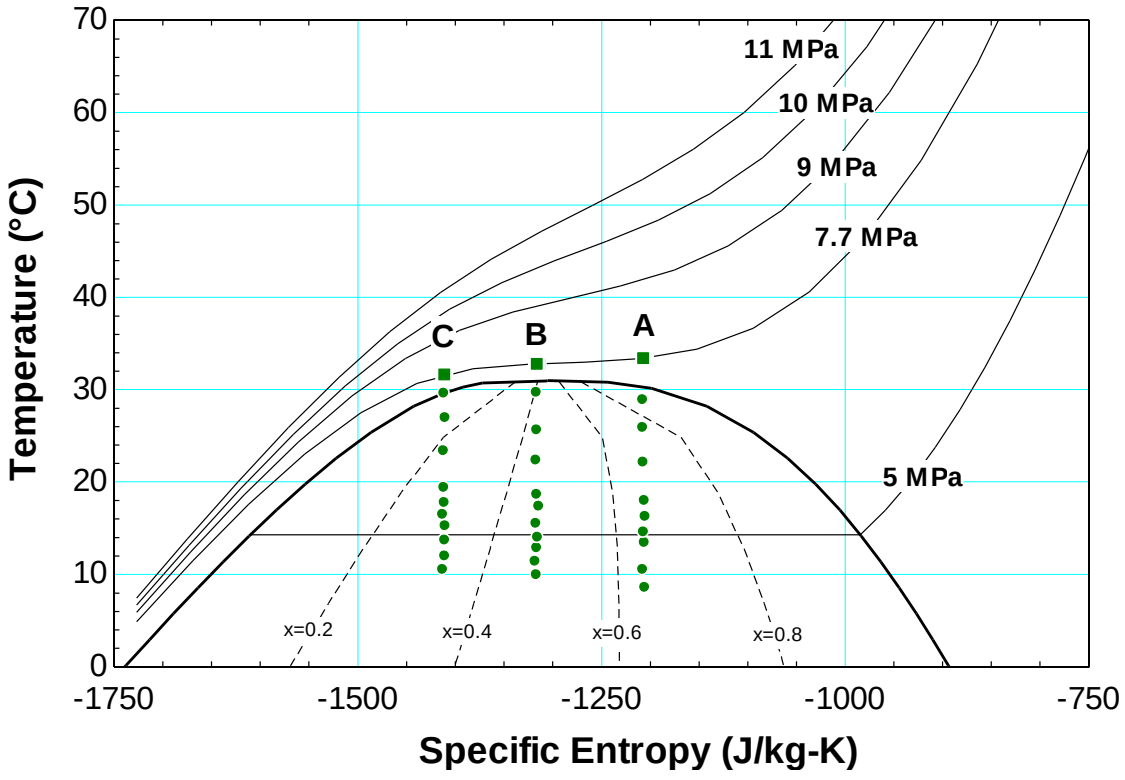


**Figure 40. Inlet conditions and approximate outlet conditions for data sets A, B, and C collected with Orifice B on a temperature-specific entropy diagram.**

Figure 41 shows the upstream stagnation conditions and downstream stagnation conditions for data sets A, B, and C collected with Orifice B on a temperature-specific entropy diagram. In this case, the downstream stagnation condition is defined by the measured downstream pressure, and the upstream stagnation enthalpy. Therefore, the downstream stagnation condition corresponds to the condition in the pressure vessel at the test section outlet rather than the condition at the orifice outlet. For the remainder of this chapter, temperature-specific entropy diagrams showing the approximate orifice outlet conditions (i.e., isentropic assumption is applied as shown in Figure 40) will be used for discussion.

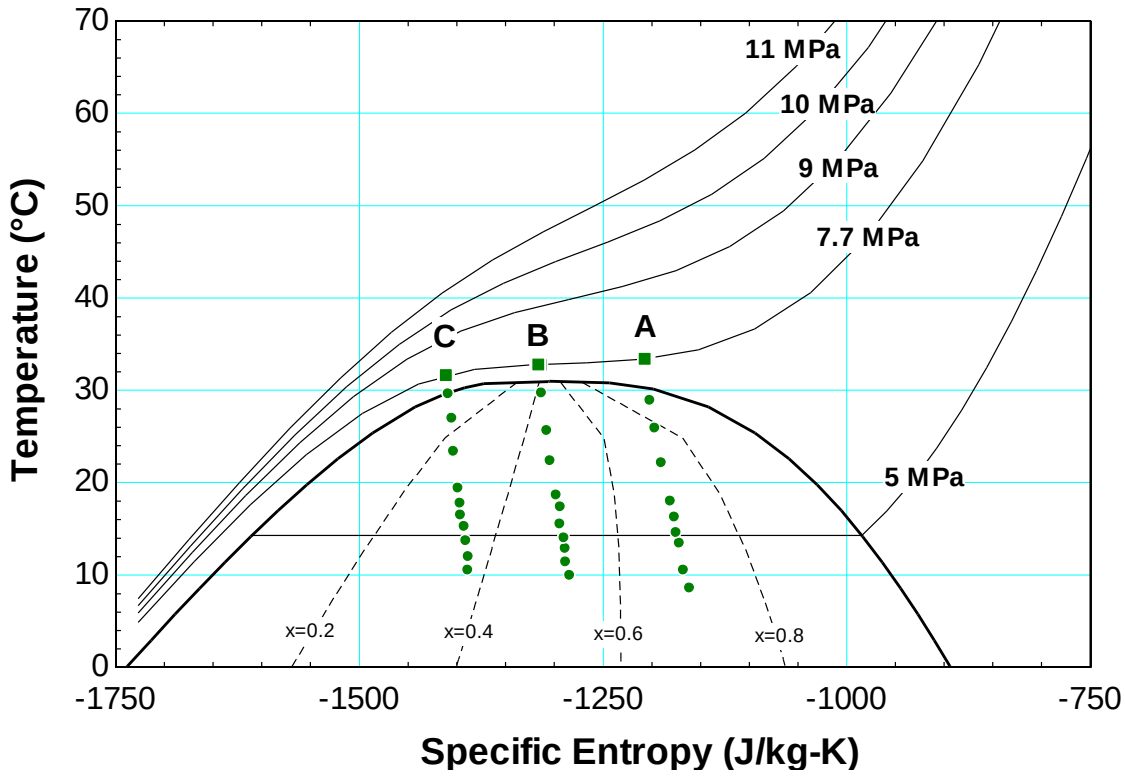


**Figure 41. Upstream stagnation conditions and downstream stagnation conditions for data sets A, B, and C collected with Orifice B on a temperature-specific entropy diagram.**

Figure 42 shows the experimentally measured mass flow rate as a function of pressure ratio for data sets A, B, and C collected with Orifice B. For each data point, the measured upstream stagnation pressure, measured upstream stagnation density, measured downstream stagnation pressure, and orifice diameter were used to calculate the isentropic mass flow rate., The single-phase model for isentropic expansion of a fluid was used for single-phase outlet conditions. For two-phase outlet conditions, the isentropic Homogeneous Equilibrium Model (HEM) and the isentropic Separated Flow Model (SFM) were both used. For data sets A, B, and C, the upstream stagnation pressure was 7.7 MPa, which is close to the critical pressure (7.39 MPa). As a result, all data collected experienced two-phase outlet conditions, as shown in Figure 40. The

isentropic HEM mass flow rate and the isentropic SFM mass flow rate as functions of pressure ratio are also shown in Figure 42.

Moody's [21] and Fauske's correlations for the slip ratio [23] both provide accurate predictions of the behavior of the data, which will be discussed later on. SFM results shown in the figures were determined using Moody's correlation.

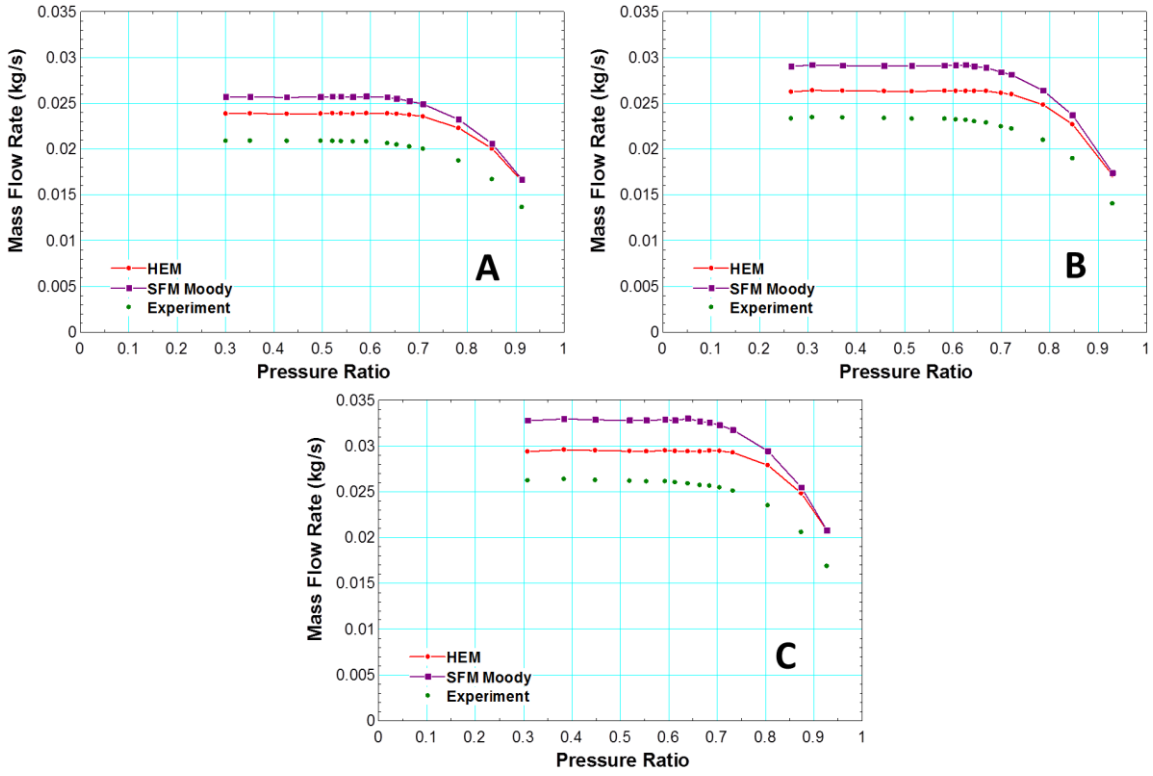


**Figure 42. Measured mass flow rate, isentropic homogeneous equilibrium model (HEM) mass flow rate, and separated flow model (SFM) mass flow rate as functions of pressure ratio for data sets A, B, and C collected with Orifice B.**

A discharge coefficient is defined for each data point as the ratio of the measured mass flow rate to the isentropic mass flow rate. For two-phase outlet conditions, discharge coefficients were calculated using both the isentropic HEM and the isentropic SFM. Figure 43 shows the discharge coefficient, defined with the isentropic HEM and the

isentropic SFM for two-phase outlet conditions, as a function of pressure ratio for data sets A, B, and C collected with Orifice B. In general, variations in the discharge coefficient with respect to pressure ratio are due to improper predictions of the physics of the flow by the isentropic model. For example, the shapes of the isentropic HEM mass flow rate curves are noticeably different than the shapes of the measured mass flow rate curves in Figure 42. As a result, there are variations in the discharge coefficients defined with the isentropic HEM with respect to pressure ratio in Figure 43. As the outlet conditions falls further into the two-phase region (i.e., pressure ratio decreases), the discharge coefficient defined with the isentropic HEM increases until the critical pressure ratio is reached. On the contrary, the shapes of the isentropic SFM mass flow rate curves match the shapes of the measured mass flow rate curves in Figure 42 quite well. As a result, the discharge coefficients defined with the isentropic SFM remain constant with respect to pressure ratio for tests A, B, and C, as shown in Figure 43. This observation is useful, as it allows for the data to be predicted accurately, independent of pressure ratio and inlet conditions with a single value for the discharge coefficient applied to the isentropic SFM with Moody's slip ratio.

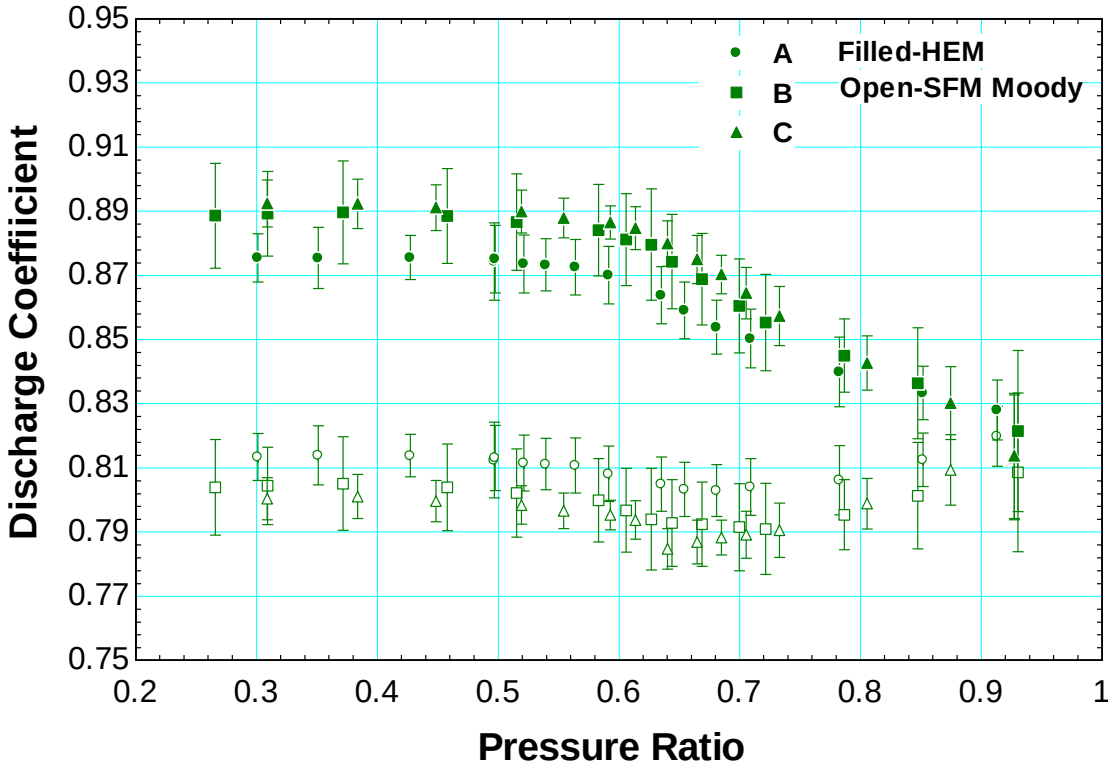


**Figure 43. Discharge coefficient, defined with isentropic HEM and isentropic SFM for two-phase outlet conditions, as a function of pressure ratio for data sets A, B, and C collected with Orifice B.**

The only assumption that differentiates the isentropic HEM from the isentropic SFM is that of equal velocities between the liquid and vapor phases. Therefore, the inability of the isentropic HEM to capture the physics of data sets A, B, and C is likely due to a difference in the velocities of the phases. Figure 44 shows the slip ratio for data sets A, B, and C, defined as the ratio of the velocity of the vapor to the velocity of the liquid, as a function of pressure ratio, determined with Moody's [21] and Fauske's [23] correlations. The correlations follow the form of Equation (73), where $n$ is 1/3 for Moody's correlation and 1/2 for Fauske's correlation. As the outlet condition falls further into the two-phase region (i.e., pressure ratio decreases), the ratio of the density of the liquid phase to the density of the vapor phase increases, and therefore the slip ratio

increases. Fauske's correlation predicts a slightly higher slip ratio than Moody's correlation.

$$S = \left(\frac{\rho_f}{\rho_g}\right)^n \tag{73}$$

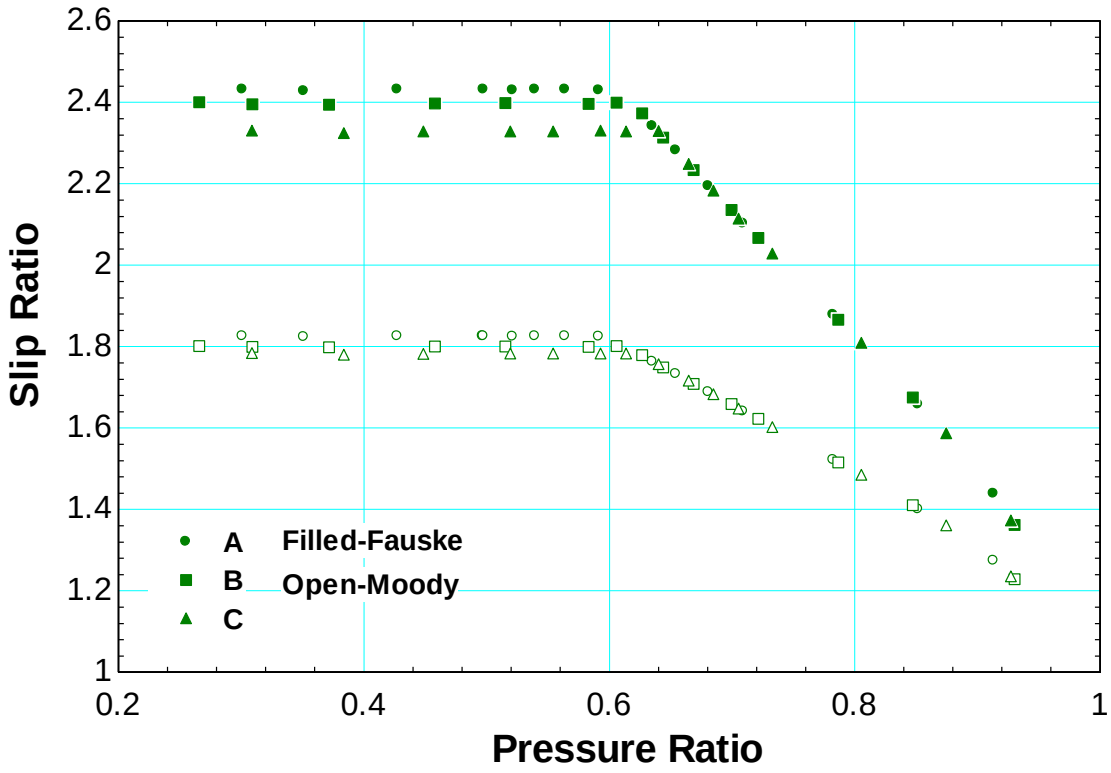


**Figure 44. Moody and Fauske slip ratios as functions of pressure ratio for data sets A, B, and C collected with Orifice B.**

Figure 45 shows the discharge coefficient defined with the isentropic SFM using both Moody and Fauske's correlations as a function of the pressure ratio for data sets A, B, and C collected with Orifice B. Within the error due to experimental measurements, the two correlations provide the same results.

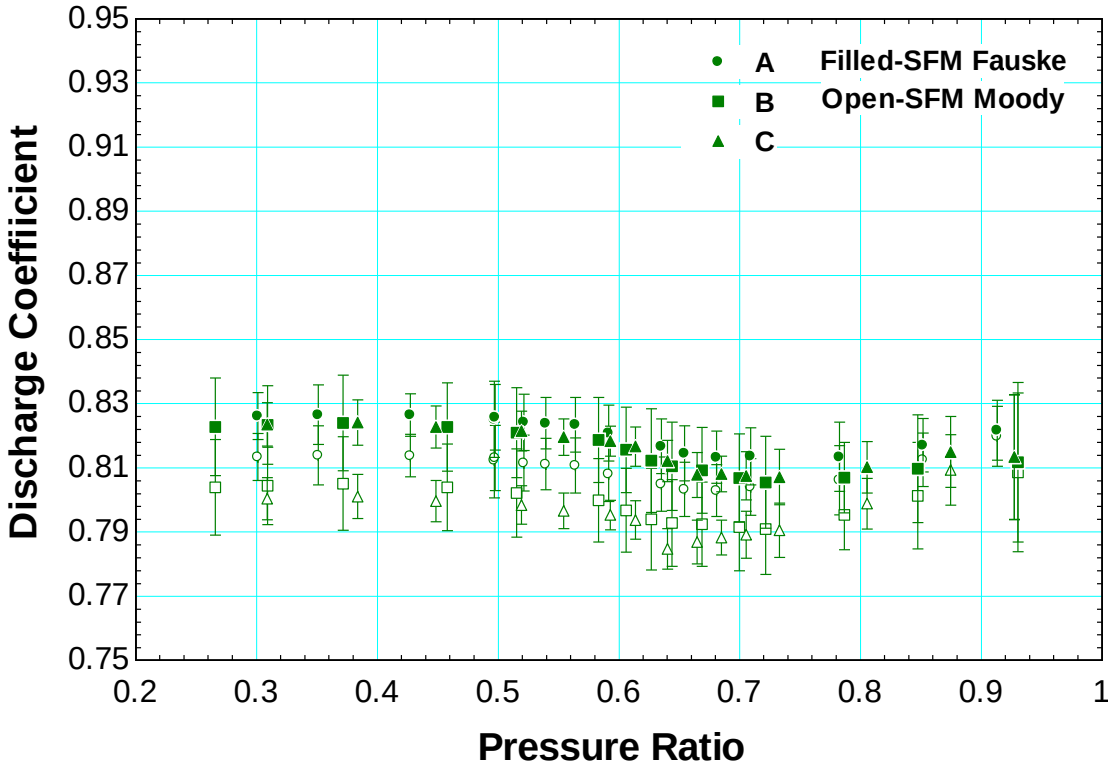


**Figure 45. Discharge coefficient defined by the isentropic SFM using both Moody and Fauske's correlations as a function of the pressure ratio for data sets A, B, and C collected with Orifice B.**

Figure 46 shows the inlet conditions and approximate orifice outlet conditions for data sets D, E, and F collected with Orifice B on a temperature-specific entropy diagram. Data sets D, E, and F have a higher inlet pressure than data sets A, B, and C, which results in more data corresponding to single-phase outlet conditions.

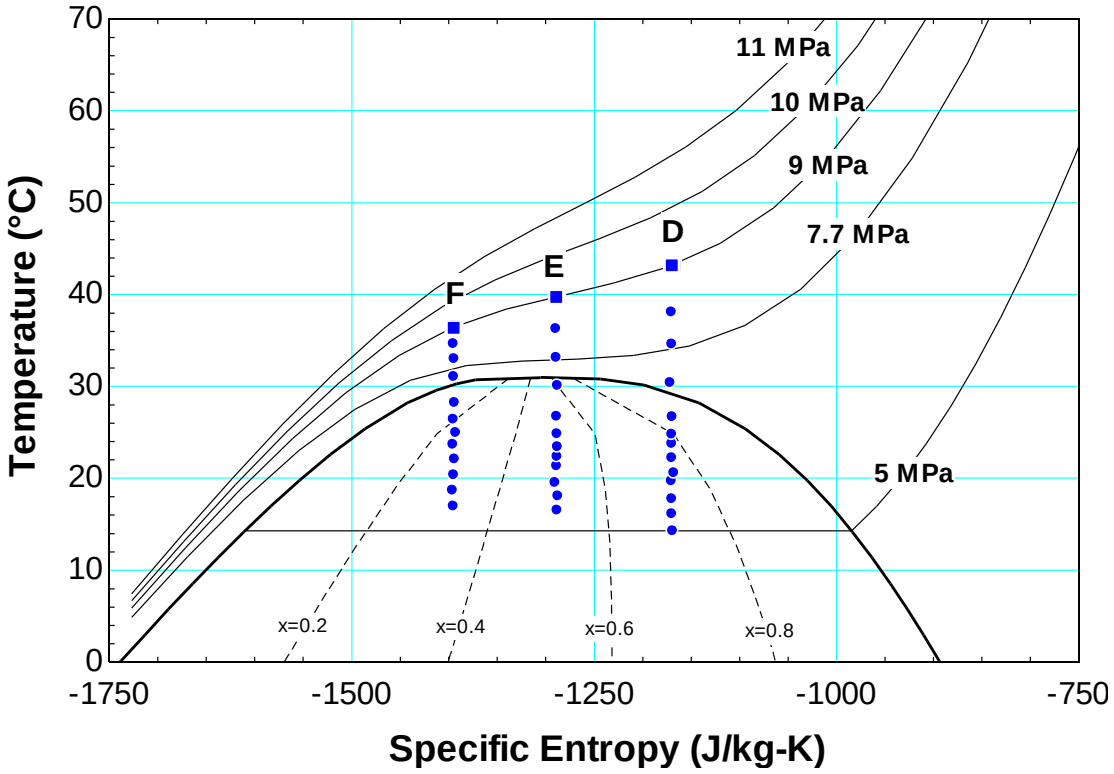


**Figure 46. Inlet conditions and approximate outlet conditions for data sets D, E, and F collected with Orifice B on a temperature-specific entropy diagram.**

Figure 47 shows the experimentally measured mass flow rate and the isentropic mass flow rate as functions of pressure ratio for data sets D, E, and F collected with Orifice B. Data were collected for both single-phase and two-phase outlet conditions. For two-phase outlet conditions, both the isentropic SFM mass flow rate and the isentropic HEM mass flow rate are shown. SFM results shown in the figures were determined using Moody's correlation.

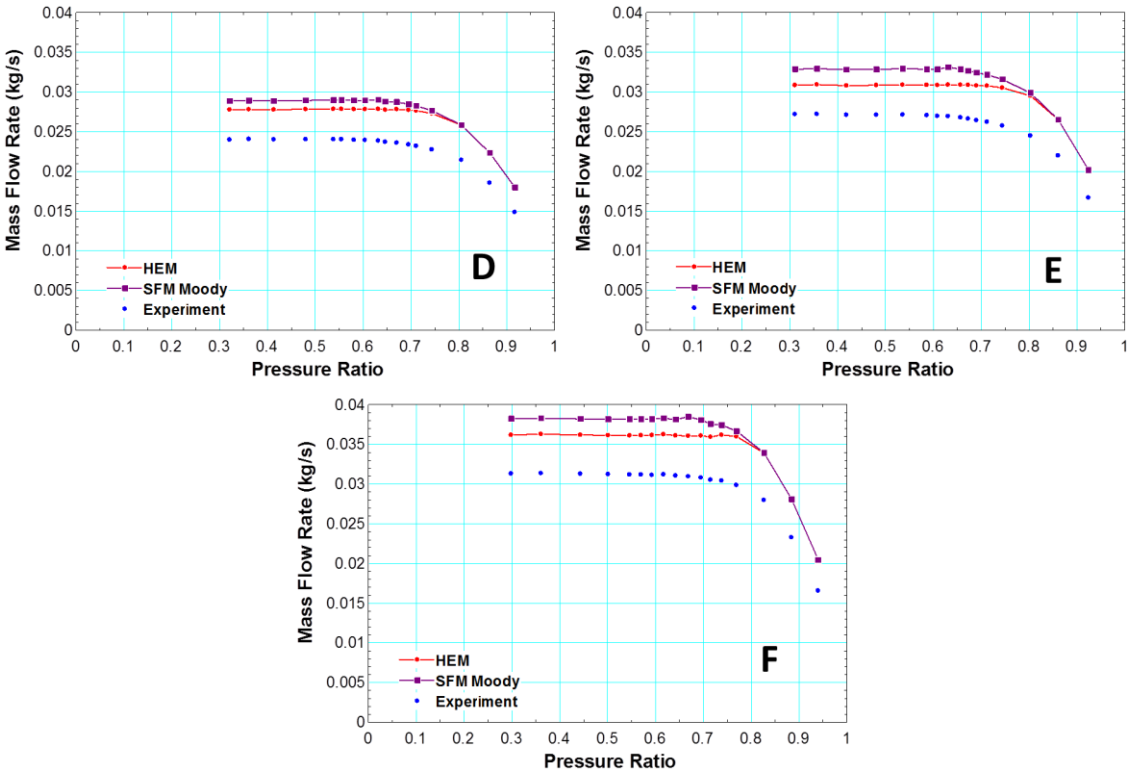


**Figure 47. Measured mass flow rate, isentropic homogeneous equilibrium model (HEM) mass flow rate, and separated flow model (SFM) mass flow rate as functions of pressure ratio for data sets D, E, and F collected with Orifice B.**

Figure 48 shows the discharge coefficient, defined with the isentropic HEM and the isentropic SFM for two-phase outlet conditions, as a function of pressure ratio for data sets D, E, and F collected with Orifice B. Figure 47 shows that for single-phase outlet conditions, the single-phase isentropic model predicts the shapes of the measured mass flow rate curves quite well. As a result, the discharge coefficient is constant with respect to pressure ratio for single-phase outlet conditions (high pressure ratios), as shown in Figure 48. For two-phase outlet conditions, the results are similar to those observed for data sets A, B, and C. The isentropic SFM predicts the shapes of the measured mass flow rate curves more accurately than the isentropic HEM, as shown in Figure 47. As a result, for two-phase outlet conditions, the discharge coefficient defined with the isentropic

HEM increases as the outlet condition falls further into the two-phase region (i.e., decreasing pressure ratios) while the discharge coefficient defined with the isentropic SFM remains constant with respect to pressure ratio, as shown in Figure 48. Once again, this is useful, as it allows for the data to be predicted accurately independent of pressure ratio and inlet conditions with a single value for the discharge coefficient applied to the single-phase isentropic model or the isentropic SFM with Moody's slip ratio depending on the outlet conditions. Also, to within the error associated with experimental measurements, this constant value for the discharge coefficient is equivalent to the value that was observed for data sets A, B, and C.

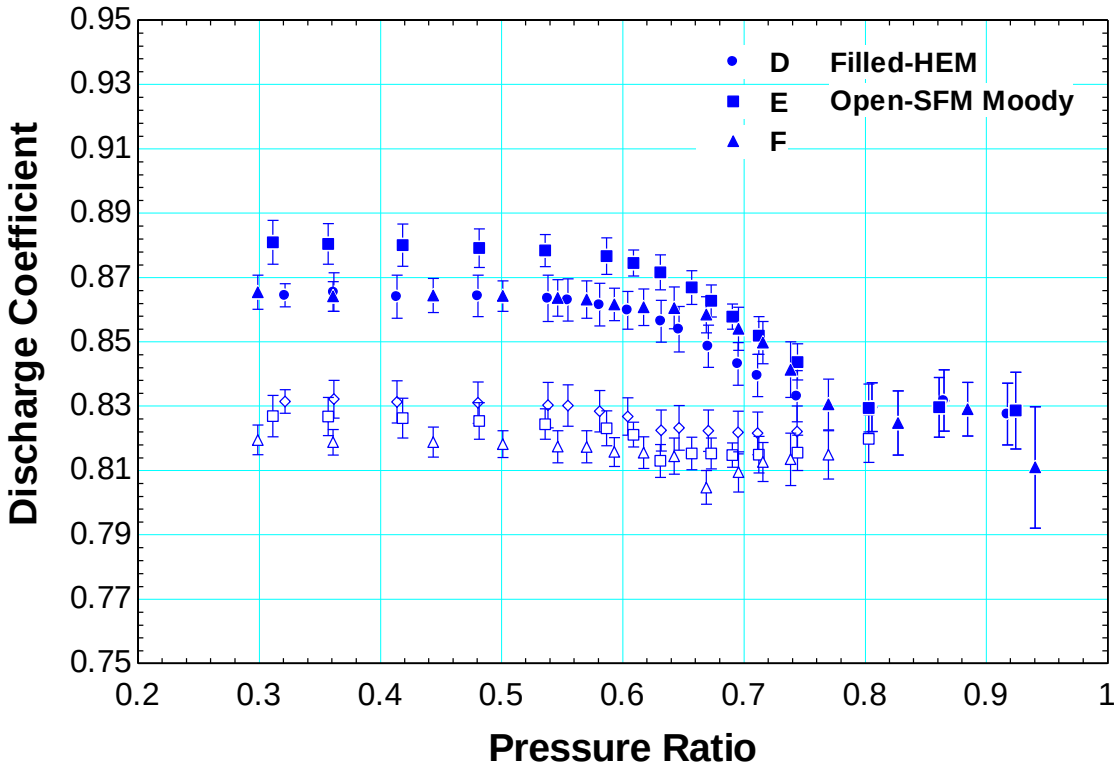


**Figure 48. Discharge coefficient, defined with isentropic HEM and isentropic SFM for two-phase outlet conditions, as a function of pressure ratio for data sets D, E, and F collected with Orifice B.**

Figure 49 shows the slip ratio for data sets D, E, and F, defined as the ratio of the velocity of the vapor to the velocity of the liquid, as a function of pressure ratio, determined with Moody's and Fauske's correlations. For single-phase outlet conditions, the slip ratio is one. As the outlet condition enters and falls further into the two-phase region (i.e., pressure ratio decreases), the ratio of the density of the liquid phase to the density of the vapor phase increases, and therefore the slip ratio increases.

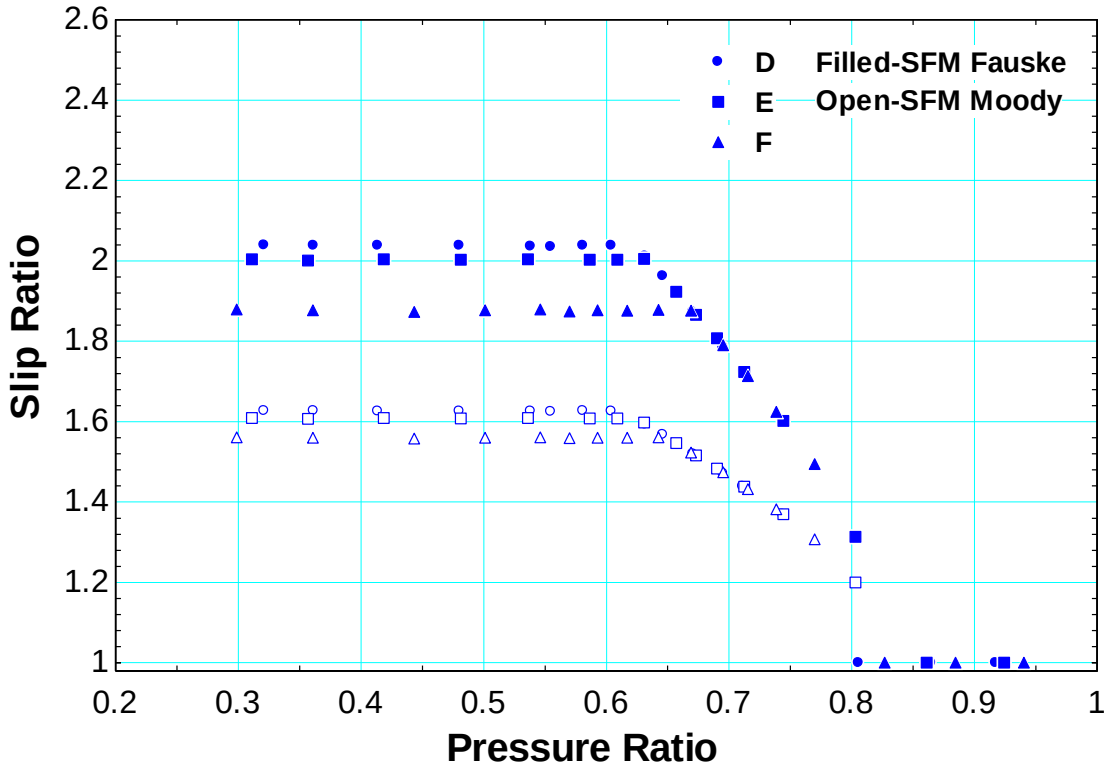


**Figure 49. Moody and Fauske slip ratios as functions of pressure ratio for data sets D, E, and F collected with Orifice B.**

Figure 50 shows the discharge coefficient defined by the isentropic SFM for two-phase outlet conditions using both Moody's and Fauske's correlations as a function of the pressure ratio for data sets D, E, and F collected with Orifice B. Within the error due to experimental measurements, the two correlations provide the same result.

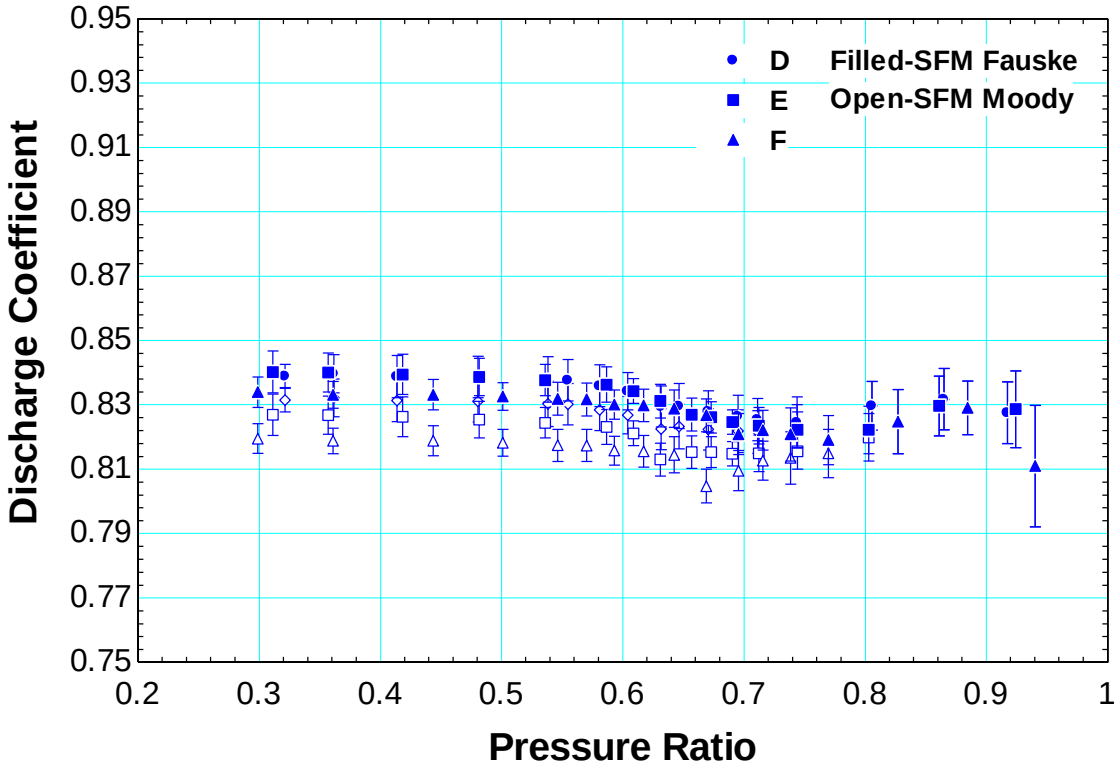


**Figure 50. Discharge coefficient defined by the isentropic SFM using both Moody and Fauske's correlations as a function of the pressure ratio for data sets D, E, and F collected with Orifice B.**

Figure 51 shows the inlet conditions and approximate orifice outlet conditions for data sets G, H, and I collected with Orifice B on a temperature-specific entropy diagram. The majority of the data that were collected for these sets correspond to single-phase outlet conditions.

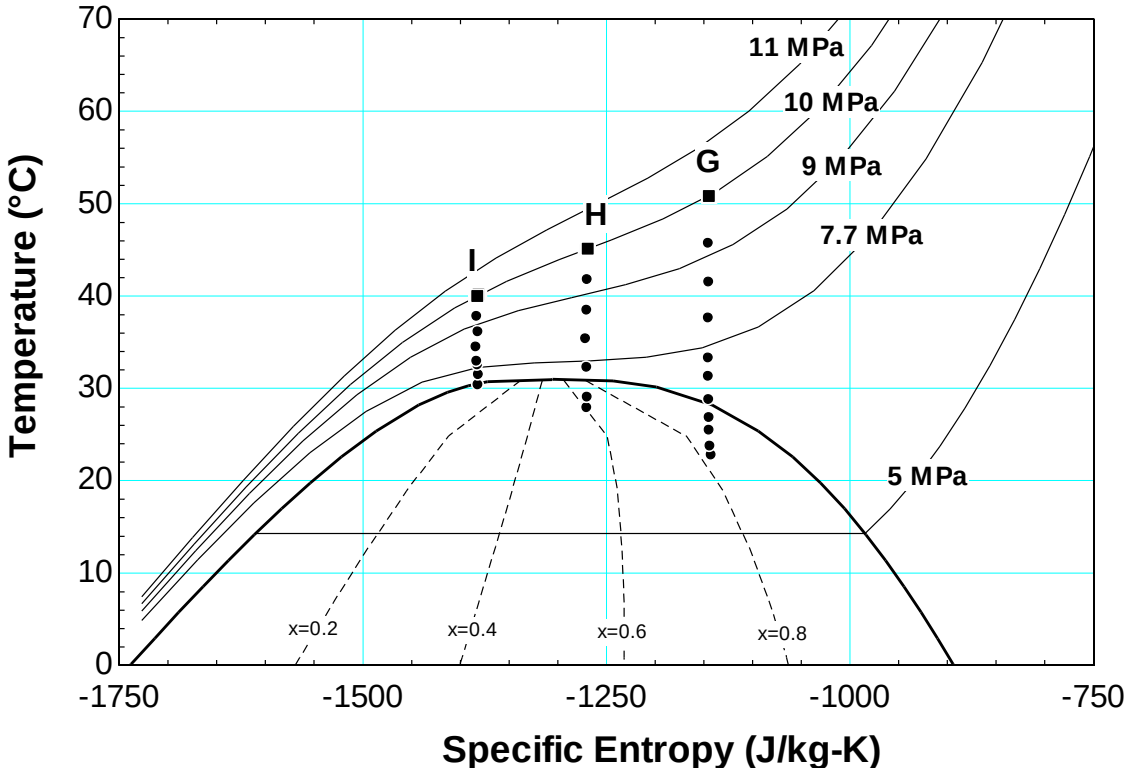


**Figure 51. Inlet conditions and approximate outlet conditions for data sets G, H, and I collected with Orifice B on a temperature-specific entropy diagram.**

Figure 52 shows the experimentally measured mass flow rate and the isentropic mass flow rate as functions of pressure ratio for data sets G, H, and I collected with Orifice B. For two-phase outlet conditions, both the isentropic SFM mass flow rate and the isentropic HEM mass flow rate are shown. SFM results shown in the figures were determined using Moody's correlation. However, the isentropic HEM and the isentropic SFM results are indistinguishable.

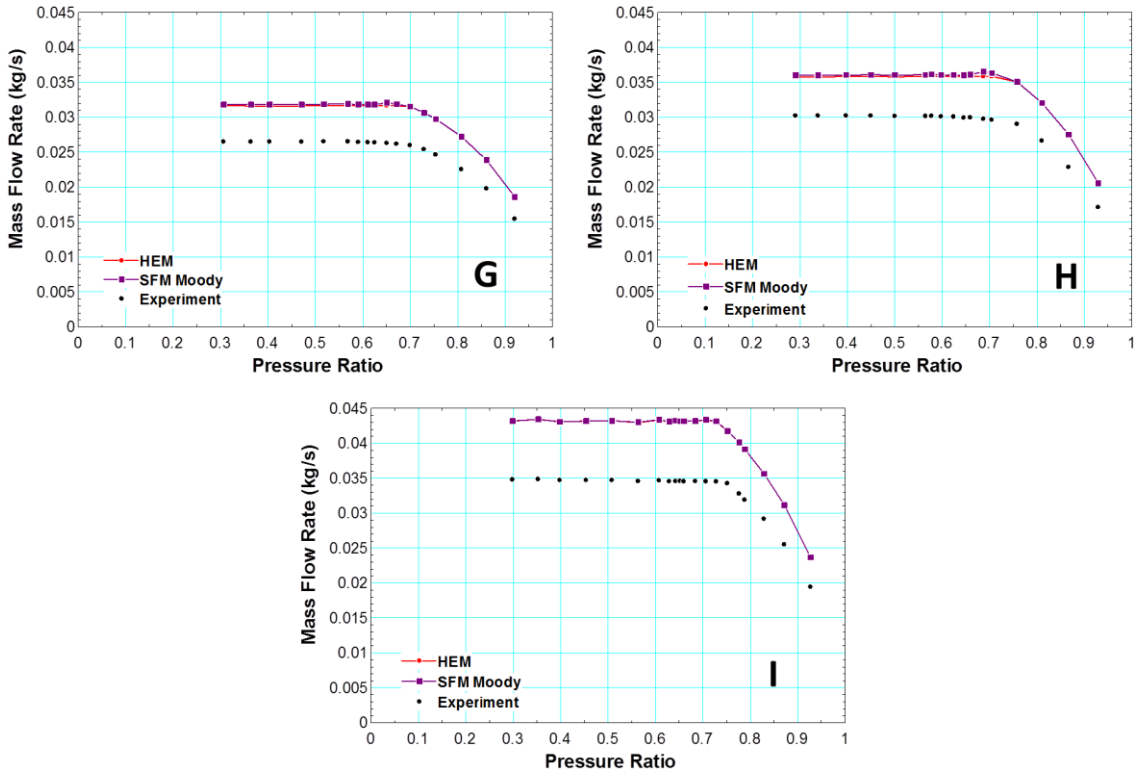


**Figure 52. Measured mass flow rate, isentropic homogeneous equilibrium model (HEM) mass flow rate, and separated flow model (SFM) mass flow rate as functions of pressure ratio for data sets G, H, and I collected with Orifice B.**

Figure 53 shows the discharge coefficient, defined with the isentropic HEM and the isentropic SFM for two-phase outlet conditions, as a function of pressure ratio for data sets G, H, and I collected with Orifice B. The figure shows that for single-phase outlet conditions, the discharge coefficient remains fairly constant with respect to pressure ratio. For two-phase outlet conditions, the discharge coefficient also remains constant when it is defined with both the isentropic HEM and the isentropic SFM. This is due to the small ratios of the density of the liquid phase to the density of vapor phase and the resulting insignificance of slip between the phases. It is interesting to note that the critical pressure ratio for data set I occurs near the saturation point, as shown in Figure 51. There is a reduction in the discharge coefficient with decreasing pressure ratio at this

point, as shown in Figure 53. This behavior is more prevalent in data sets J, K, and L, and will be addressed in the discussion of these data sets. Data sets G, H, and I can be predicted accurately independent of pressure ratio and inlet conditions with a single value for the discharge coefficient applied to the single-phase isentropic model for single phase outlet conditions or to the isentropic SFM with Moody's or Fauske's slip ratio for two-phase outlet conditions.

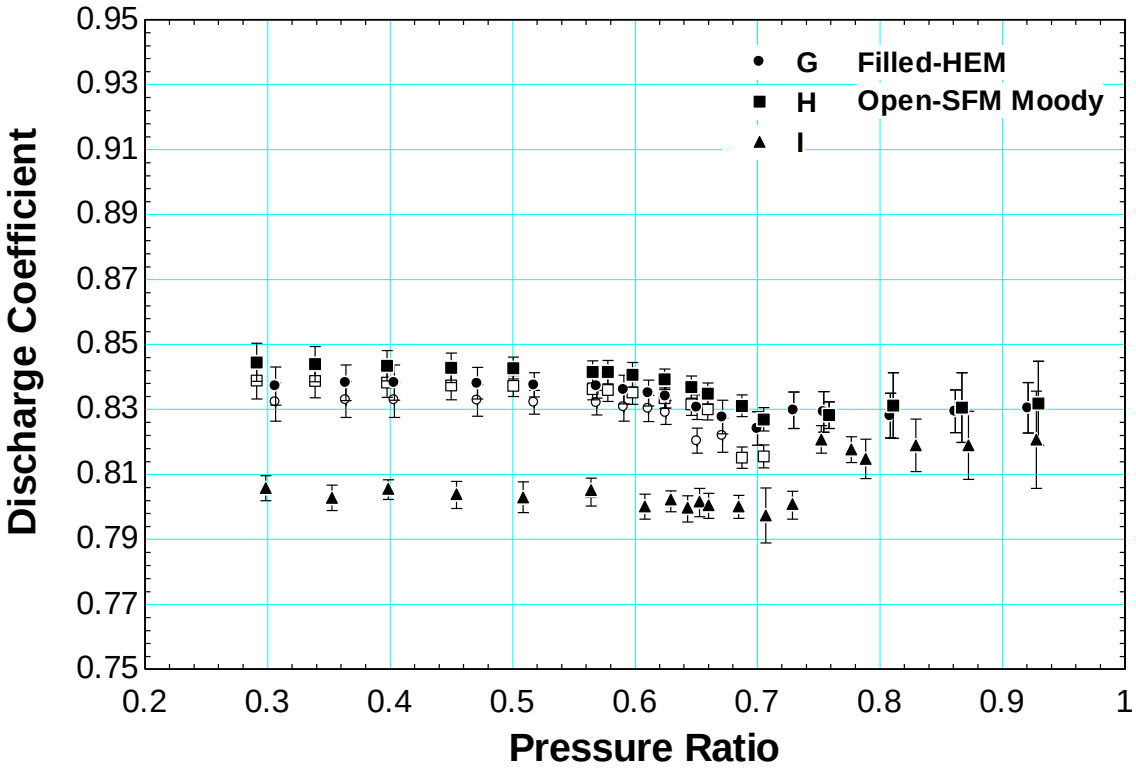


**Figure 53. Discharge coefficient, defined with isentropic HEM and isentropic SFM for two-phase outlet conditions, as a function of pressure ratio for data sets G, H, and I collected with Orifice B.**

Figure 54 shows the inlet conditions and approximate orifice outlet conditions for data sets J, K, and L collected with Orifice B on a temperature-specific entropy diagram. The critical pressure ratios for all three tests occur near the saturation points.

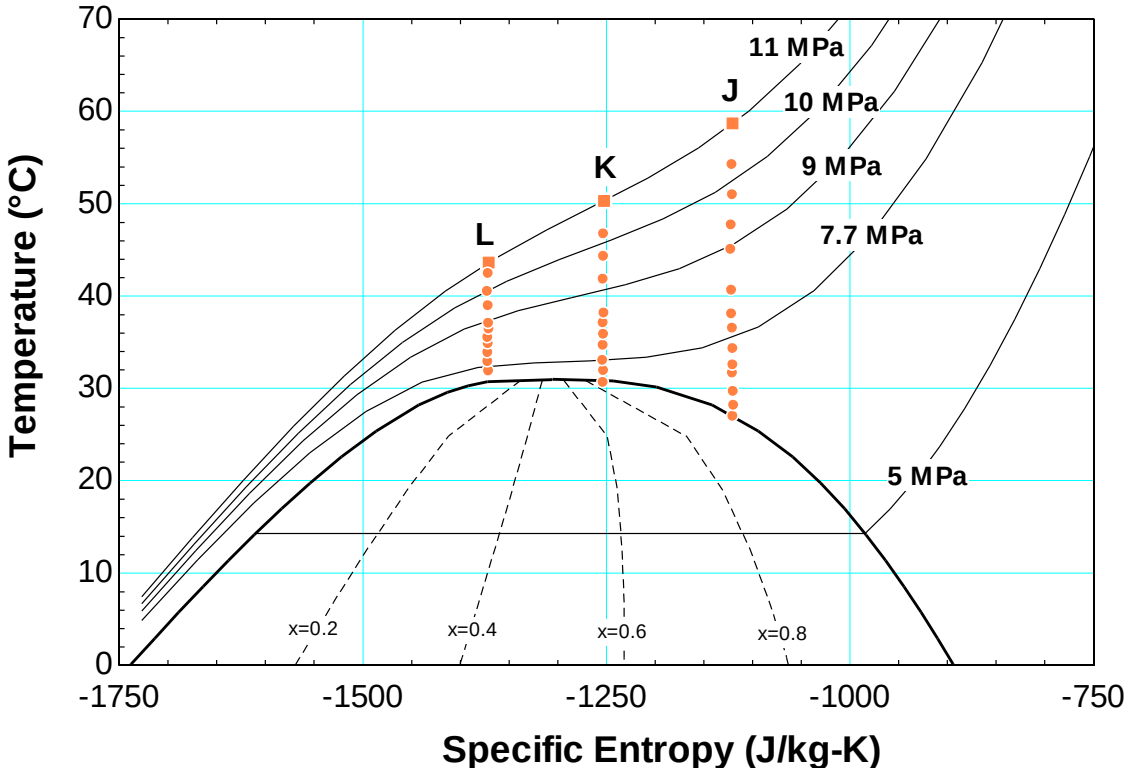


**Figure 54. Inlet conditions and approximate outlet conditions for data sets J, K, and L collected with Orifice B on a temperature-specific entropy diagram.**

Figure 55 shows the experimentally measured mass flow rate and the isentropic mass flow rate as functions of pressure ratio for data sets J, K, and L collected with Orifice B. Excluding the last subcritical point for each test, all of the data were collected for single-phase outlet conditions. The final subcritical data points for tests J and K correspond to two-phase outlet conditions. For these points, both the isentropic SFM mass flow rate and the isentropic HEM mass flow rate are shown. However, there is no visible difference between the two models.

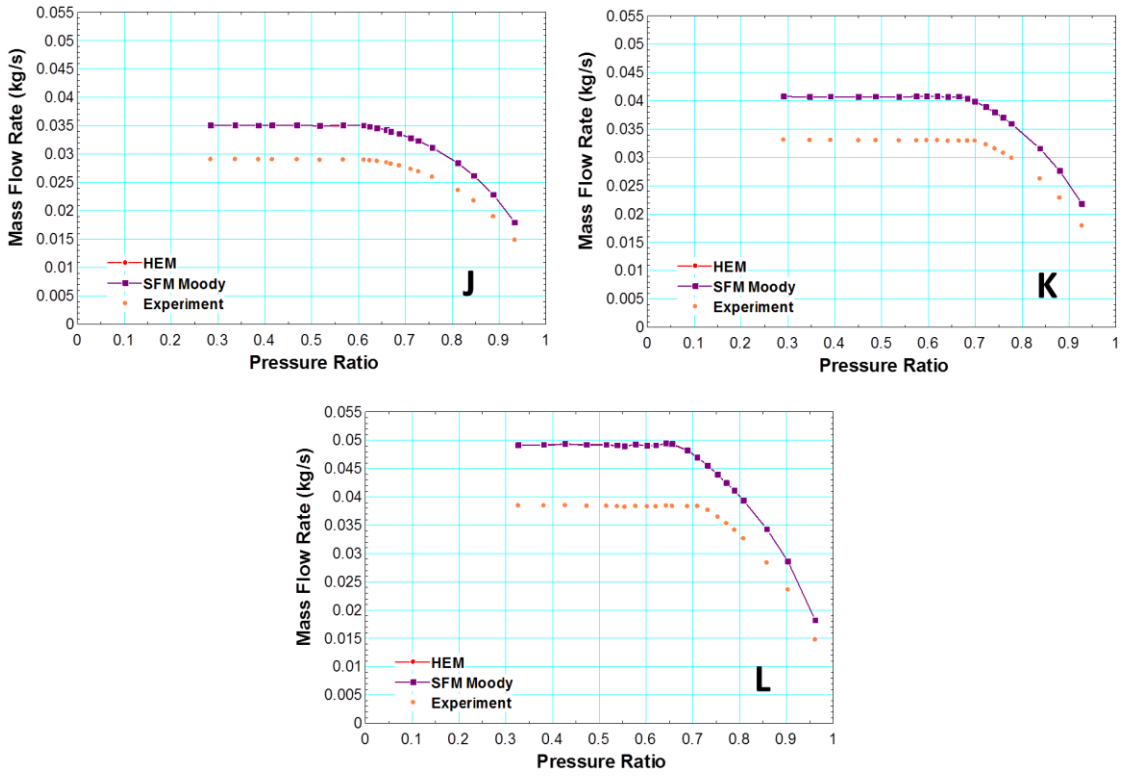


**Figure 55. Measured mass flow rate, isentropic homogeneous equilibrium model (HEM) mass flow rate, and separated flow model (SFM) mass flow rate as functions of pressure ratio for data sets J, K, and L collected with Orifice B.**

Figure 56 shows the discharge coefficient as a function of pressure ratio for data sets J, K, and L collected with Orifice B. For all three data sets, there is an abrupt reduction in the discharge coefficient with decreasing pressure ratio near the critical pressure ratio, as shown in Figure 56. The magnitude of the reduction increases with inlet density (moving from right to left on the temperature-specific entropy diagram).

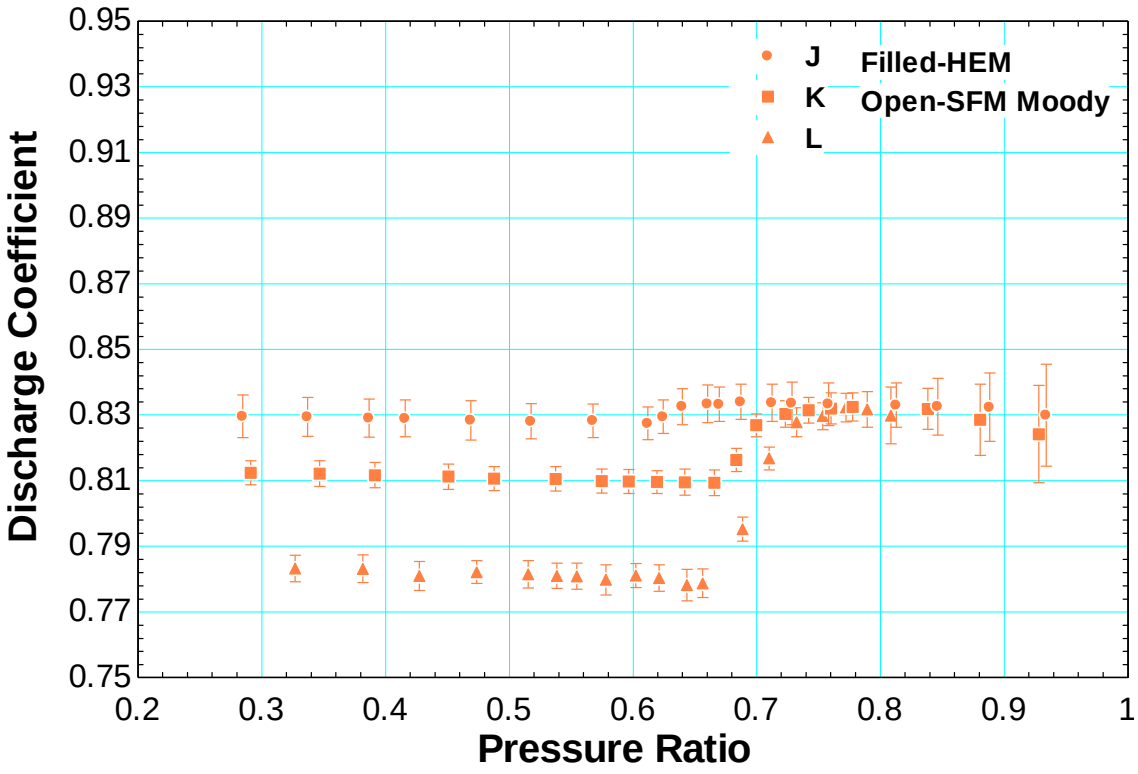


**Figure 56. Discharge coefficient, defined with isentropic HEM and isentropic SFM for two-phase outlet conditions, as a function of pressure ratio for data sets J, K, and L collected with Orifice B.**

The reductions in the discharge coefficients with decreasing pressure ratios in Figure 56 occur for downstream pressures near the saturation points. It is possible that two-phase flow occurs within the orifice near the vena contracta in low-pressure cavitation regions even for single-phase inlet and outlet conditions. Figure 57b shows the results of an axisymmetric CFD simulation performed by Yuan et al. [45] for the flow of S-$CO_2$ through Orifice A for an upstream stagnation pressure of 11MPa, an upstream stagnation density of 372 kg/$m^3$, and a downstream stagnation pressure of 7 MPa. The approximate (the isentropic assumption was used) inlet and outlet conditions for the simulation are shown on the temperature-entropy diagram in Figure 57a. The results in Figure 57b show the quality of the $CO_2$ within the orifice. A quality of 1 indicates single-phase $CO_2$.

Although the upstream and downstream stagnation conditions are in the single-phase region, two-phase flow occurs near the entrance of the orifice. The same result is observed in a simulation for an upstream stagnation pressure of 11 MPa, an upstream stagnation density of 498 kg/m$^3$, and a downstream stagnation pressure of 8 MPa, as shown in Figure 58.

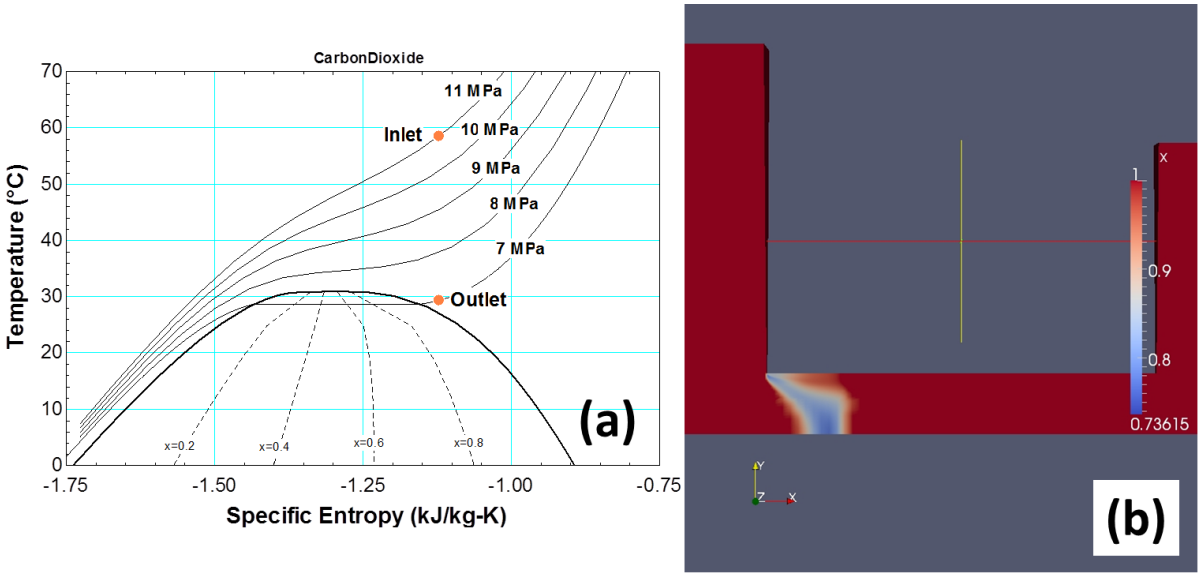


**Figure 57. (b) Results from a CFD simulation by Yuan et al. [45] for the flow of S-$CO_2$ through Orifice A for an upstream stagnation pressure of 11 MPa, an upstream stagnation density of 372 kg/m$^3$, and a downstream stagnation pressure of 7 MPa. (a)The approximate conditions are shown on the temperature-specific entropy diagram.**

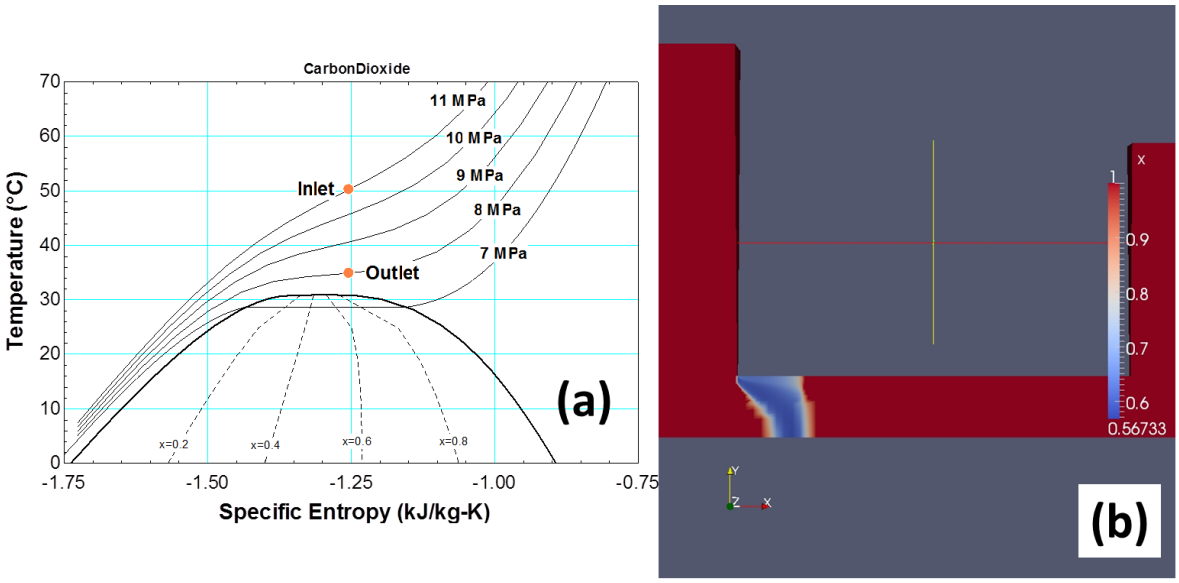


**Figure 58. (b) Results from a CFD simulation by Yuan et al. for the flow of S-$CO_2$ through Orifice A for an upstream stagnation pressure of 11 MPa, an upstream stagnation density of 498 kg/m$^3$, and a downstream stagnation pressure of 8 MPa. (a) The approximate conditions are shown on the temperature-specific entropy diagram.**

Based on Yuan's CFD results, the flow rates of the experimental data for data sets J, K, and L for downstream pressures near the saturation points may be limited by two-phase conditions in the vena contracta region even for single-phase inlet and outlet conditions. However, the isentropic models used to define the discharge coefficients are only based on the inlet and outlet conditions, which may explain the behavior observed in Figure 56.

Despite the interesting behavior of the discharge coefficients observed for data sets J, K, and L, the data can still be predicted accurately independent of pressure ratio and inlet conditions with a single value for the discharge coefficient applied to the single-phase isentropic model or the isentropic SFM with Moody's or Fauske's slip ratio depending on the outlet conditions.

In summary, for the data sets collected with Orifice A and Orifice B, a constant single-phase discharge coefficient of approximately 0.82 was observed. For two-phase outlet conditions, a constant discharge coefficient of approximately 0.82 was observed when the discharge coefficient was defined with the isentropic SFM with Moody's and Fauske's correlations for the slip ratio. When the discharge coefficient was defined with the isentropic HEM for two-phase outlet conditions, an increase in the discharge coefficient with decreasing pressure ratio was observed due to the inability of the model to capture slip between the liquid and vapor phases.

Figure 59 shows the mass flow rate predicted by applying a discharge coefficient of 0.82 to the isentropic model using the HEM for two-phase outlet conditions as a function of the experimentally measured mass flow rate for all of the data collected with Orifice A and Orifice B. The figure shows that this model predicts the majority of the experimental data within five percent. However, the predictions for many of the data points corresponding to two-phase outlet conditions are only predicted within 10% due to the invalid assumption of equal velocities of the liquid and vapor phases.

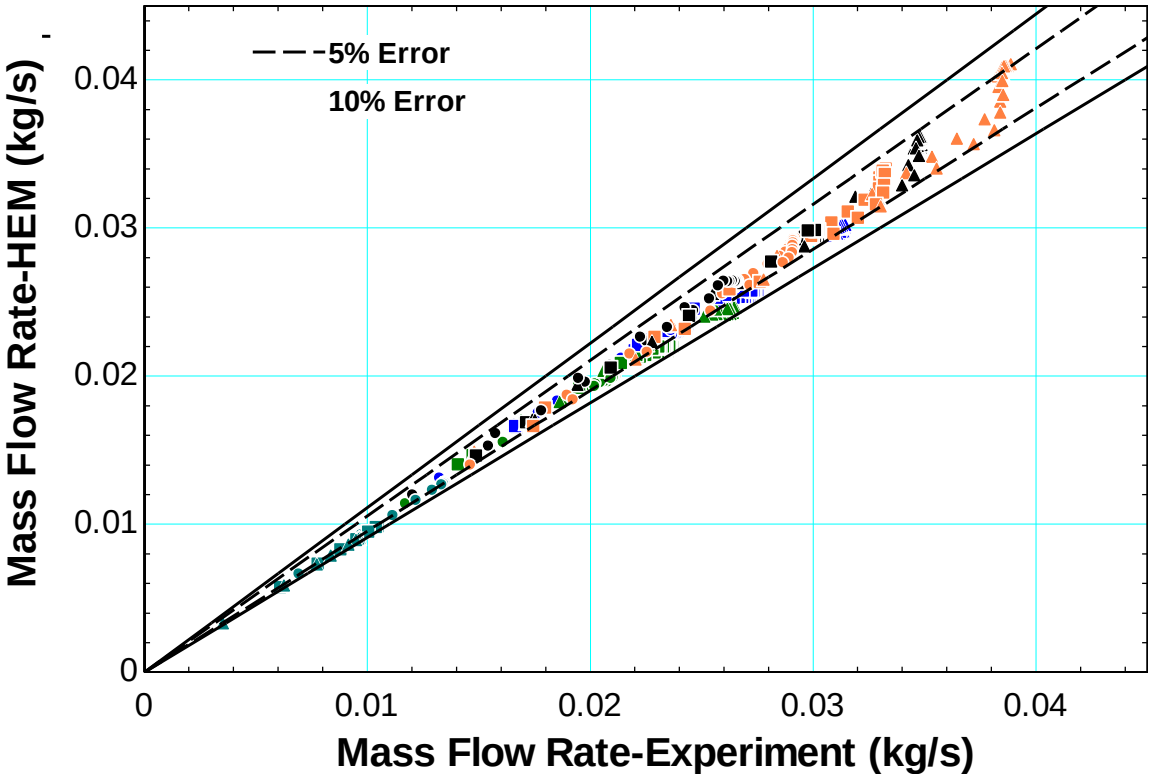


**Figure 59. Mass flow rate predicted by applying a discharge coefficient of 0.82 to the isentropic model using the HEM for two-phase outlet conditions as a function of the experimentally measured mass flow rate.**

Figure 60 shows the mass flow rate predicted by applying a discharge coefficient of 0.82 to the isentropic model using the SFM with Moody's correlation for the slip ratio for two-phase outlet conditions as a function of the experimentally measured mass flow rate for all of the data collected with Orifice A and Orifice B. The figure shows that this model predicts nearly all of the data within five percent.

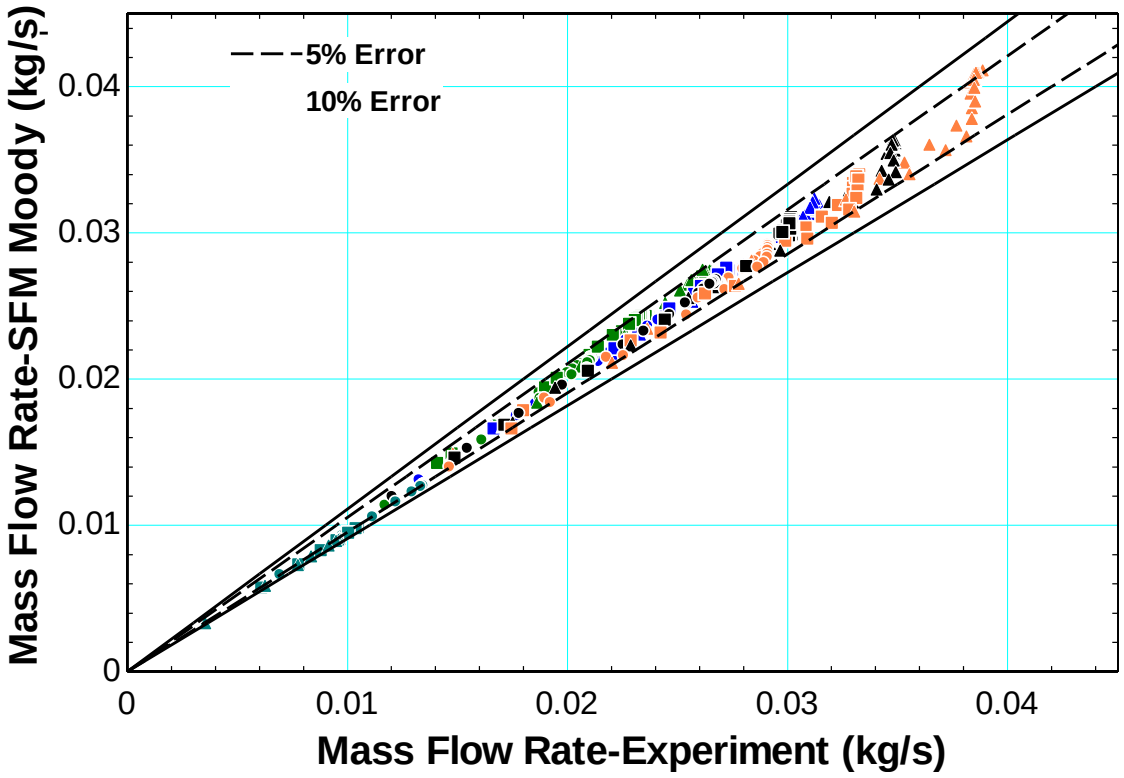


**Figure 60. Mass flow rate predicted by applying a discharge coefficient of 0.82 to the isentropic model using the SFM with Moody's correlation for the slip ratio for two-phase outlet conditions as a function of the experimentally measured mass flow rate.**

The results of these experiments are obviously useful for predicting flow rates of S-$CO_2$ through short orifices. For a given orifice geometry, upstream stagnation condition, and downstream pressure, the mass flow rate can be predicted within five percent by applying a discharge coefficient of 0.82 to the single-phase isentropic model for single-phase outlet conditions or the isentropic SFM with Moody's or Fauske's correlation for the slip ratio for two-phase outlet conditions. This model is also useful for predicting the form loss at the entrance to an orifice with a large L/D.

## 4.4 Major Losses Results

Figure 61 illustrates the methodology for applying the empirical form loss model to orifices with large L/D. The isentropic model with the discharge coefficient is applied at the orifice entrance, labeled as section A in Figure 61. Models for the friction, acceleration, and gravity losses are integrated along the remaining length of the orifice, labeled as section B in Figure 61. The modeling methodology for orifices with large L/D is discussed in detail in Chapter 2.

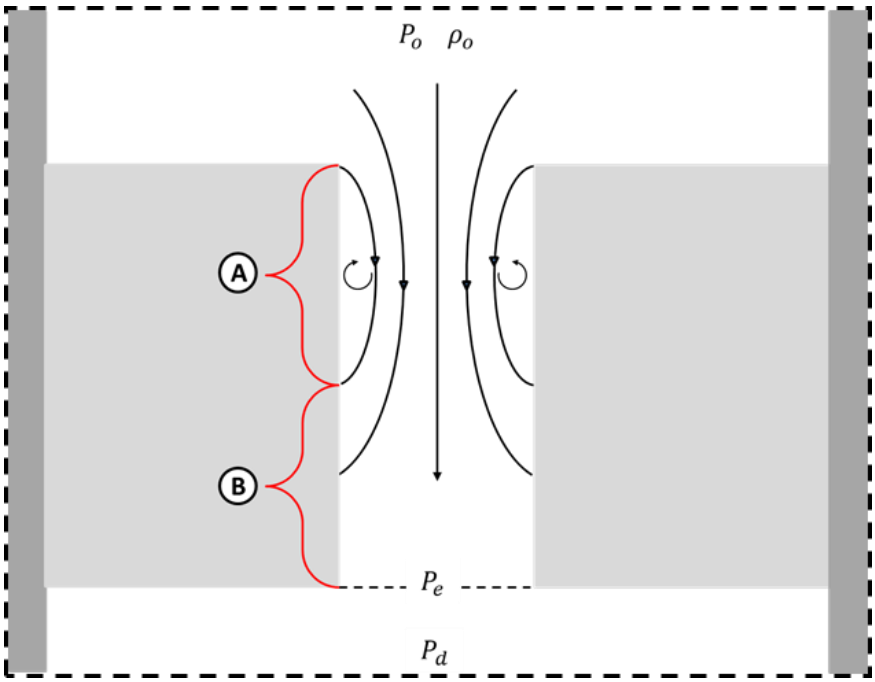


**Figure 61. Methodology for modeling the flow of S-$CO_2$ through orifices with large L/D.**
**A: Apply isentropic model with empirical discharge coefficient.**
**B: Apply models for major losses.**

In order to validate models for the major losses and compare various correlations for the friction factor, data were collected with Orifice C, which has a L/D of 20. Data were collected for all of the conditions displayed in Table 5 except for C, K, and L, which

were not collected due to time constraints and issues with the experimental facility. The HEM assumptions were used for modeling the major losses for two-phase conditions. After quantifying the geometry of the orifice, the upstream stagnation conditions, and the downstream stagnation pressure, the only piece of information in the major loss models left to vary was the correlation for the friction factor.

Figure 62 shows the inlet conditions and approximate orifice outlet conditions (estimated using the isentropic assumption) for data sets A, E, I, and J collected with Orifice C on a temperature-specific entropy diagram. These four data sets were selected for discussion since they encompass a wide range of inlet conditions.

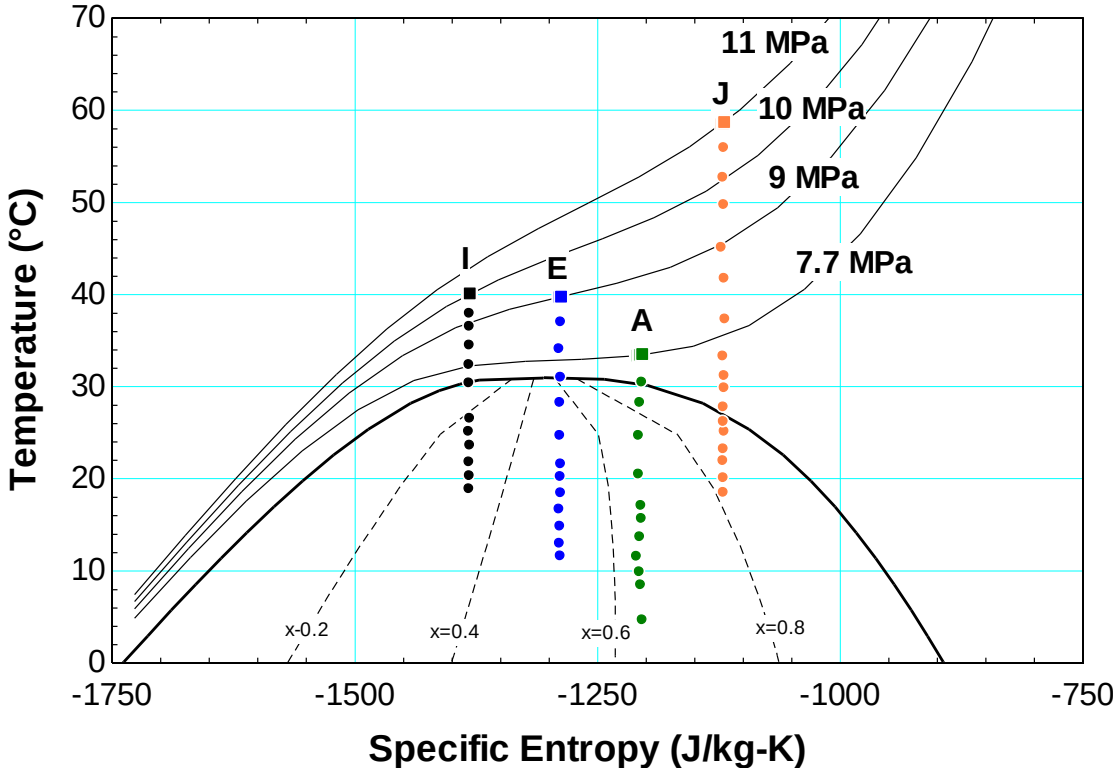


**Figure 62. Inlet conditions and approximate outlet conditions for data sets A, E, I, and J collected with Orifice B on a temperature-specific entropy diagram.**

Figure 63, Figure 64, Figure 65, and Figure 66 show the measured mass flow rates and mass flow rates predicted by the model with various friction factors (discussed in Chapter 2) as functions of the pressure ratio for data sets A, E, I, and J collected with Orifice C, respectively. The figures show that for all four data sets, the model predicts the data accurately when Colebrook's correlation for the friction factor is used. Also, the HEM assumptions appear to be valid for the major loss models, since the model accurately predicts the behavior of the data for two-phase conditions. It is not surprising that Colebrook's correlation provides a better prediction than Blasius' and Popov's correlations since it accounts for the roughness of the orifice, while the other two do not.

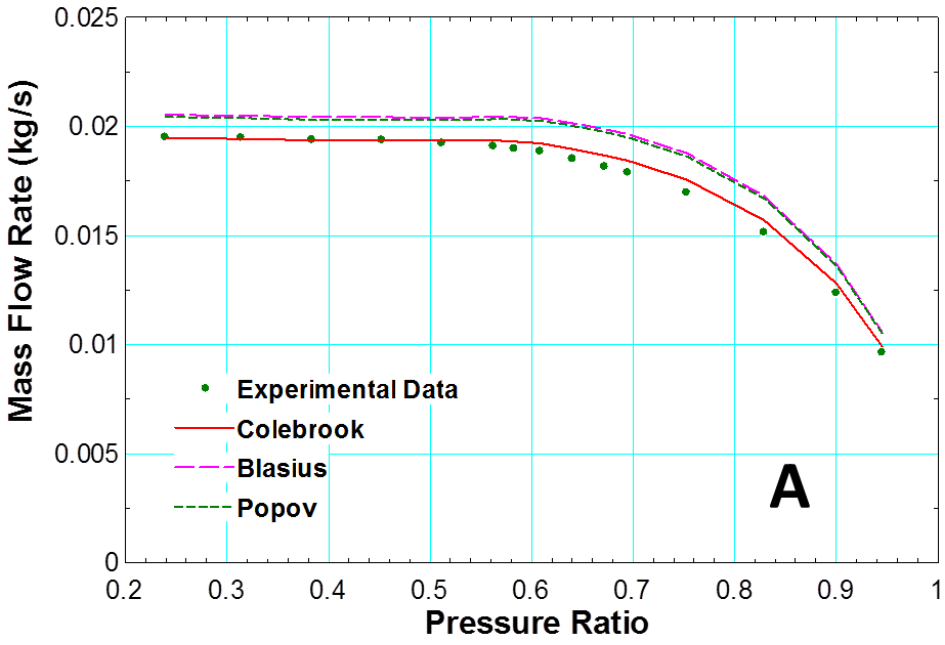


**Figure 63. Measured mass flow rate and mass flow rate predicted by model with various friction factors as functions of pressure ratio for data set A collected with Orifice C.**

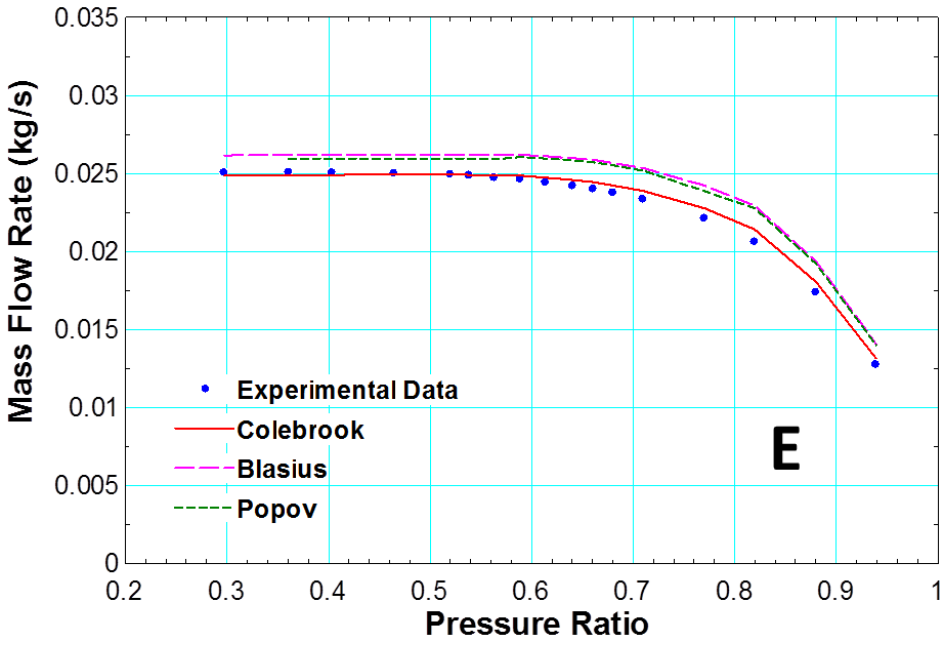


**Figure 64. Measured mass flow rate and mass flow rate predicted by model with various friction factors as functions of pressure ratio for data set E collected with Orifice C.**

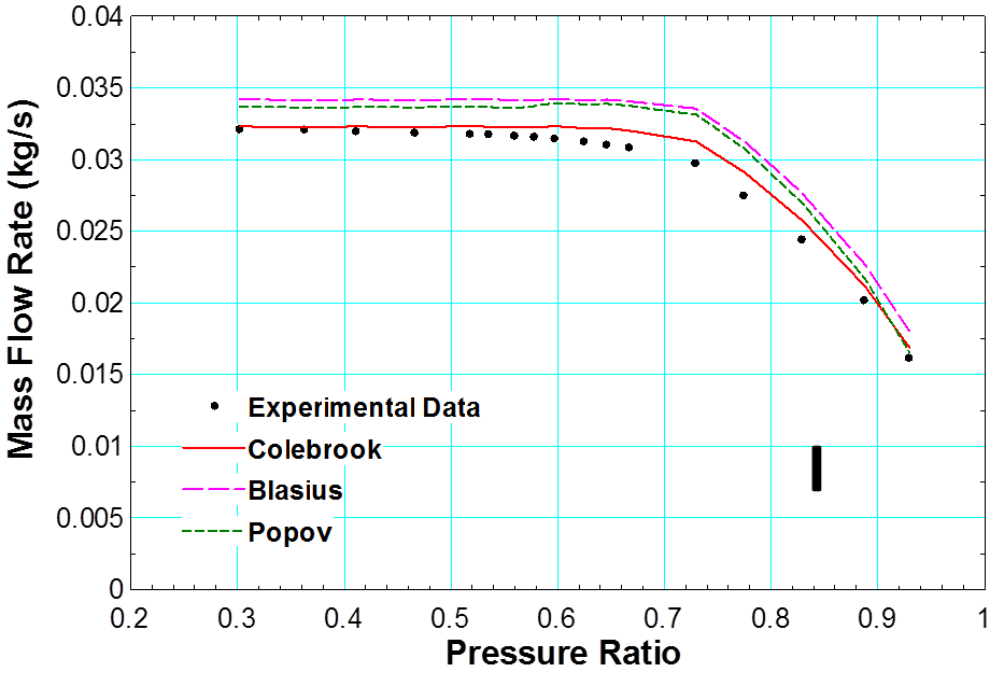


**Figure 65. Measured mass flow rate and mass flow rate predicted by model with various friction factors as functions of pressure ratio for data set I collected with Orifice C.**

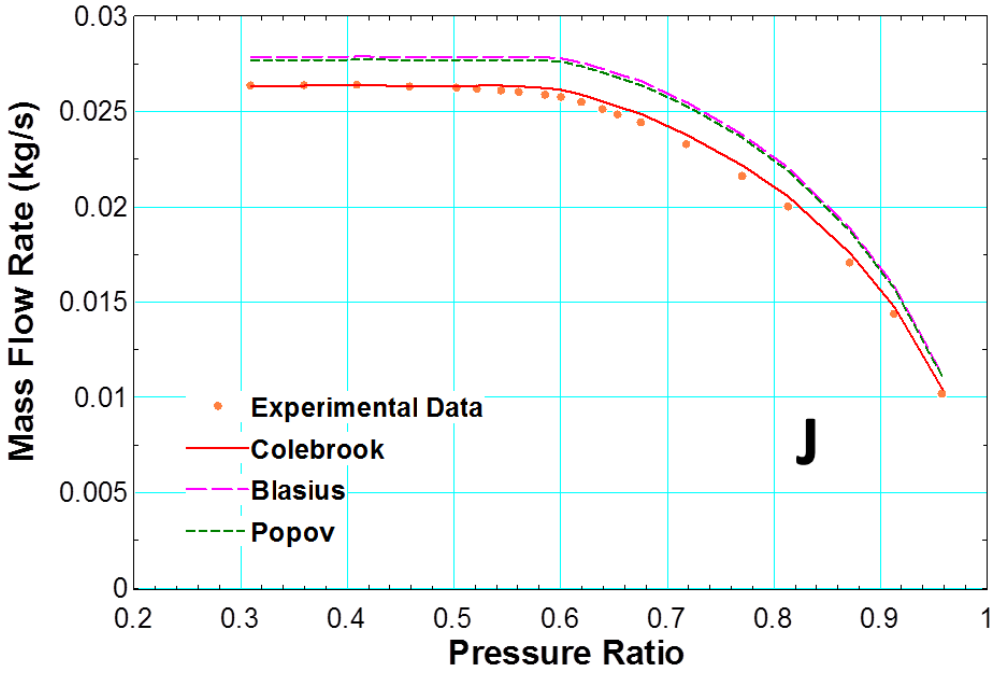


**Figure 66. Measured mass flow rate and mass flow rate predicted by model with various friction factors as functions of pressure ratio for data set J collected with Orifice C.**

Figure 67 shows the mass flow rate predicted with the model for orifices with large L/D with Colebrook's correlation for the friction factor as a function of the experimentally measured mass flow rate for all of the data that were collected with Orifice C. The figure shows that this model predicts all of the experimental data within five percent. Once again, this result is very useful for a variety of applications associated in which models for the form losses and the major losses associated with flow of S-$CO_2$ through orifices are required.

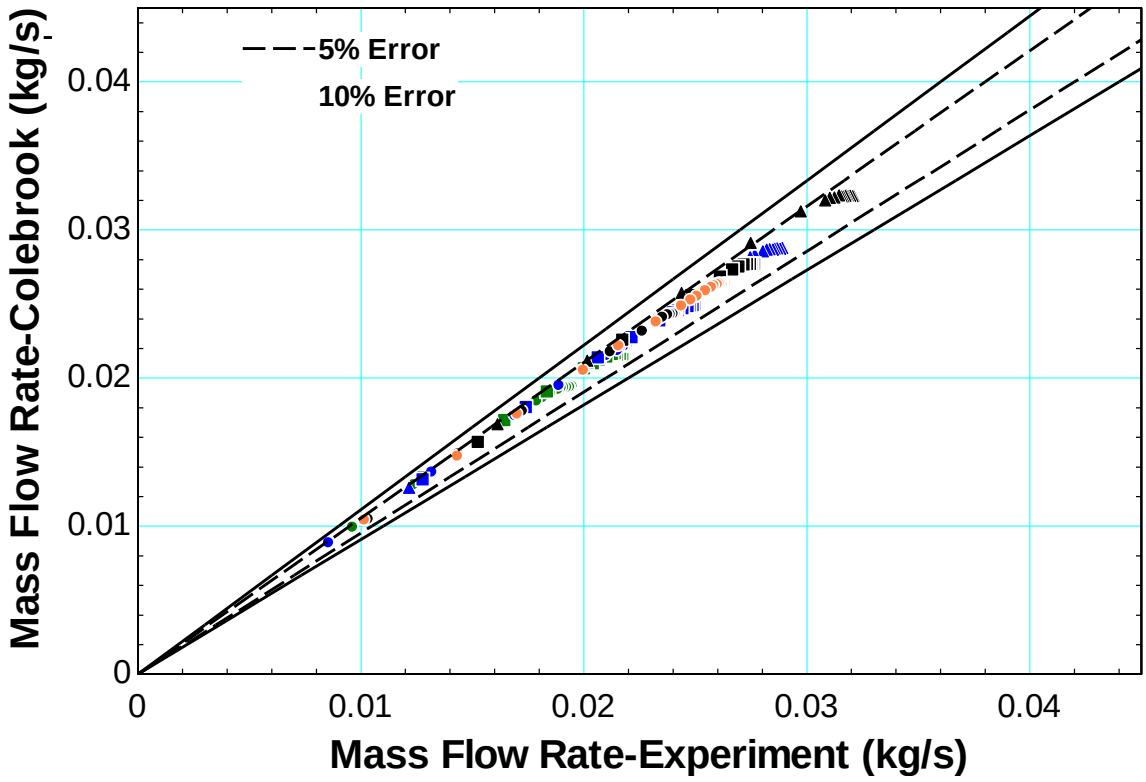


**Figure 67. Mass flow rate predicted with the model for orifices with large L/D with Colebrook's correlation for the friction factor as a function of the experimentally measured mass flow rate for data collected with Orifice C.**

# 5 Conclusions and Future Work

As a result of relatively high efficiencies and low capital costs, the S-$CO_2$ Brayton Cycle is a promising technology for power production. However, the ability to predict the flow of supercritical and two-phase $CO_2$ through restrictions must be improved in order to analyze pipe ruptures, valves, and turbomachinery seals. To this end, the study described herein provides a comprehensive data set for the flow of S-$CO_2$ through sharp-edge orifices with small and large L/D over a broad range of inlet conditions for pressure ratios both above and below the critical pressure ratio. Data were obtained for orifice inlet pressures ranging from 5 MPa to 11 MPa and inlet densities ranging from 86.5 kg/m$^3$ to 630 kg/m$^3$.

A model for the form losses associated with the contraction and expansion of the $CO_2$ at the orifice inlet was developed based on the data that were collected with orifices with small L/D. All of the data that were collected with orifices with small L/D are predicted within five percent by applying an empirical discharge coefficient of 0.82 to the single-phase isentropic model for single-phase outlet conditions, or to the SFM with Moody's or Fauske's correlation for the slip ratio for two-phase outlet conditions. The SFM shows better agreement with the data than the HEM when an empirical discharge coefficient is applied for two-phase outlet conditions. This is likely due to slip between the liquid and vapor phases.

Models for the major losses were validated with the data collected with an orifice with a large L/D. The empirical form loss model was applied at the entrance to the orifice, and the friction, acceleration, and gravity losses were integrated along the remaining length

of the orifice. The HEM assumptions were used for two-phase conditions. The model showed the best agreement with the data when Colebrook's correlation for the friction factor was used, in which case it predicted all of the data within five percent.

The data and models described in this study are useful for creating, validating, and improving analytical, numerical, and empirical models of pressure losses associated with the flow of S-$CO_2$ through orifices, and they provide a starting point for studies of more complex restrictions such as annuli and labyrinth seals.

A variety of interesting steps could be taken to further the research conducted in this study. Data were only collected and models were only developed and validated for sharp-edged orifices. It would be useful to perform a study of the effects of the inlet and outlet curvatures of orifices on the form losses. Also, the experiment used to collect data for this study is capable of achieving a variety of inlet conditions that were not investigated. For example, it would be possible to achieve saturated liquid inlet orifice inlet conditions, and data collected in this region may provide a better understanding of the flow of two-phase $CO_2$ through restrictions. Finally, it would be useful to collect data with sharp-edged orifices with larger diameters in order to verify that the models discussed in this study scale with diameter.

## References

[1] "A Technology Roadmap for Generation IV Nuclear Energy Systems," U.S. DOE Nuclear Energy Research Advisory Committee and the Generation IV International Forum2002.

[2] T. Conboy, S. Wright, J. Pasch, D. Fleming, G. Rochau, and R. Fuller, "Performance Characteristics of an Operating Supercritical CO2 Brayton Cycle," *Journal of Engineering for Gas Turbines and Power,* vol. 134, 2012.

[3] V. Dostal, P. Hejzlar, and M. J. Driscoll, "High-Performance Supercritical Carbon Dioxide Cycle for Next-Generation Nuclear Reactors," *Nuclear Technology,* vol. 154, pp. 265-282, 2006.

[4] A. Kruizenga, M. Anderson, R. Fatima, M. Corradini, A. Towne, and D. Ranjan, "Heat Transfer of Supercritical Carbon Dioxide in Printed Circuit Heat Exchanger Geometries," *Journal of Thermal Science and Engineering Applications,* vol. 3, 2011.

[5] A. Kruizenga, H. Li, M. Anderson, and M. Corradini, "Supercritical Carbon Dioxide Heat Transfer in Horizontal Semicircular Channels," *Journal of Heat Transfer,* vol. 134, 2012.

[6] A. Moisseytsev and J. J. Sienicki, "Validation of the ANL Plant Dynamics Code with the SNL S-CO2 Loop Transient Data," in *ASME Turbomachinery Expo* vol. Draft, ed. San Antonio, Texas: ASME, 2013.

[7] R. J. Allam, M. R. Palmer, G. W. Brown Jr., J. Fetvedt, D. Freed, H. Nomoto, *et al.*, "High Efficiency and Low Cost Electricity Generation from Fossil Fuels while Eliminating Atmospheric Emissions, Including Carbon Dioxide," *Energy Procedia,* vol. 37, pp. 1135-1149, 2012.

[8] T. Held, M. Persichilli, A. Kacludis, and E. Zdankiewicz, "Supercritical CO2 Power Cycle Developments and Commercialization: Why SCO2 Can Displace Steam," presented at the Power-Gen India and Central Asia, New Delhi, India, 2012.

[9] V. Dostal, P. Hejzlar, and M. J. Driscoll, "The Supercritical Carbon Dioxide Power Cycle: Comparison to Other Advanced Power Cycles," *Nuclear Technology,* vol. 154, pp. 283-301, 2006.

[10] D. Gavic, "Investigation of Water, Air, and Hybrid Cooling for Supercritical Carbon Dioxide Brayton Cycles," M.S. Mechanical Engineering, Mechanical Engineering, University of Wisconsin-Madison, Madison, WI, 2013.

[11] V. Dostal, "A Supercritical Carbon Dioxide Cycle for Next Generation Nuclear Reactors," Ph.D, Department of Nuclear Engineering, Massachusetts Institute of Technology, 2004.

[12] S. Klein and G. Nellis, *Thermodynamics*. New York, NY: Cambridge University Press, 2012.

[13] S. A. Klein, "Engineering Equation Solver". Madison, WI: F-Chart Software, 2013.

[14] M. D. Carlson, "Measurement and Analysis of the Thermal and Hydraulic Performance of Several Printed Circuit Heat Exchanger Channel Geometries," Master of Science, Department of Mechanical Engineering, University of Wisconsin-Madison, Madison, WI, 2012.

[15] S. M. Liao and T. S. Zhao, "Measurements of Heat Transfer Coefficients from Supercritical Carbon Dioxide Flowing in Horizontal Mini/Micro Channels," *Journal of Heat Transfer,* vol. 124, pp. 413-420, 2007.

[16] A. Moisseytsev and J. J. Sienicki, "Development of a Plant Dynamics Computer Code for Analysis of a Supercritical Carbon Dioxide Brayton Cycle Energy Converter Coupled to a Natural Circulation Lead-Cooled Fast Reactor," Argonne National Laboratory2006.

[17] A. Moisseytsev and J. J. Sienicki, "Title," unpublished|.

[18] (2013). *Encyclopedia of Chemical Engineering Equipment*.

[19] M. L. Corradini. (1997). *Fundamentals of Multiphase Flow*.

[20] G. B. Wallis, *One-dimensional Two-phase Flow*: McGraw-Hill, Inc., 1969.

[21] F. J. Moody, "Maximum Flow Rate of a Single-Component, Two-phase Mixture," *Journal of Heat Transfer,* vol. 87, pp. 134-142, 1965.

[22] H. K. Fauske, "The Discharge of Saturated Water Through Tubes," presented at the Chemical Engineering Progress Symposium Series, 1965.

[23] H. K. Fauske, "Contribution to the Theory of Two-Phase, One-Component Critical Flow," Argonne National Laboratory, Argonne, ILL1962.

[24] C. F. Colebrook, "Turbulent Flow in Pipes, with Particular Reference to the Transition Region Between the Smooth and Rough Pipe Laws," *Journal of ICE,* vol. 11, pp. 133-156, 1939.

[25] G. Nellis and S. Klein, *Heat Transfer*. New York, NY: Cambridge University Press, 2009.

[26] I. Pioro and R. B. Duffey, *Heat Transfer and Hydraulic Resistance at Supercritical Pressures in Power Engineering Applications*. New York, NY: ASME Press, 2007.

[27] W. H. McAdams, W. K. Woods, and L. C. Heroman, "Vaporization Inside Horizontal Tubes II-Benzene-Oil Mixtures " *Transactions of ASME,* vol. 64, pp. 193-200, 1942.

[28] S. L. Bragg, "Effect of Compressibility on the Discharge Coefficient of Orifices and Convergent Nozzles," *The Journal of Mechanical Engineering Science,* vol. 2, pp. 34-44, 1959.

[29] R. P. Benedict, "Generalized Contraction Coefficient of an Orifice for Subsonic and Supercritical Flow," *Journal of Basic Engineering,* pp. 99-120, 1971.

[30] D. A. Jobson, "On the Flow of a Compressible Fluid Through Orifices," 1955, pp. 767-777.

[31] J. A. Perry, "Critical Flow Through Sharp-edged Orifices," presented at the Transactions of ASME, 1949.

[32] R. E. Henry and H. K. Fauske, "The Two-Phase Critical Flow of One-Component Mixtures in Nozzles, Orifices and Short Tubes," *Journal of Heat Transfer,* pp. 179-187, 1971.

[33] G. Mignot, "Experimental Investigation of Critical Flow of Supercritical Carbon Dioxide," Master of Science in Nuclear Engineering, Department of Engineering Physics, University of Wisconsin-Madison, Madison, Wisconsin, 2008.

[34] G. P. Mignot, M. H. Anderson, and M. L. Corradini, "Measurement of supercritical CO2 critical flow: Effects of L/D and surface roughness," *Nuclear Engineering and Design,* vol. 239, pp. 949-955, 2009.

[35] J. P. Liu, Y. M. Niu, J. P. Chen, Z. J. Chen, and X. Feng, "Experimentation and correlation of R744 two-phase flow through short tubes," *Experimental Thermal and Fluid Science,* vol. 28, pp. 565-563, 2004.

[36] Y. Chen, M. Zhao, C. Yang, K. Bi, K. Du, and S. Zhang, "Critical Flow of Water Under Supercritical Pressures," in *14th International Heat Transfer Conference*, Washington, DC, USA, 2010.

[37] S. Zwolinski, M. Anderson, M. Corradini, and J. Licht, "Evaluation of Fluid-to-Fluid Scaling Method for Water and Carbon Dioxide at Supercritical Pressure," presented at the The 5th International Symposium on Supercritical Water-Cooled Reactors, Vancouver, British Columbia, Canada, 2011.

[38] "Instruction Manual-Hydro-Pac LX Compressor," ed. Fairview, PA: Hydro-Pac, Incorporated, 2010.

[39] *Duo-Tape Heavy Insulated Tape*. Available: http://www.heatingtapes.com/Duo_All.pdf

[40] "SITRANS P, Series DIII Transmitter," 4 ed: Siemens Energy and Automation, 2004.

[41] "Cubemass DCI-Coriolis mass flow measuring system," ed. Reinach, Switzerland: Endress+Hauser, 2010.

[42] "User's Guide-HP 34401A Multimeter," 4 ed. U.S.A.: Hewlett-Packard Company, 1996.

[43] "ImageJ," 1.47 ed: National Institutes of Health, 2013.

[44] "NewView 7300 Specifications," ed. Middlefield, CT: Zygo Corporation, 2013.

[45] H. Yuan, "Simulation of Supercritical CO2 through Circular and Annular Orifice," *Submitted for publication,* 2013.

# Appendices

Computer codes, orifice specifications, and complete data sets are available with the electronic copy of this thesis.